Breakdown Analysis of Monohalogenated Silacyclohexanes $(CH_2)_5SiHX$ (X=F, Cl, Br, I) and Attempted Synthesis of 1,1′-Silicon-bridged [5]Ferrocenophane

Katrín Lilja Sigurðardóttir

Faculty of Sciences
University of Iceland
2014

Breakdown Analysis of Monohalogenated Silacyclohexanes $(CH_2)_5SiHX$ (X=F, Cl, Br, I) and Attempted Synthesis of 1,1′-Silicon-bridged [5]Ferrocenophane

Katrín Lilja Sigurðardóttir

90 ECTS thesis submitted in partial fulfillment of a
Magister Scientiarum degree in Chemistry

Advisors
Ingvar Helgi Árnason
Ágúst Kvaran

External examiner
Pálmar Ingi Guðnason

Faculty of Sciences
School of Engineering and Natural Sciences
University of Iceland
Reykjavik, January 2014

Breakdown Analysis of Monohalogenated Silacyclohexanes $(CH_2)_5SiHX$ (X=F, Cl, Br, I) and Attempted Synthesis of 1,1'-Silicon-bridged [5]Ferrocenophane

Breakdown Studies and Ansa Complexes
90 ECTS thesis submitted in partial fulfillment of a *Magister Scientiarum* degree in Chemistry

Copyright © 2014 Katrín Lilja Sigurðardóttir
All rights reserved

Faculty of Sciences
School of Engineering and Natural Sciences
University of Iceland
Hjarðarhaga 2-4
101, Reykjavik
Iceland

Telephone: 525 4000

Bibliographic information:
Katrín Lilja Sigurðardóttir, 2014, *Breakdown Analysis of Monohalogenated Silacyclohexanes* $(CH_2)_5SiHX$ *(X=F, Cl, Br, I) and Attempted Synthesis of 1,1'-Silicon-bridged [5]Ferrocenophane*, M.Sc. thesis, Faculty of Physical Sciences, University of Iceland.

Printing: Háskólaprent
Reykjavik, Iceland, January 2014

Abstract

The project is mainly divided into two parts. The first part describes the breakdown processes of monohalogenated silacyclohexanes $(CH_2)_5SiHX$; X = F, Cl, Br, I. In order to obtain the breakdown diagrams, Threshold Photoelectron Photoion coincidence (TPEPICO) analysis were carried out on the compounds. For comparison, energy diagrams for the most common breakdown pathways were calculated by computational methods.

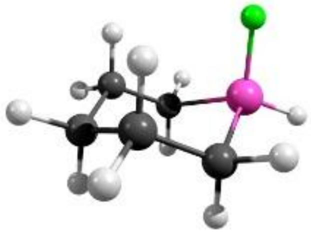

Figure A.1 Monohalogenated silacyclohexane, $(CH_2)_5SiHX$; X = F, Cl, Br, I.

In general, the appearance of the measured breakdown diagrams for all of the four rings are in good accordance with the calculated energy diagrams. It was shown that the loss of ethylene or propene requires similar energy for all the rings while the Si-X bond energy decreases considerably as the X atom gets larger. For the I-ring the Si-X bond energy is lower, resulting in a somewhat different breakdown diagram. Nevertheless, the bond dissociation energies cannot be read directly from the breakdown diagrams. The breakdown processes have to be modeled to obtain values comparable to the calculated results.

The second part of the project describes the attempts to synthesize hitherto unknown compounds of ansa complexes. The main compounds are [5]ferrocenophane and the analogous [5]chromoarenophane, with the bridging 1,5-disilapentane ligands containing the reactive SiH_2 groups.

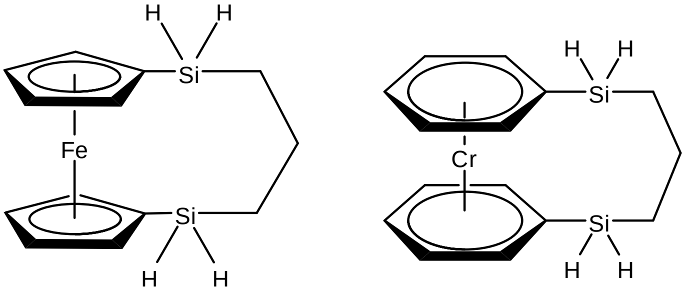

Figure A.2 [5]ferrocenophane and [5]chromoarenophane with a 1,5-disilapentane bridge.

Multiple attempts were made to synthesize the Fe-containing complex. NMR spectra of the products show a mixture of the desired complex and some side products but attempts to isolate and crystallize the complexes were unsuccessful.

Útdráttur

Verkefnið er að mestu tvíþætt. Fyrri hluti verkefnisins fjallar um niðurbrot á halógen-einsetnum kísilsexhringjum $(CH_2)_5SiHX$; X = F, Cl, Br, I. Til að kanna niðurbrotsferla efnanna voru gerðar svokallaðar Threshold Photoelectron Photoion coincidence (TPEPICO) [1] mælingar á efnunum. Til samanburðar voru orkuferlar fyrir helstu niðurbrotsleiðir sameindanna reiknaðir með skammtafræðilegum aðferðum.

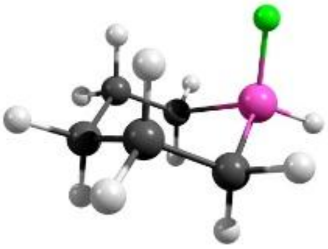

Mynd A.3 Halógen-einsetinn kísilsexhringur, $(CH_2)_5SiHX$; X = F, Cl, Br, I.

Á heildina litið er gott samræmi milli mældu ferlanna og þeirra reiknuðu. Niðurstöður sýna að til að kljúfa etýlen eða própen af sameindinni þarf álíka mikla orku fyrir alla fjóra hringina meðan Si-X tengjaorkan er lægri fyrir stærri halógena. Í tilfelli I-hringsins er Si-X tengjaorkan orðin lægri en sú orka sem þarf í etýlen klofnun og það veldur því að niðurbrotsferill I-hringsins er frábrugðinn hinum.

Það er ekki mögulegt að lesa tengjaorku sameindanna beint úr niðurbrotsferlunum. Til að öðlast nákvæm tölugildi sem hægt er að bera saman við reiknuðu orkuferla niðurbrotanna, þarf að herma niðurbrotin í þar til gerðu reikniforriti.

Seinni hluti verkefnisins fjallar um tilraunir að efnasmíði áður óþekktra efna úr flokki ansa komplexa. Í aðalhlutverki eru [5]ferrocenophane og hliðstætt [5]chromoarenophane með brúandi 1,5-disilapentane tengihóp en SiH_2 hópar hans eru afar hvarfgjarnir og því vandmeðfarnir.

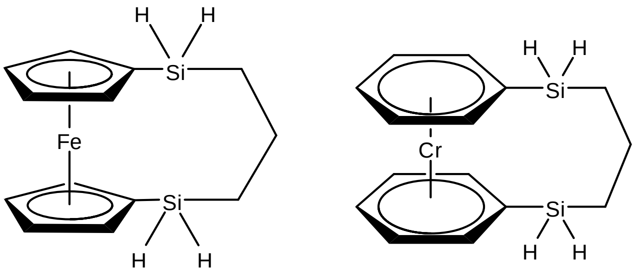

Mynd A.4 [5]ferrocenophane og [5]chromoarenophane með brúandi1,5-disilapentane tengihóp.

Fjölmargar tilraunir voru gerðar að efnasmíði brúandi ferrocene komplexins. NMR róf af myndefnunum sýna að hið ætlaða myndefni hafði myndast ásamt nokkrum hliðarmyndefnum en tilraunir til að einangra og kristalla myndefnin skiluðu ekki tilætluðum árangri.

To my children

Róbert Leó
Sumarrós Lilja
Hólmfríður Katla

Table of Contents

List of Schemes .... **xi**

List of Figures .... **xii**

List of Tables .... **xv**

Abbreviations .... **xvi**
Numbered compounds xvii

Acknowledgements .... **xix**

1 Introduction **1**
1.1 Conformational behavior and breakdown of 1-halo-1-silacyclohexanes 1
1.2 Ansa complexes 3
1.2.1 Ferrocenophanes 3
1.2.2 Chromoarenophanes 5

2 Breakdown studies **7**
2.1 General information 7
2.1.1 Data processing – Example of $SiC_5H_{11}F$ 9
2.2 Methods 13
2.2.1 iPEPICO measurements 13
2.2.2 Computational methods 13
2.3 Review of breakdown pathways 15
2.3.1 Pathways of C3-C4 ring opening – A geometrical approach 20
2.3.2 Pathway of X-loss – A geometrical approach 24
2.3.3 H-loss 26
2.4 Comparison 26
2.5 Calculated breakdown energy diagrams 28
2.5.1 F-substituted ring 28
2.5.2 Cl-substituted ring 29
2.5.3 Br-substituted ring 29
2.5.4 I-substituted ring 30
2.6 Experimental breakdown diagrams 30
2.6.1 F-substituted ring 31
2.6.2 Cl-substituted ring 32
2.6.3 Br-substituted ring 33
2.6.4 I-substituted ring 34
2.7 Ionization energy and excitation spectra 35
2.8 Modeling 36

3 Ansa complexes **37**
3.1 Preparation of the precursors 37
3.1.1 The isolation of **1a** 37

3.1.2 The preparation of **2** 39
3.2 Attempted synthesis of **3a** 40
3.2.1 Takeaway from the synthesis 54
3.2.2 Conclusions of ansa compounds 55
3.3 Calculated NMR shifts of **3a** 56
3.4 Attempted synthesis of **3b** 57

4 Other work 59
4.1 Nysted reaction 59
4.2 Mass spectrometric studies of a titanasiloxane complex 61

5 Summary 65

6 Experimental section 67
6.1 General comments 67
6.2 Experimental 67

References 75

Appendices 77

List of Schemes

Scheme 1.1 Ring opening polymerization of a strained ferrocenophane. 4

Scheme 1.2 Proposed reaction with a di-Grignard reagent adding a second bridge between the Si atoms. 5

Scheme 2.1 The transition state of the C_2H_4 loss is the formaton of a four-membered ring. 21

Scheme 2.2 Second ethylene loss 22

Scheme 2.3 H-shift from C5 to C4 followed by a propene loss. 22

Scheme 2.4 Dissociation of the Si-X bond resulting in a symmetrical ionic fragment. 24

Scheme 2.5 Ethylene loss following a X-loss includes the formation of a four-membered ring. 25

Scheme 2.6 Hydrogen loss. The hydrogen bonded to Si is most easily removed. 26

Scheme 3.1 Dilithiation of ferrocene with *n*-BuLi and TMEDA. 37

Scheme 3.2 Reaction with $SiMe_2Cl_2$, done to test the purity of **1a**. 38

Scheme 3.3 Three step synthesis of **2**. 39

Scheme 3.4 Coupling of the two precursors resulting in the desired formation of **3a**. 40

Scheme 3.5 Coupling of **1b** and **2** resulting in a [5]Chromoarenophane. 57

Scheme 4.1 The standard synthetic route to **4** is by reacting **2** with $CH_2(MgBr)_2$. 59

Scheme 4.2 The proposed formation of **4** in the one step reaction of **2** with the Nysted reagent. 59

Scheme 4.3 Formation of the eight-membered ring **6**. 61

List of Figures

Figure 1.1 The interconversion of a halogen-substituted silacyclohexane. 1

Figure 1.2 The size of the tilting angle α of an ansa complex describes the tension of the molecule. 3

Figure 1.3 [5]Ferrocenophane using 1,3-disilapentane as the bridging unit. 4

Figure 1.4 A geometry optimized configuration of **3a**. 5

Figure 2.1 The iPEPICO apparatus is located at the vacuum ultraviolet (VUV) beamline of the Swiss Light Source at Paul Sherrer Institut, Villigen. 7

Figure 2.2 Energy curves describing slow and fast dissociations. 8

Figure 2.3 A screenshot of the TOF processing window from the iPEPICO computer program for hν = 11.16 eV. 9

Figure 2.4 TOF mass spectra series of the breakdown of $SiC_5H_{11}F$. 10

Figure 2.5 Uncorrected breakdown diagram of $SiC_5H_{11}F$. 11

Figure 2.6 The value of the variable *a* describes the shift of the COG of a peak including two masses. 12

Figure 2.7 A minimum on a potential energy surface. 13

Figure 2.8 A saddle point on a potential energy surface. 14

Figure 2.9 $(CH_2)_5SiHX$ showing numbering of carbon atoms. 15

Figure 2.10 Calculated bond dissociation energies of the ring opening cleavages. 16

Figure 2.11 Comparison of the calculated dissociation energies for all hydrogen cleavages. 17

Figure 2.12 Geometry optimized ions resulting from the elimination of different H atoms. 19

Figure 2.13 Energy diagram of the relaxed surface scan of increased C3-C4 bond distance. Example showing the F-substituted ring. 20

Figure 2.14 Energy curve describing the formation of the four-membered ring. Example showing the F-substituted ring. 21

Figure 2.15 Energy curve describing the H-shift from C5 to C4. 23

Figure 2.16 Si-X bond lengths compared to the Si-X dissociation energies. 25

Figure 2.17 Comparison of the main calculated bond dissociation and fragment loss energies. 27

Figure 2.18 Calculated breakdown energy diagram of $SiC_5H_{11}F$. 28

Figure 2.19 Calculated breakdown energy diagram of $SiC_5H_{11}Cl$. 29

Figure 2.20 Calculated breakdown energy diagram of $SiC_5H_{11}Br$. 29

Figure 2.21 Calculated breakdown energy diagram of $SiC_5H_{11}I$. 30

Figure 2.22 Breakdown diagram of $SiC_5H_{11}F$. The propene loss is omitted. 31

Figure 2.23 Breakdown diagram of $SiC_5H_{11}Cl$. The Cl-loss peak is omitted. 32

Figure 2.24 Breakdown diagram of $SiC_5H_{11}Br$. 33

Figure 2.25 Breakdown diagram of $SiC_5H_{11}I$. 34

Figure 2.26 TPES showing the absorbtion as a function of photon energy. 35

Figure 3.1 ^{1}H NMR spectrum of the product from the test reaction. 38

Figure 3.2 ^{1}H NMR spectrum from the first attempt at synthesis of 3a. 41

Figure 3.3 Comparison of ^{1}H NMR spectra of products from reaction 1, aromatic region. 43

Figure 3.4 Comparison of ^{1}H NMR spectra of products from reaction 1, aliphatic region. 44

Figure 3.5 Comparison of the aromatic region of ^{1}H NMR spectra from reactions 2 and 4. 46

Figure 3.6 Comparison of the aliphatic region of ^{1}H NMR spectra from reactions 2 and 4. 46

Figure 3.7 Comparison of the aromatic region in ^{1}H NMR spectra of products from reaction 4. 47

Figure 3.8 Comparison of the aliphatic region in ^{1}H NMR spectra of products from reaction 4. 47

Figure 3.9 ^{1}H NMR spectrum of product 5-A. 49

Figure 3.10 Comparison of the aromatic region in ^{1}H NMR spectra of products from reaction 6. 50

Figure 3.11 Comparison of the aliphatic region in ^{1}H NMR spectra of products from reaction 4. 51

Figure 3.12 Comparison of the aromatic region in ^{1}H NMR spectra of products from reaction 8. 52

Figure 3.13 Comparison of the aliphatic region in ^{1}H NMR spectra of products from reaction 8. 53

Figure 3.14 A possible product is the polymer. 55

Figure 3.15 One of the possible products is the dimer. 55

Figure 3.16 The most promising ^{1}H NMR spectrum from the attempted synthesis of **3b**. 58

Figure 4.1 ^{1}H NMR spectrum from the only attempted synthesis of **4**. 60

Figure 4.2 Mass spectrum of **6**. The marked peak was analyzed and simulated. 61

Figure 4.3 The peak of the mass spectrum of **6** corresponding to H_2O-loss. The experimental spectra is above and the simulated below. 63

List of Tables

Table 2.1 Change of bond distances during H-shift (Cl-substituted ring). 23

Table 2.2 Thermally corrected barriers and energy changes of transition states. Values in [eV]. 24

Table 2.3 Si-X bond lengths compared to the Si-X dissociation energies. 25

Table 2.4 The main calculated bond dissociation and fragment loss energies, values given in eV. 27

Table 2.5 Comparison of calculated and experimental breakdown values [eV]. 31

Table 2.6 Comparison of calculated and experimental breakdown values [eV]. 32

Table 2.7 Comparison of calculated and experimental breakdown values [eV]. 33

Table 2.8 Comparison of calculated and experimental breakdown values [eV]. 34

Table 2.9 Comparison of calculated (at 298 K) and experimental values for ionization energy. 35

Table 3.1 Summary of the yields for the three step synthesis of **2**. 40

Table 3.2 Treatment of products from reaction 1. 42

Table 3.3 Chemical shifts of the ^{1}H NMR peak sets I, II and III. 45

Table 3.4 Treatment of products from reaction 4. 48

Table 3.5 Treatment of products from reaction 6. 50

Table 3.6 Treatment of products from reaction 8. 52

Table 3.7 Summary of reaction conditions for the attempted synthesis of **3a**. 54

Table 3.8 Calculated ^{1}H NMR chemical shifts for compund **3a**. Comparison to observed peak sets I, II and 5-A. Values in ppm. 56

Table 3.9 Calculated ^{13}C NMR chemical shifts for compound **3a**. Comparison to observed peak sets I, II and 5-A. Values in ppm. 56

Table 3.10 Calculated ^{29}Si NMR chemical shift for compound **3a**. 56

Table 4.1 Fragmentation of **6** observed in its mass spectrum. 62

Abbreviations

a.u.	arbitrary units
BD	breakdown diagram
BuLi	butyl lithium
COG	center of gravity
Cp	cyclopentadienyl ($C_5H_5^-$)
Cp*	pentamethylcyclopentadienyl
DFT	density functional theory
Et	ethyl-
iPEPICO	Imaging Photoelectron Photoion coincidence
Me	methyl-
NMR	nuclear magnetic resonance
PFS	polyferrocenylsilanes
ROP	ring opening polymerization
SEC	size exclusion chromatography
THF	tetrahydrofuran
TLC	thin layer chromatography
TMEDA	N,N,N’N’-tetramethylethylenediamine
TOF	time of flight (mass spectrometer)
TPEPICO	threshold photoelectron photoion coincidence
TPES	threshold photoelectron spectra
TS	transition state

Numbered compounds

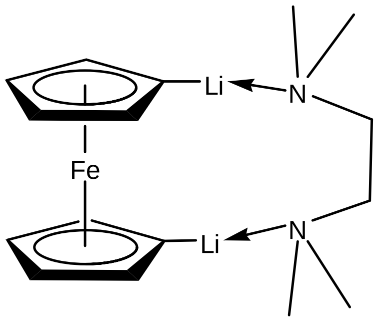

1a

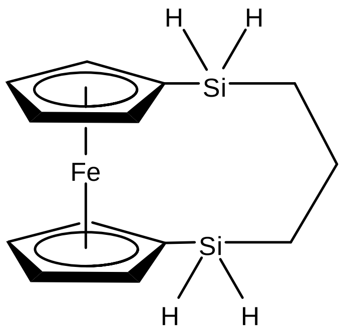

3a

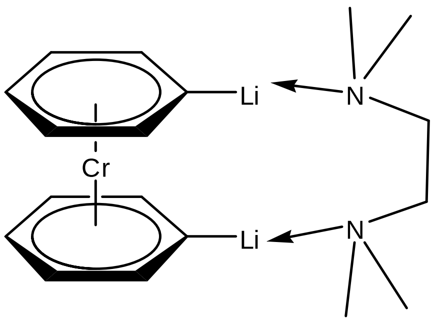

1b

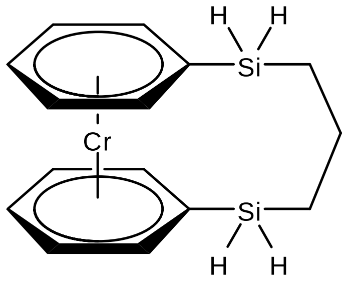

3b

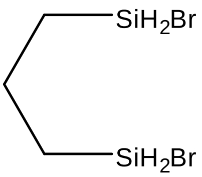

2

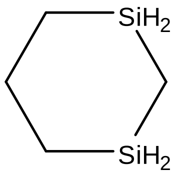

4

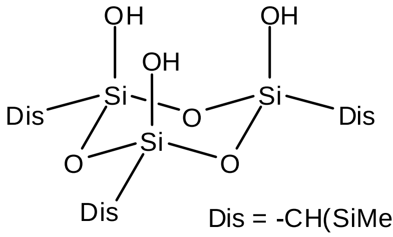

Dis = -CH(SiMe$_3$)$_2$

5

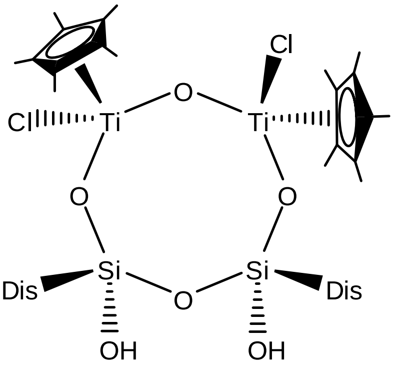

6

Acknowledgements

Foremost I would like to thank my supervisor, prof. Ingvar Helgi Árnason. I am extremely thankful for his guidance, patience and good friendship.

For computational assistance and helpful discussions I would like to thank

Dr. Ragnar Björnsson

Dr. Benedikt Ómarsson

Dr. Simon Klüpfel

At the University of Iceland I would like to thank

Ágúst Kvaran for his guidance and helpful discussions

Sigríður Jónsdóttir for NMR measurements

Sverrir Guðmundsson for glassblowing and for fixing broken glassware

Svana Stefánsdóttir for providing chemicals

Helga Dögg Flosadóttir for assistance with MS measurements

At Paul Sherrer Institut, Switzerland

Andras Bodi for iPEPICO measurements, guidance and kind hospitality

I would also like to thank

Romeo Losso (Romeo_Losso@Yahoo.it), for kindly proposing the reactions of the ferrocene-containing ansa complexes and the Nysted reaction

Ísak Sigurjón Bragason and Haraldur Gunnar Guðmundsson for helpful discussions and good friendship

My fiancé Kristján Páll Rafnsson for his generous amounts of love, support and patience

All the fantastic people I got to know during my studies: Friends at the Science Institute, my teachers and my students at the University of Iceland and members of Sprengjugengið, for lightening up the period of my studies

For financial support

University of Iceland Research Fund

1 Introduction

1.1 Conformational behavior and breakdown of 1-halo-1-silacyclohexanes

The conformational features of substituted cyclohexanes are well known since the stereochemistry of these compounds is one of the most studied fields in organic stereochemistry [2, 3]. A six-membered ring exists as a mixture of two chair conformers which interconverts rapidly so that the substituents possess either axial or equatorial position (**Figure 1.1**). In the unsubstituted cyclohexane the conformers are in equal concentration but when the cyclohexane is substituted, the substituents usually prefer the equatorial positions, thereby changing the relative abundance of the two conformers. What describes the experimentally observed behavior of the six-membered rings are steric effects, especially 1,3-synaxial interactions, electrostatic dipole-dipole interactions and hyperconjugation [4-6]. The steric effects are dominating in substituted cyclohexanes. Substituents in monosubstituted cyclohexanes always prefer the equatorial position of the chair conformation with rare exceptions and bulkier substituents increase this tendency [7].

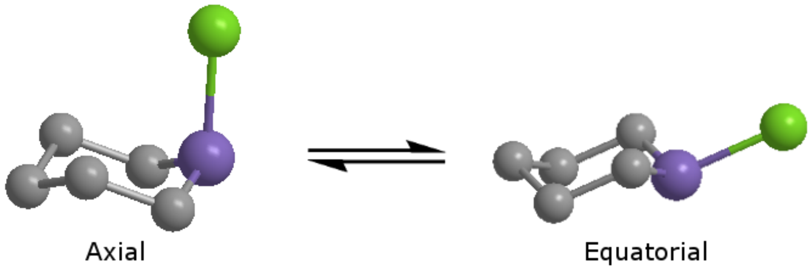

Figure 1.1 The interconversion of a halogen-substituted silacyclohexane.

The background of this project attributes to the conformational studies of substituted silacyclohexanes. Silacyclohexanes are comparable to cyclohexanes due to the similarities of carbon and silicon. Silicon is known to be the more electropositive chemical analogue of carbon and is located directly below it in group 14 of the periodic table. However, the chemistry of carbon and silicon differ greatly in the nature. Carbon accounts for the extensive organic chemistry of life whereas silicon, strongly bonded to oxygen, forms silicates which are crystalline materials and the main components of the Earth’s crust [8]. The similarities of these two elements are more demonstrative in the area of organosilicon chemistry, where carbon atoms are replaced by silicon in the molecular structure. The synthetic routes to the silicon-containing counterparts are more challenging because of their greater reactivity towards atmospheric oxygen and water vapor, especially when the compounds contain the very reactive Si-H or Si-halogen bonds. In recent years, a series of silicon-containing six-membered ring systems have been prepared in Árnason’s research group at the Science Institute. The conformational equilibria of several 1-monosubstituted 1-silacyclohexanes $C_5H_{10}SiH$-R have been investigated thoroughly in both experimental and theoretical manner [9-12]. Similar conformational behavior might be expected for the cyclohexanes and silacyclohexanes but the results show an increased preference for the axial position when monosubstituted silacyclohexanes are compared to monosubstituted cyclohexanes. In the case when the substituent is -CF_3 [13, 14], -SiH_3 [15] or -X (X = F, Cl, Br, I) [10], the equilibria have been shifted such that the substituent prefers the axial position contrary to the behavior of their cyclohexane analogues. Árnason's latest paper of this topic summarizes the conformational behaviors of *cyclo*-$C_5H_{10}SiHX$ (X = F, Cl, Br, I). Investigations by means of various experimental techniques as well as high-level quantum chemical calculations were made on this series. All experiments agreed that for all of these derivatives, the axial conformer was preferred over the equatorial one. It also revealed an increasing affinity for the axial conformer in going from the lightest halogen derivative to the heaviest. This contradicts the same series of substituted cyclohexanes as they behave the opposite way, showing greater equatorial tendency for larger halogens.

A full understanding of the conformational properties of both substituted cyclohexanes and silacyclohexane ring systems is needed to construct a unified model explaining their different behavior. The above-mentioned results from the study of the halogen-substituted silacyclohexanes call for further examination since they have the great advantage of being substituted with a series of homologous substituents. In order to obtain a deeper thermo-chemical understanding about these ring systems, it was decided to carry out a Threshold Photoelectron Photoion coincidence (TPEPICO) [16, 17] analysis on monohalogenated silacyclohexanes $(CH_2)_5SiHX$; X = F, Cl, Br, I. For this purpose, fresh samples were prepared in Árnason's group [18].

These measurements make possible the analysis of parallel and sequential dissociations of the ionic molecules. The experimental data include TOF mass spectra of the molecular ion and of its ionic fragments. A breakdown diagram is obtained from the mass spectra by integrating the correct TOF mass peaks and plotting their fractional abundance as a function of the photon energy. For comparison, energy diagrams for the most common breakdown pathways were calculated by computational methods.

1.2 Ansa complexes

1.2.1 Ferrocenophanes

Metallocenes are a type of organometallic compounds consisting of two aromatic ring systems bound on opposite side of a central metal atom. Derived from their shape, they are commonly known as sandwich complexes. Ferrocene, being the prototypical metallocene, is made up of an iron atom between two aromatic cyclopentadienyl (Cp) rings ($C_5H_5^-$). It was discovered simultaneously and independent of each other by two research groups early in the 1950's. Kealy and Pauson's paper entitled 'A New Type of Organo-Iron Compound' was published in December 1951 [19], but Miller, Tebboth and Tremaine's paper, 'Dicyclopentadienyliron' was published two months later, in February 1952 [20]. However, the latter paper was received by the publisher prior to the former. The discovery of ferrocene [21-23] turned out to be a milestone for organometallic chemistry and opening new dimensions of chemistry to be explored [24, 25]. In ferrocene, the iron atom is Fe(II) and each Cp ring has a single negative charge. Adding one electron to the Cp ring brings the number of π-electrons to six, making it aromatic. The π-electrons of both rings, a total of 12 electrons, are shared with the metal. Combined with the six d-electrons of Fe(II), the complex attains an 18-electron configuration which is one of the reasons for its remarkable stability. With lithiation methods, various groups can be placed on the Cp ligands. When the same group is attached to both rings, the attached group is called "a bridge" and the resulting complex is called [n]ferrocenophane where n stands for the number of atoms in the bridging chain. Analogous complexes can be made with other metals and aromatic rings and this family of compounds is called ansa complexes. However, the most studied ansa complexes are the ferrocenophanes.

One of the most interesting properties of ansa complexes is the tilting of the two aromatic rings. The tilting angle, described by the symbol α in **Figure 1.2**, varies for different bridging units, having values on a broad range up to more than 32° [26].

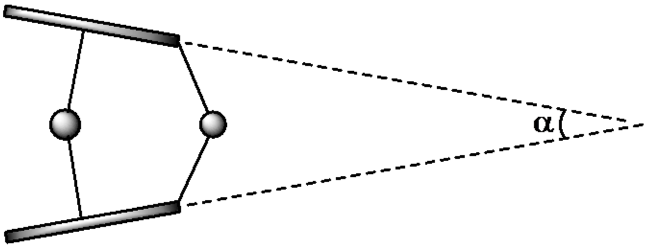

Figure 1.2 The size of the tilting angle α of an ansa complex describes the tension of the molecule.

Generally, shorter bridges cause greater tilting angles, making the compound more strained and consequently less stable. Therefore, the most strained ferrocenophanes having n = 1 were not the first to be prepared [27].

What makes the tilting angle such an interesting feature of the ansa complexes is their increased susceptibility to undergo strain releasing ring opening polymerization (ROP) reactions. This field of study is relatively new; the first reports of ROP synthesis of polymers bearing transition metals in the backbone were published in 1989 [28, 29]. ROP of an ansa complex results in a macromolecule with a backbone consisting of its metallocene alternately with its bridging unit. In the case of the bridging unit being Si, ROP leads to polyferrocenylsilanes (PFS) of which polyferrocenyldimethylsilane is by far the most studied. One such example is given in **Scheme 1.1**.

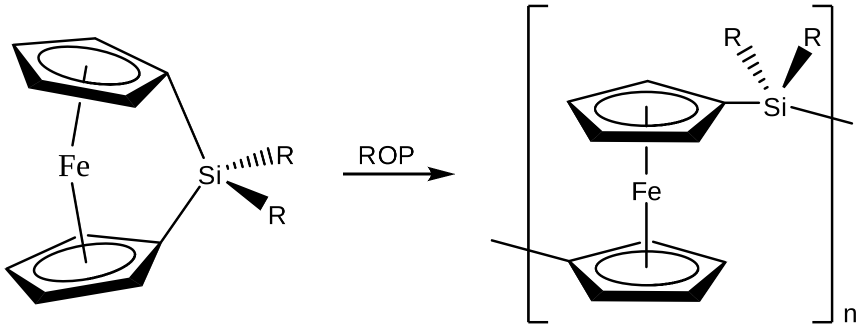

Scheme 1.1 Ring opening polymerization of a strained ferrocenophane.

Several ROP methods have been developed, the most common methods being thermal, transition metal catalyzed, photolytic and carbionic. A number of PFS polymer types have been synthesized [26] and their chemical and physical properties prove to be very interesting. Studies of the PFS‘s optical properties have revealed that they have exceptionally high refractive indices along with relatively low optical dispersion, making these materials ideal for coating of optical devices [30]. Although the PFS-based materials are still in their initial stages of development, scientists are nevertheless convinced that these materials will find commercial applications and will play a crucial role in future technology [31].

The aim of this project is to synthesize the ansa complex [5]ferrocenophane with the bridging unit -$SiH_2(CH_2)_3SiH_2$- (**3a**). This complex is a potential precursor for a ROP reaction which could bring a new member to the family of polyferrocenylsilanes (**Figure 1.3**).

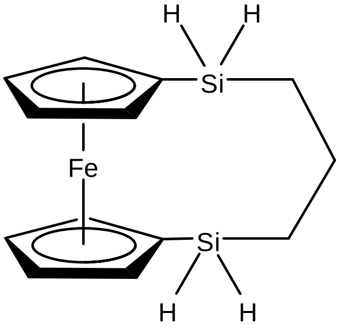

3a

Figure 1.3 [5]Ferrocenophane using 1,3-disilapentane as the bridging unit.

3a was geometry optimized by the force field implemented in Spartan 08. The outcome of the optimization is what makes the molecule a particularly flavourful subject matter (**Figure 1.4**). Its distinctive feature is the tilting of the two Cp rings, which in this case tilt away from the bridge, making the tilt angle α negative.

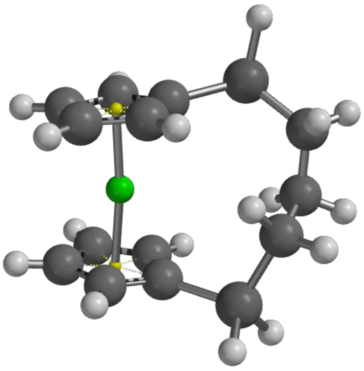

Figure 1.4 A geometry optimized configuration of **3a**.

Only a single example of an ansa complex having a negative α value was found in the literature. It is the zirconium bridged [(η^5-C_5H_4)Fe(η^5-C_5Me_4)CH_2ZrCp_2] having α value of -5.5°. The small negative tilting angle makes this particular compound resistant against thermal ROP.

The main goal of this project was to synthesize the silicon bridged [5]ferrocenophane, crystallize it and examine its geometrical properties. Expectations in succeeding in the synthesis were very high and plans were made for even further reactions of the compound. The SiH_2 hydrogens could for example be replaced by alkyl or aryl ligands. Or they could be brominated, offering the option of placing a second bridge between the two Si atoms in a di-Grignard reaction (**Scheme 1.2**). The latter reaction is very interesting due to the fact that geometry optimization of the dibridged product showed the tilting angle changing from negative to positive.

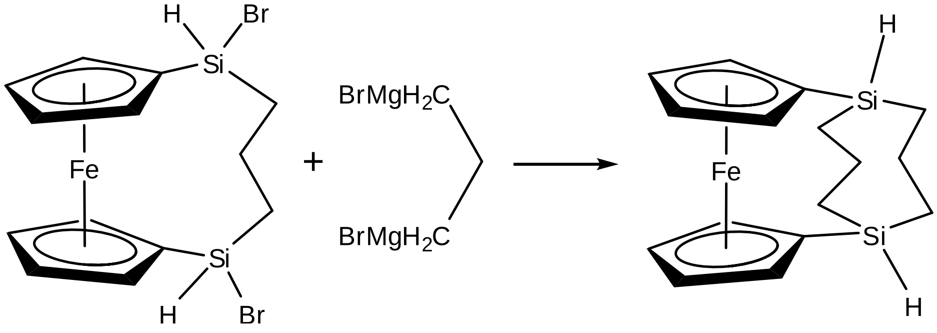

Scheme 1.2 Proposed reaction with a di-Grignard reagent adding a second bridge between the Si atoms.

1.2.2 Chromoarenophanes

Bis(benzene)chromium is the metallocene bearing Cr atom between two benzene rings. Its discovery by Fisher and Hafner in 1955 [32] was a great success since the compound was generally believed to be too unstable to exist. The reason for the believed unstability was because each benzene molecule in the complex is neutral, making the central chromium atom zerovalent. Fisher's idea was that if each benzene molecule would share its six π-electrons with the six d-electrons of Cr(0), a stable 18-electron configuration would be achieved.

Bis(benzene)chromium is indeed easily oxidized to the cationic species upon efforts to carry out substitution reactions on the benzene rings. Attempts to metallize bis(benzene)-chromium were first successful in 1961 when Fisher and Brunner used suspensions of *n*-amylsodium in hexane for that purpose [33]. For years, the studies of chromoarenophanes were far behind the investigations of the analogous ferrocenophanes, thereby the preparation of their polymers remained a key synthetic challenge [34, 35]. The ROP of silicon-bridged [1]chromoarenophanes were not reported until in 2004 [36]. They are driven by metal-catalysts as opposed to the [1]ferrocenophanes only needing heating at 130 °C to undergo the same reaction [37]. Accordingly, the PFS were synthesized more than 10 years in advance of the polymers bearing $Cr(arene)_2$ and organosilane units in their backbone. This difference in behavior can partly be put down to the tilt angle of [1]chromoarenophanes generally being smaller than of the corresponding [1]ferrocenophanes, making the latter more strained and consequently more prone to ROP. As an example, the tilt angles are 16.6° and 20.8°, respectively, when the bridging unit is $SiMe_2$ [38, 39]. Consequently, research of polymers resulting from ROP of chromoarenophanes is still in its early stage. Nevertheless, materials with regular pore structures on the nanometer or micrometer scale have been synthesized bearing bis(η^6-arene) derivatives in the backbone [40].

All reactions described in this project using ferrocene, were intended to be tested for bis(benzene)chromium as well. Since ferrocene is significantly more stable and the more affordable of these two, all reactions were first tried using ferrocene. Identification of products in the first stages of the synthetic process is solely by ^1H and occasionally ^{13}C NMR measurements. Many spectra were not usable as they revealed very broad signals, presumably because of paramagnetic properties of some products.

It should be pointed out that the aromatic protons on the disila-bridged [5]ferrocenophane and [5]chromoarenophane experience a great shielding effect from both the metal central atom and the substituted silicon atoms. Therefore, their signals are shifted upfield and have chemical shifts in the interval 4.0-4.5 ppm. Also, tilting of the sandwich structure generally effects the shielding of aromatic protons. This is a widely observed phenomenon which consists of shifting towards higher field as a result of stacking of arenes, one ring being positioned in the shielding region of another ring [41, 42]. However, because of the unknown and maybe negative tilting of the aromatic rings in the [5]ferrocenophane and [5]chromoarenophane of this work, and due to the lack of known suitable reference substances, it is not possible to predict whether the aromatic protons would be shifted up- or downfield as a result of the tilting.

2 Breakdown studies

2.1 General information

The dissociative photoionization process of a gaseous molecule causes a cleavage of a molecular bond according to the energy of the photon used, $h\nu$. In general, the fragments produced in the energy selected ionic reaction are a cation, a neutral species and a photoelectron [43]:

$$AB + h\nu \rightarrow A^{+} + B + e^{-}$$

In the iPEPICO measurements, the photoelectrons and the cations produced in the photoionization process are extracted with low electric fields in opposite directions (**Figure 2.1**). The electrons are velocity map imaged on a position sensitive detector. By map imaging, the threshold electrons having zero velocity perpendicular to the extraction field hit the center of the detector. They are strongly contaminated by energetic (hot) electrons having velocity in the direction of the extraction field. The major advantage of the iPEPICO instrument is the ability to subtract the hot electron signal leaving only the electron signal corresponding to the true threshold energy. The masses of the photoions are determined by a time of flight (TOF) mass spectrometer. Only the cations in coincidence with the true threshold energy signal are processed [16].

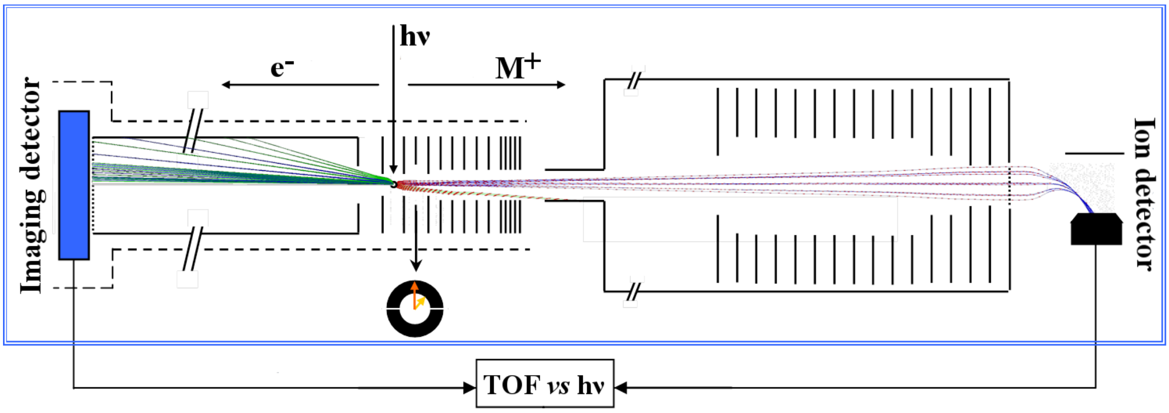

Figure 2.1 The iPEPICO apparatus is located at the vacuum ultraviolet (VUV) beamline of the Swiss Light Source at Paul Sherrer Institut, Villigen.

The first dissociation step of the molecule occurs at the lowest threshold. At higher energies, the fragments dissociate further via sequential dissociation paths. If two different dissociations have similar threshold energies, parallel dissociation paths are detected. The molecules discussed in this project fragment in a quite complex manner which will be described later in detail. At the higher energy sequential dissociations, more scattering is observed in the breakdown curve due to the increased product energy distribution. This scattering increases with each fragment loss, causing the precision of the measurements to decrease. For this reason, the lowest energy dissociation path of a molecule can be measured most accurately but at higher energies, the sequential dissociations are not as sharp and their energy values are therefore more difficult to determine precisely.

Dissociations are either fast or slow. In **Figure 2.2**, energy dissociation curves describing both fast and slow dissociations are seen. The difference is attributed to the transition state of the slow dissociation energy curve, which is at higher energy than the two resulting fragments. Therefore, only the ions having enough energy to pass the transition state are able to dissociate. No additional energy is needed if the curve does not contain a transition state. Then, the dissociation takes place as soon as the energy is reached, resulting in a fast dissociation.

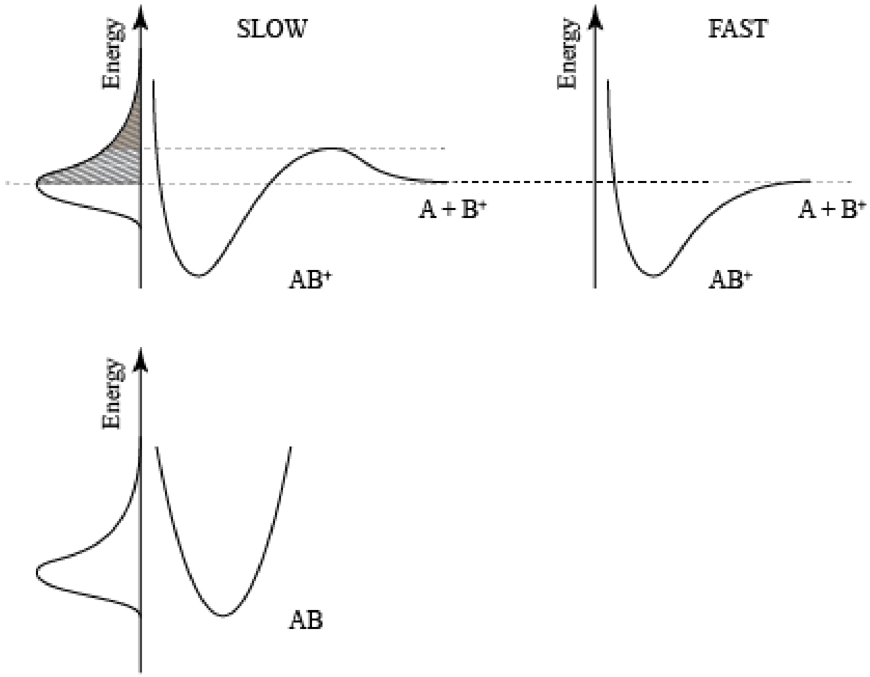

Figure 2.2 Energy curves describing slow and fast dissociations.

The treatment of the fast dissociations is considerably easier than for the slow ones. If the dissociation has a low rate constant, only some of the ions have enough time to dissociate on their way to the sensor even though their energy is above the threshold [16].

2.1.1 Data processing – Example of $SiC_5H_{11}F$

The cations produced in the energy selected dissociative photoionization reaction are detected in a TOF mass spectrometer, providing spectra showing abundance of ionic fragments as a function of the time of flight in μs. A computer program specially developed for iPEPICO measurements was used to process the data. One of the programs windows is shown in **Figure 2.3**. This is the TOF distribution spectrum or more specifically, the TOF mass spectrum for the photoionization of $SiC_5H_{11}F$ at 11.16 eV. In order to introduce the processing procedure, an example will be given for the $SiC_5H_{11}F$ breakdown and its analysis described in details.

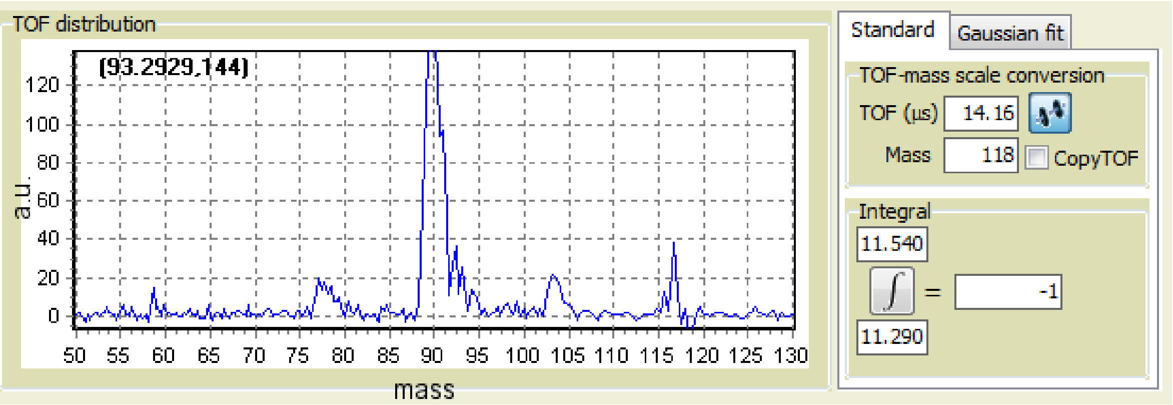
TOF (µs) 14.16
Mass 118
☐ CopyTOF
Integral
11.540
11.290
= -1

Figure 2.3 A screenshot of the TOF processing window from the iPEPICO computer program for hν = 11.16 eV.

First, the time scale of the spectrum is converted to mass. It is enough to identify only one peak in the spectrum. In this particular case, the parent ion having mass of 118 is detected at time 14.16 μs. By providing this information, the program converts the scales of all spectra from μs to mass. A series of TOF mass spectra is obtained where the abundances of the ionic fragments increase with increasing photon energy. In the TOF spectrum in **Figure 2.3**, the parent ion of mass 118 has dissociated to some degree so that the fragment ion with the mass 90 is the most abundant. This mass of 90 corresponds to the loss of an ethylene fragment of mass 28. At low photon energy, only the parent ion is detected but at higher energies, the abundance of the parent ion decreases and mass peaks of fragment ions are seen instead. **Figure 2.4** shows seven chosen TOF mass spectra for the molecule $SiC_5H_{11}F$ for the photon energy range 10.10-14.60 eV.

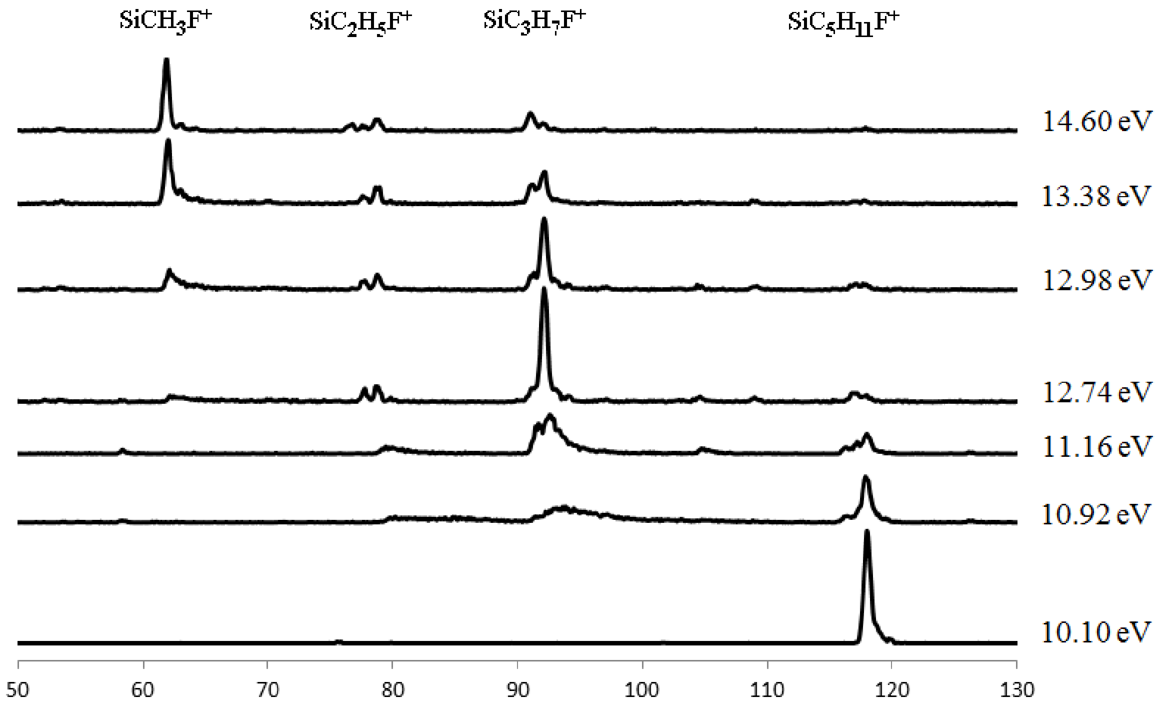

Figure 2.4 TOF mass spectra series of the breakdown of $SiC_5H_{11}F$.

The lowest spectrum in the figure corresponds to photon energy of 10.10 eV. This energy is higher than the ionization energy of the molecule but lower than the first dissociation energy, so the only fragment detected is the undissociated parent ion with mass 118. At 10.92 eV, the fractional abundance of the parent ion has decreased and unsymmetrical mass peaks corresponding to the fragments $SiC_3H_7F^+$ (ethylene loss) and $SiC_2H_5F^+$ (propene loss) are seen, having masses of 90 and 76, respectively.[1] As the energy is increased, the mass peaks get more symmetrical. This peak shape is characteristic for slow dissociations. At high enough energy, the mass peaks for slow dissociations get symmetrical as can be seen in the TOF mass spectrum of energy 12.74 eV. The $SiC_3H_7F^+$ fragment dissociates further by losing another ethylene and leaving the fragment ion $SiCH_3F^+$ with mass of 62. The unsymmetrical peak formation is already detected at energy of 12.74 eV but attains a symmetrical shape as the energy increases.

Breakdown diagrams are obtained from these TOF mass spectra. In the iPEPICO computer program, mass intervals in the TOF spectra are chosen by hand for each mass peak of the breakdown process. By running a script in the program, it counts the ion coincidences in each interval and writes it out in an Excel output sheet. (Example of an iPEPICO script is given in the appendix G). When the fractional abundances of the ionic fragments are plotted as a function of the photon energy, a breakdown diagram is obtained. Special caution should be taken when plotting the fractional abundances as the peaks can include impurities which need to be subtracted to obtain the correct abundance of the fragment. One such example can be seen in **Figure 2.4**, in the TOF spectra of energies 12.74 eV, 12.98 eV and 13.38 eV, where a small peak is detected at mass 117, after the dissociation of the parent ion. This is due to the dissociation corresponding to a single H atom loss from the parent ion, and takes place at energy just above the initial ethylene and propene losses. The unprocessed breakdown diagram includes the fractional abundance of all the ionic fragments chosen to be integrated. As shown in **Figure 2.5**, this diagram does not represent the true breakdown diagram of the molecule. It includes some contamination which distorts its appearance.

---

[1] The information contained in the original TOF mass spectra is abundance as a function of channel numbers. The data was scripted in the iPEPICO computer program and transferred to Excel where the channel numbers were changed to mass by hand. For some unknown reason, the mass interval of one channel is not constant for increasing channel number, causing a minor shift of the mass numbers in the final excel graph. **Figure 2.4** was only made for explanation. The peaks having masses 62 and 118 were set at these masses by hand, causing the shift of the masses in between.

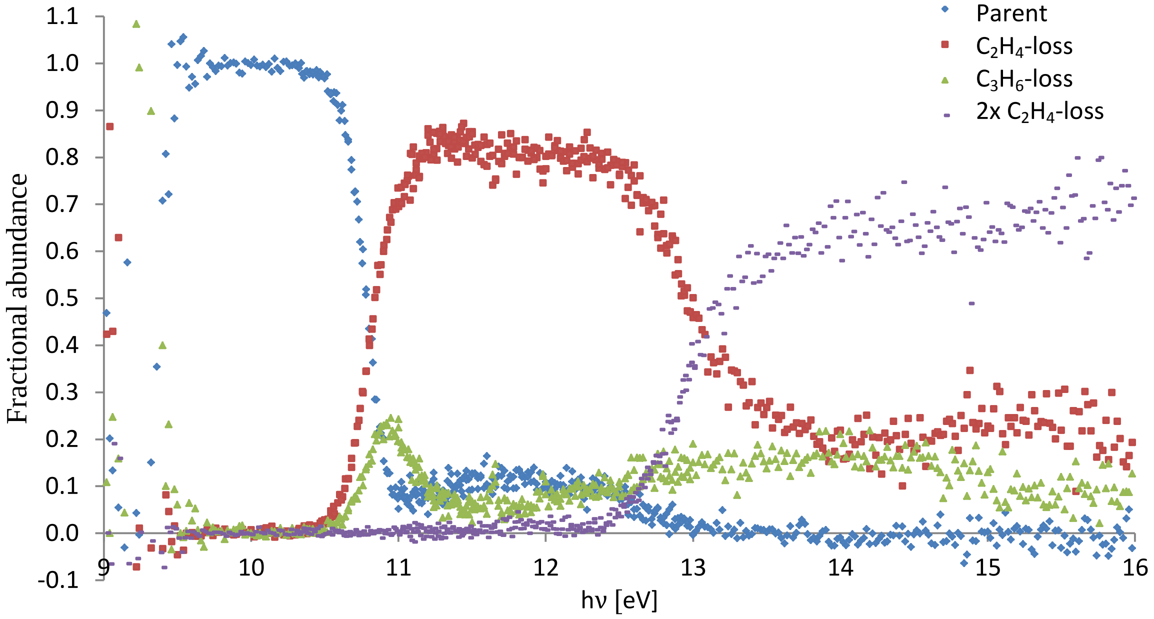

Figure 2.5 Uncorrected breakdown diagram of $SiC_5H_{11}F$.

Below 9.5 eV the energy is not sufficient to ionize the molecule and no ionic fragments are detected. Above 9.5 eV, ionization has occurred, resulting in the detection of the parent ion in 100% fractional abundance. After the ion starts to dissociate at about 10.5 eV, the fractional abundance of the parent ion does not go down to 0% but stays at about 10% until at energy about 12.5 eV. The ions accounting for the 10% peak correspond to a single H atom loss and have the mass 117 and this small mass difference of the two ions causes them to be integrated together. In order to correct for the H-loss peak contamination, center-of-gravity (COG) analysis are carried out on the peak. At low energies, the mass peak includes only the parent ion and the COG of the peak is the mass of the parent ion. At higher energies, COG of the peak gradually shifts to the mass of the H-loss fragment ion, 117. In the energy interval between these two extremes, the COG is somewhere between the two masses, 117 and 118. By computing the location of the COG for the fused mass peaks, it is possible to divide the integration of the mass peak between the parent ion and the H-loss ion.

Now, let's explore the interval between the masses of these two ions. The variable *a* is defined as the fraction of this peak area corresponding to the parent ion, i.e. below the COG. **Figure 2.6** illustrates how the value of *a* changes as the energy is increased.

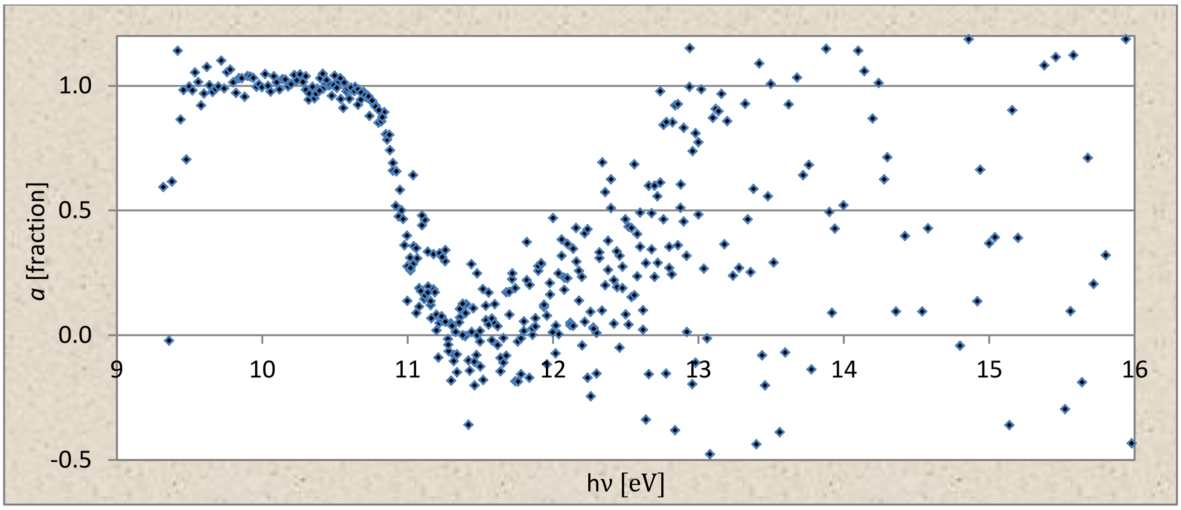

Figure 2.6 The value of the variable *a* describes
the shift of the COG of a peak including two masses.

At low energies, *a* has approximately the value 1, meaning that the peak includes only the parent ion. As the energy increases, the value of *a* decreases. It shifts towards 0, whereas the peak includes only the H-loss ion. As the energy is increased even further the H-loss ion starts to dissociate and the peak disappears so that the value of *a* gets scattered and has eventually no meaning.

At 10.5 eV, the slow dissociations corresponding to ethylene and propene losses (**Figure 2.5**) are detected, the ethylene loss being greater. However, the propene loss raises steeply at first and then decreases again. The peak is clearly contaminated in the interval between 10.5 eV – 11.5 eV (see **Figure 2.4** and **Figure 2.5**). The contamination has not been identified and was not corrected for since it is quite clear that the ethylene loss is greater and has an important sequential dissociation. The further dissociation of the ethylene loss fragment, $SiC_3H_7F^+$, corresponds to a second ethylene loss resulting in the detected ionic fragment $SiCH_3F^+$. Again, the $SiC_3H_7F^+$ abundance does not go down to 0% as the ion dissociates. This is believed to be due to the fragment $SiC_3H_6F^+$ which results from further dissociation of the H-loss ion. This was not corrected for either in **Figure 2.5**. No further dissociations are seen in this breakdown diagram. From now on, breakdown diagrams are always corrected for the H-loss so that the parent peak goes down to 0%.

2.2 Methods

2.2.1 iPEPICO measurements

The iPEPICO apparatus is located at the vacuum ultraviolet (VUV) beamline of the Swiss Light Source at Paul Scherrer Institut, Villigen. It operates with a photon resolution of 2 meV and threshold electron kinetic energy resolution of about 1 meV [44]. It is therefore capable of determining the dissociative photoionization onset energy with accuracy of 1 meV. The apparatus has been presented in detail [17] so its instrumental features will not be described here further.

2.2.2 Computational methods

Computational calculations were performed to construct the calculated breakdown pathways of the molecules. The target is to obtain the zero point energy at 0 K for all molecular and ionic species concerned. These species of the breakdown paths are the so-called stationary points. They are of two different types, based on their location in their potential energy diagram. These are local minima and transition states:

- *Fragments located at minima on the potential energy surface*: A geometry optimization is performed on the fragment, followed by calculations to obtain the numerical harmonic vibrational frequencies in the respective optimized geometry. If the geometry is a true minimum on the energy surface, all the vibrational frequencies have a positive value. The dot on the surface in **Figure 2.7** is located at a local minimum. [2]

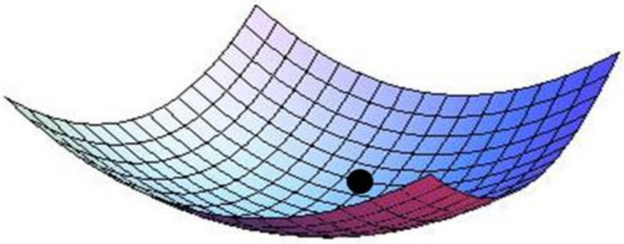

Figure 2.7 A minimum on a potential energy surface.

- *Fragments located at a saddle point on the potential energy surface*: To obtain the true transition state of a bond cleavage, a relaxed surface scan is performed on the ionic fragment. With this method, the distance between two atoms is changed stepwise and a geometry optimization carried out for each step while keeping the respective bond distance constant. Energy values obtained from the scan only include the electronic energy of the system but not the zero point energy. It is added to the true transition states and minima afterwards. If the energy curve obtained from the relaxed surface scan seems to include a transition state, an optTS calculation is performed on the geometry having the highest energy. The optTS method searches for the geometry located on the nearest point on the energy surface having a tangent with zero slope, which is generally a saddle point. If this geometry is a true transition state, one of its vibrational frequencies has a negative value and its motion describes the geometric path of the transition state. The arrow on the surface in **Figure 2.8** describes the energy path chosen when a bond cleavage contains a transition state.

---

[2] **Figure 2.7** and **Figure 2.8** were taken from this website: http://commons.wikimedia.org/wiki/File:Minima_and_Saddle_Point.png

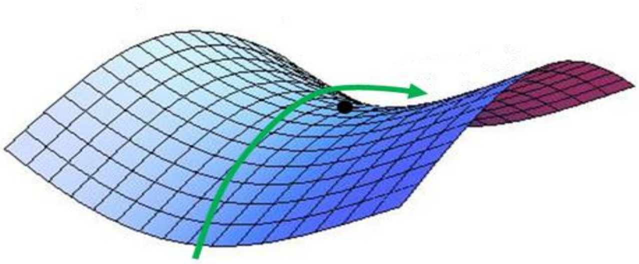

Figure 2.8 A saddle point on a potential energy surface.

All values displayed in the calculated breakdown energy diagrams provide only energy differences between the neutral molecule and the respective state. In order to obtain breakdown energy diagrams comparable to the experimental results, thermal corrections are made to the neutral molecule and the parent ion but not to the products from the dissociation reactions. This means that the molecule is originally at 298 K. When it gains the photon energy, it will be capable of contributing its thermal energy to the energy needed for bond dissociation. All the available energy, including the thermal energy of the molecule, is used for the dissociation. Consequently, the fragments produced do not contain any thermal energy and are therefore at 0 K. Information about the 0 K energy and the thermally corrected energy at 298 K is included in the results from the numerical frequency calculations so a separate calculation was not needed.

When a cleavage of a molecular bond does not contain a transition state, the energy required for the cleavage is interpreted as the energy difference of the neutral molecule and the geometry optimized products, but not the energy of the products occupying the unchanged geometries. The reason is that while the distance between the two fragments increases they simultaneously acquire the lowest energy geometry possible, so the lowest possible energy state is followed throughout the cleavage process.

All DFT calculations; geometry optimizations, relaxed surface scans and single point energy calculations were performed with the ORCA program computational chemistry software, version 2.9 [45]. The geometry of all molecules and fragments was optimized using the density functional theory (DFT) calculations based on the PW6B95 hybrid functional with DFT-D3(BJ) dispersion correction. The def2-TZVP basis set was used in all cases and calculations used the RIJCOSX approximation with def-TZVP/J auxiliary basis set. Calculated numerical harmonic vibrational frequencies were used to calculate zero-point and thermal corrections to enthalpy and free energy. All mentioned functionals, basis sets and other features are implemented in the ORCA program suite. Input files were generated in the freeware Gabedit [46], a graphical user interface for computational chemistry software. The program supports ORCA and offers the user, for example, to edit, display and analyze molecular systems. An example for an input file generated in Gabedit is given in appendix E. For exclusive visualization of the computed results, the graphical program Chemcraft, version 1.7 [47] was used. All molecular figures in this project are images exported from Chemcraft. The program was particularly useful to determine whether geometries were true transition states by playing the animations of their negative vibrational frequency.

A complete list of all fragments, their 0 K energy and 298 K thermally corrected energy is given in appendix H.

2.3 Review of breakdown pathways

There are few possible breakdown pathways for the monohalogenated silacyclohexanes. As can be seen in **Figure 2.9**, each carbon atom is identified with a number from 2 to 6 while the silicon atom has the number 1. The symmetry of the six membered ring systems simplifies them a little bit. It causes the two carbon atoms adjacent to the silicon atom, C2 and C6, to be identical, as well as carbon atoms C3 and C5. This symmetry usually breaks up when the dissociation process begins.

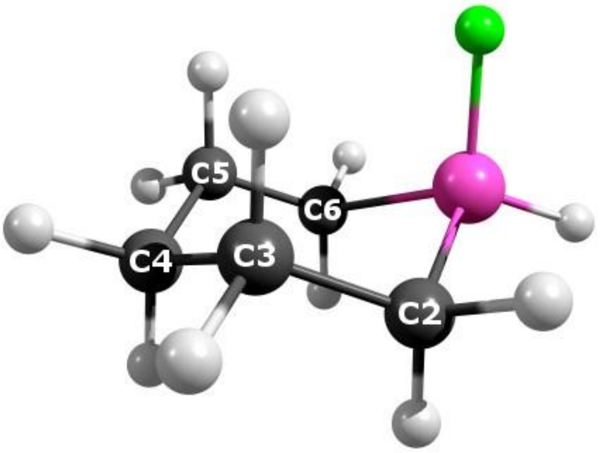

Figure 2.9 $(CH_2)_5SiHX$ showing numbering of carbon atoms.

As discussed in the introduction, the dissociative ionization takes place when the gaseous molecule is bombarded with an energy selected photon. When the energy of the photons is increased, the first event to occur is the ionization of the molecule. As the input energy increases, bonds with higher bond energies are cleaved.

The first bond dissociation either opens up the six-membered ring or cleaves the molecule apart. When a fragment is cleaved from the molecular ion, the positive charge always stays on the silicon containing fragment. This was verified by computing the energy of the same fragments having switched charges, keeping the silicon containing fragment neutral. The energies of the resulting systems were considerably higher than when the charge was located on the silicon containing fragment. Compared to the experimental results, this was as expected, since non-silicon containing fragment were never detected in the mass spectra. Accordingly, the most loosely bound electron of these molecules is located on the silicon atom, which also is the most electropositive atom.

First dissociation resulting in opening of the ring

There are three possible 1st dissociations that would result in the opening of the ring without changing the mass of the detected cation. These are

- Si-C2 bond cleavage
- C2-C3 bond cleavage
- C3-C4 bond cleavage

In order to identify which cleavage requires the lowest onset energy, the cleaved structures were geometry optimized and their final single point energy compared to the energy of the uncleaved neutral molecule. These energy differences are the sum of the ionization energy and the bond breaking energy and are interpreted as the bond dissociation threshold. They are compared for each ring system in **Figure 2.10**.

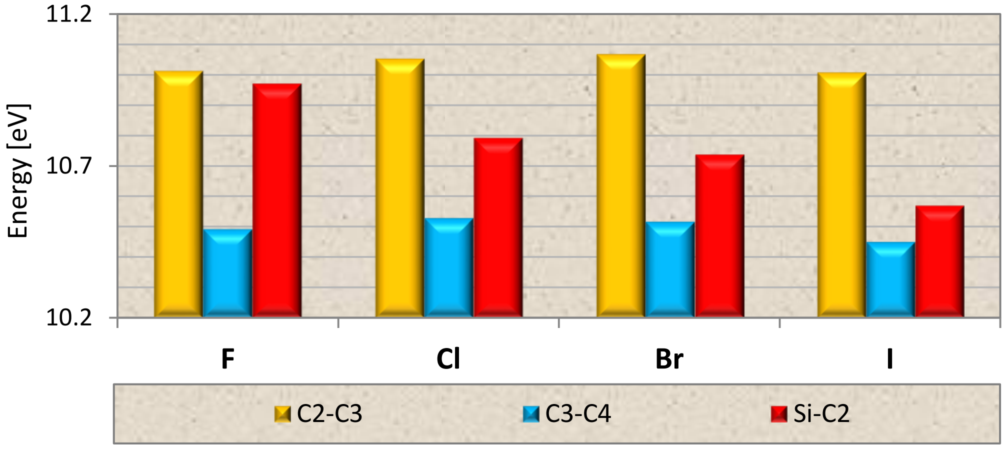

Figure 2.10 Calculated bond dissociation energies of the ring opening cleavages.

The comparison reveal that the C3-C4 bond cleavage is most favourable and the C2-C3 bond cleavage is least favourable in all cases. Both the C3-C4 and the C2-C3 bond cleavage requires a virtually constant energy for all four halogen-substituted rings. Conversely, the Si-C2 bond dissociation threshold decreases as the electronegativity of the halogen atoms decreases and thereby decreasing the polarization of the Si-X and Si-C2 bonds. The higher energy C2-C3 and Si-C2 bond energies will not be discussed further since their cleavage is not a part of the experimental breakdown paths, but the lowest energy C3-C4 bond cleavage has sequential dissociation pathways that will be discussed in detail.

First dissociation resulting in a molecular cleavage

Additional to the C3-C4 bond cleavage, two other 1st dissociations are possible. If either the halogen or one hydrogen atom is cleaved off, the ring itself is intact but the resulting ionic fragment has a lower mass:

- Si-X cleavage
- H atom loss (7 different cases)

Characteristic of the Si-X cleavage is that the resulting ionic fragment is the same for all four halogen-substituted rings and the symmetry of the resulting ionic fragment is the same as for the parent ion.

The molecule has a total of eleven hydrogen atoms but the symmetry reduces the number of distinct hydrogens to seven. It is necessary to discriminate between the axial and the equatorial positions of the hydrogen atoms, making the seven distinct H atoms the following:

- Si-H
- C2-H_{ax} and C2-H_{eq}
- C3-H_{ax} and C3-H_{eq}
- C4-H_{ax} and C4-H_{eq}

In order to identify which of the hydrogens are the most likely to be cleaved off, it was decided to calculate and compare the dissociation energies of every distinct hydrogen cleavage. These calculations were performed for all four halogen-substituted rings as well as the non-substituted ring. The hydrogen-cleaved structures were geometry optimized and their electronic energy compared to the electronic energy of the intact neutral molecule. The results are summarized in **Figure 2.11**.

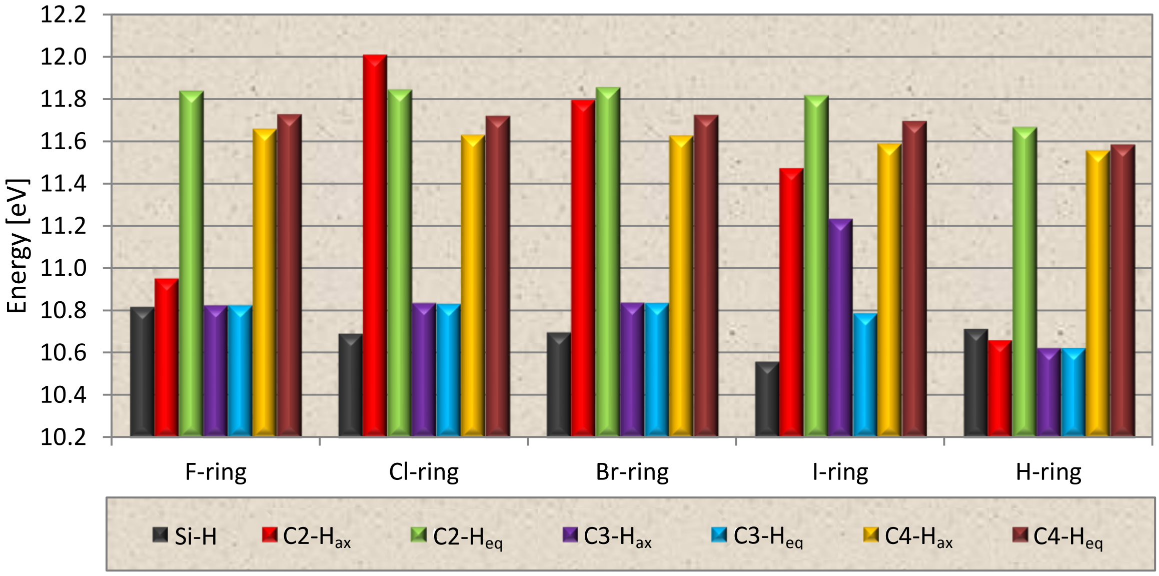

Figure 2.11 Comparison of the calculated dissociation energies for all hydrogen cleavages.

In all cases but the unsubstituted ring, the lowest energy required to cleave a single hydrogen atom from the molecule corresponds to the Si-H bond. Other feature seen in the figure is also of great interest. It is the vast energy differences ranging from 10.56 eV up to 12.01 eV. Therefore it was decided to take a better look at the geometry optimized structures resulting from the elimination of the H atoms from all the four halogen substituted rings and the results are summarized in **Figure 2.12**. The geometries for the Br-substituted ring are omitted from the figure as it behaves identically to the Cl-substituted ring. **Figure 2.12** illustrates nicely the reasons for the great energy differences seen in **Figure 2.11** and the exceptions from the trends. Three facts are worth pointing out:

1. The low energy required to cleave the C2-H_{ax} bond in the F-ring and in the unsubstituted ring is accounted for by the H-shift from C3 to C2 in the remaining cations. A very different geometry is reached in the Cl-, Br-, and I-rings, where the halogen atom in the remaining cation moves towards carbon C2 to offer stabilizing effect. This can be explained by the size of the larger halogens and thereby their longer Si-X distance.
2. As in the above example, when cleaving the C3-H_{ax} bond, the ions reaches a geometry where the C2 and C3 carbon atoms are η^2-bonded to the Si atom. The size of the I atom and the great Si-I distance makes the I atom shift towards C3, ending up η^3-bonded to Si, C2 and C3. For the lighter halogens the η^2 geometry is much lower in energy, explaining the high C3-H_{ax} bond dissociation energy for the I-ring.
3. In general, the stabilization gained by having the C2 and C3 carbon atoms η^2-bonded to the Si atom is energetically favourable. Apart from the I-substituted ring, this geometry is reached in the case of both axial and equatorial C3-H cleavage and explaines their low bond dissociation energy. Stabilizing geometry changes are not as efficient when cleaving the C4-H_{ax}, C4-H_{eq} or C2-H_{eq} bonds.

The geometrical results summarized **Figure 2.12** were only illustrated for general interest and have negligible connection to the main issue of this project so they will not be discussed further.

The breakdown pathways will be divided into three chapters which are classified by the first bond breakage of the respective pathway. These are the C3-C4 ring opening, the X-loss, and the Si-H cleavage.

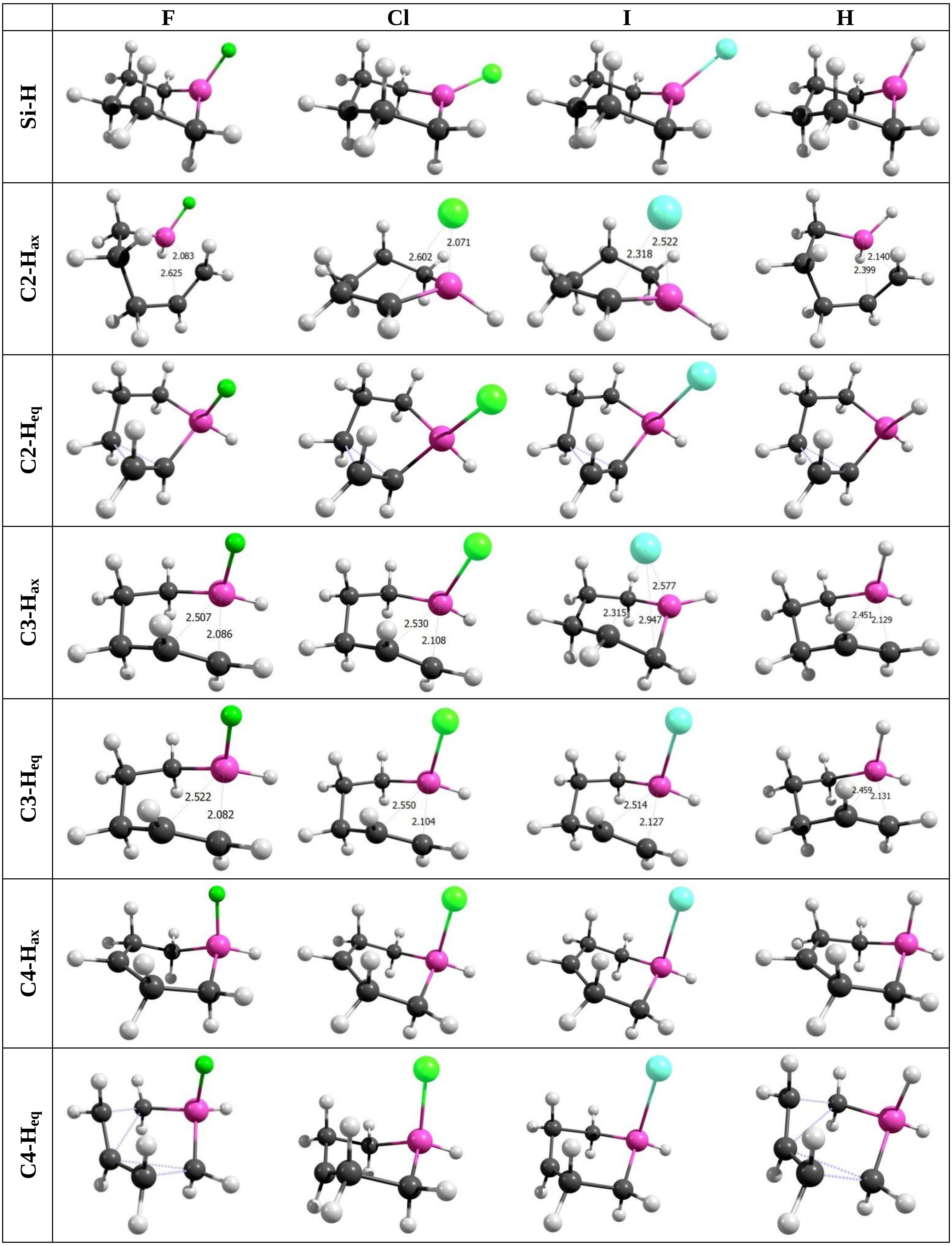
F
Cl
I
H
Si-H
C2-H$_{ax}$
2.083
2.625
2.602
2.071
2.318
2.522
2.140
2.399
C2-H$_{eq}$
C3-H$_{ax}$
2.507
2.086
2.530
2.108
2.577
2.315
2.947
2.451
2.129
C3-H$_{eq}$
2.522
2.082
2.550
2.104
2.514
2.127
2.459
2.131
C4-H$_{ax}$
C4-H$_{eq}$

Figure 2.12 Geometry optimized ions resulting from the elimination of different H atoms.

2.3.1 Pathways of C3-C4 ring opening – A geometrical approach

In the case of the F-, Cl-, and Br-rings, the C3-C4 bond has the lowest bond dissociation threshold. By making a relaxed surface scan, described in the computational methods chapter, the transition state of the bond cleavage was calculated. As seen in the energy diagram from the relaxed surface scan (**Figure 2.13**), the energy of the system increases while the C3-C4 bond is elongated. At a certain bond length the energy reaches a maximum. By increasing the bond length further, the energy decreases again and reaches a minimum at geometry where the C2 and C3 carbon atoms are η^2-bonded to the Si atom. The difference between the transition state and the following minimum state is small, in terms of both the geometry and the energy difference.

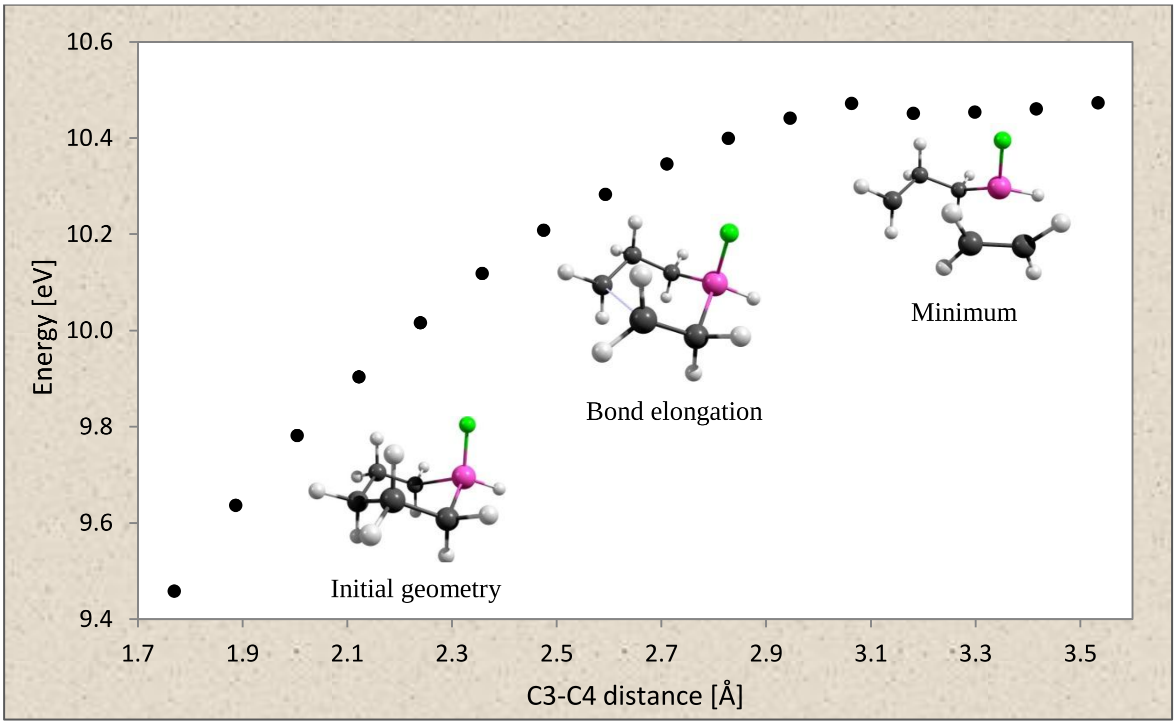

Figure 2.13 Energy diagram of the relaxed surface scan of increased C3-C4 bond distance. Example showing the F-substituted ring.

When the C3-C4 bond has been broken, two following breakdown pathways are possible:

- C_2H_4 cleavage
- C_3H_6 cleavage

The resulting ionic fragments for both pathways were detected in the measured breakdown diagrams for X = F, Cl and Br, to an unequal degree depending on the halogen.

C_2H_4 cleavage

After the C3-C4 bond breakage, the C_2H_4 ethylene fragment containing carbon atoms C2 and C3 is η^2-bonded to the Si atom. Without the ethylene, the remaining four-membered fragment was geometry optimized, converging to the geometry of a four-ring from being in a chain configuration. Therefore, it was believed that the C_2H_4 fragment loss requires the formation of a four-membered ring as illustrated in **Scheme 2.1**.

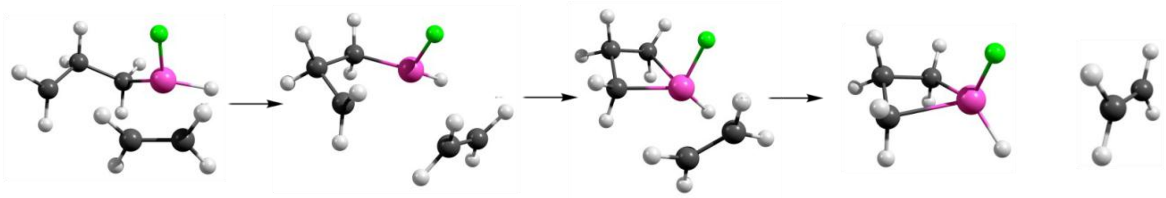

Scheme 2.1 The transition state of the C_2H_4 loss is the formaton of a four-membered ring.

By exploring a relaxed energy surface scan for the combined fragments, decreasing stepwise the bond distance between the Si atom and the C4 carbon atom, it was verified that formation of the four-membered ring truly is the transition state of the ethylene cleavage. The direction of the scan is from the right to the left in **Figure 2.14** since the distance between the Si atom and the C4 atom is decreased stepwise.

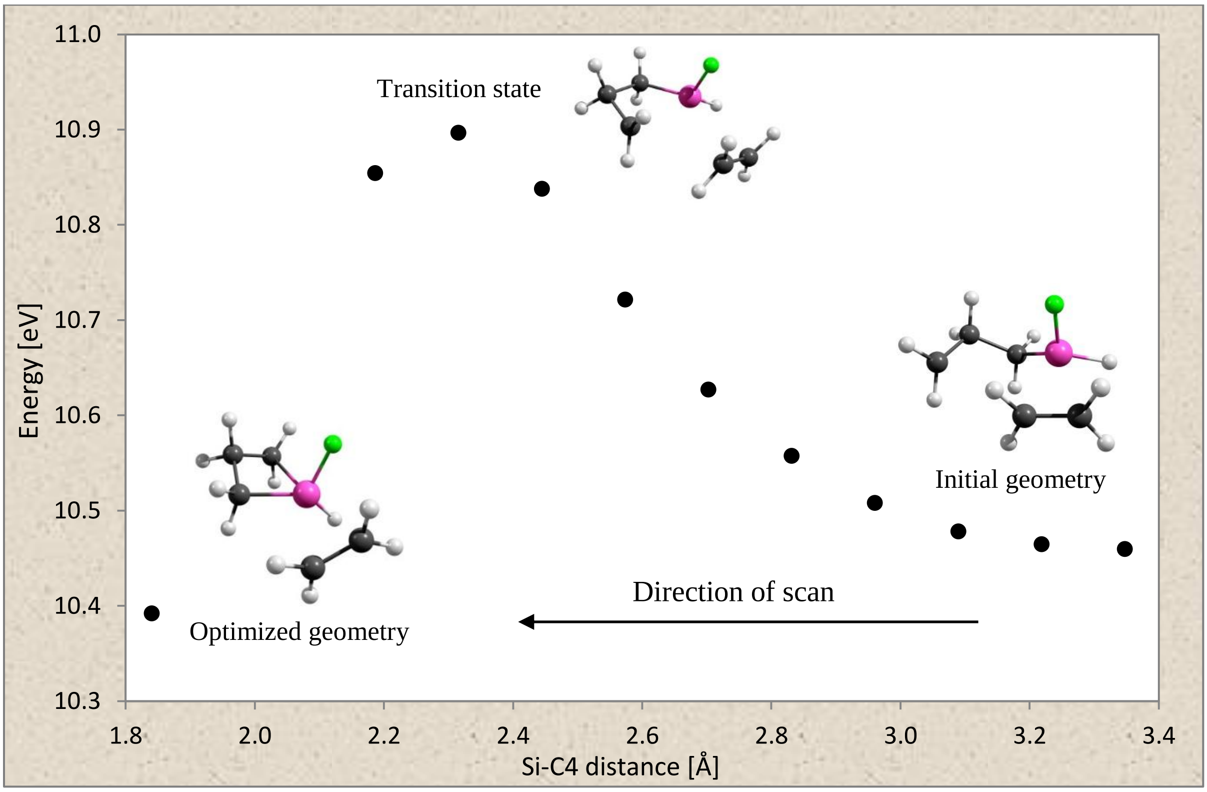

Figure 2.14 Energy curve describing the formation of the four-membered ring. Example showing the F-substituted ring.

The single dot farthest to the left in **Figure 2.14** is not a part of the relaxed energy surface scan. It was obtained by performing a geometry optimization on the final step from the scan (at 2.19 Å). This resulted in a minimum having lower energy than the initial geometry of the scan, but only in the case of the Fl- and Cl-substituted rings. For some reason, doing the same geometry optimization on the Br- and I-substituted rings resulted in higher energy states. These states still had the features necessary to be defined as minima.

Following the ethylene loss, a second ethylene loss is possible from the four-membered ring.

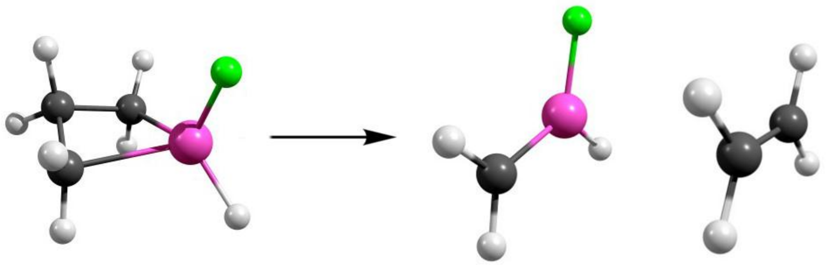

Scheme 2.2 Second ethylene loss.

C_3H_6 cleavage

Another breakdown pathway is possible after the C3-C4 bond breakage. Instead of cleaving off the C_2H_4 fragment which is η^2-bonded to the Si atom, the C_3H_6 fragment can be cleaved from the molecule. Geometry optimization was carried out on the C_3H_6 fragment showing a convergence to the geometry of a stable propene fragment. This requires a H-shift from the middle carbon atom to one of the terminal carbons. Since all carbon atoms in the initial geometry are bonded to two hydrogen atoms, the H atom shifts from the C5 carbon atom to either C4 or C6. Thus, two relaxed energy surface scans were run describing these two H atom transfers, showing the preferred hydrogen shift to be towards the C4 carbon atom as illustrated in **Scheme 2.3**.

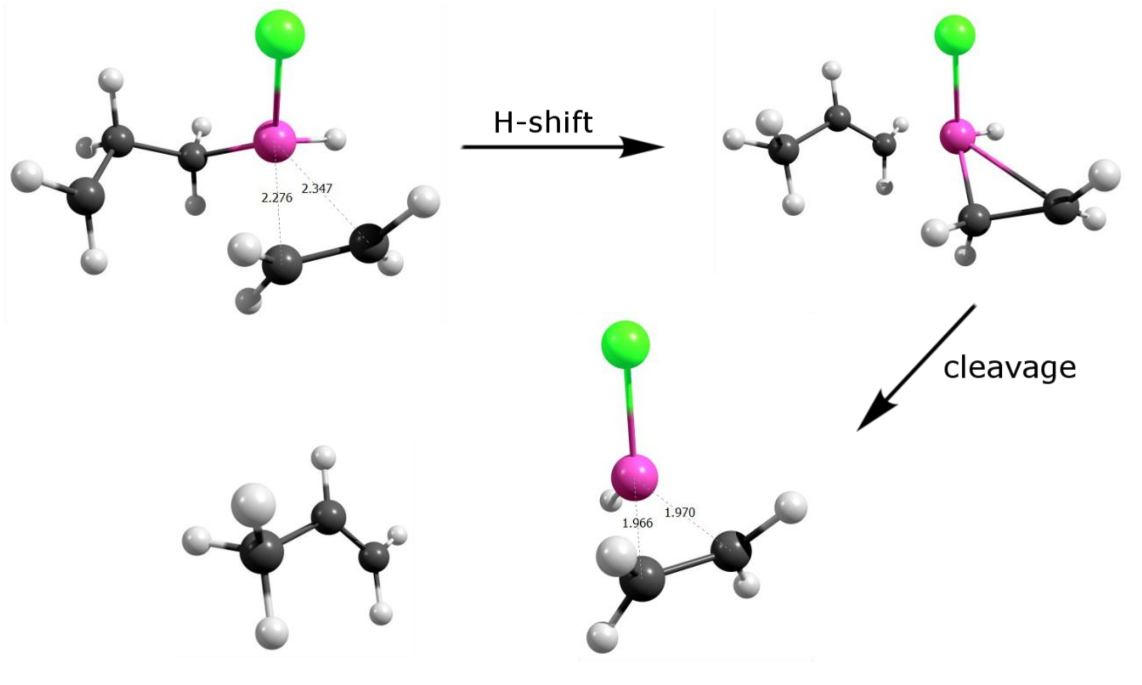

Scheme 2.3 H-shift from C5 to C4 followed by a propene loss.

The geometry of the cleaved structures in **Scheme 2.3** were found by performing geometry optimizations for both of the resulting fragments, C_3H_6 and $SiC_2H_5X^+$, separately. The energy curve obtained from the relaxed surface scan for the H-shift, containing both fragments (**Figure 2.15**) shows a clear transition state during the H-shift. The resulting geometry after the shift has a lower energy than before the shift. Four scans corresponding to all of the four halogen-substituted rings are displayed in **Figure 2.15** to illustrate the negligible energy difference between the four systems.

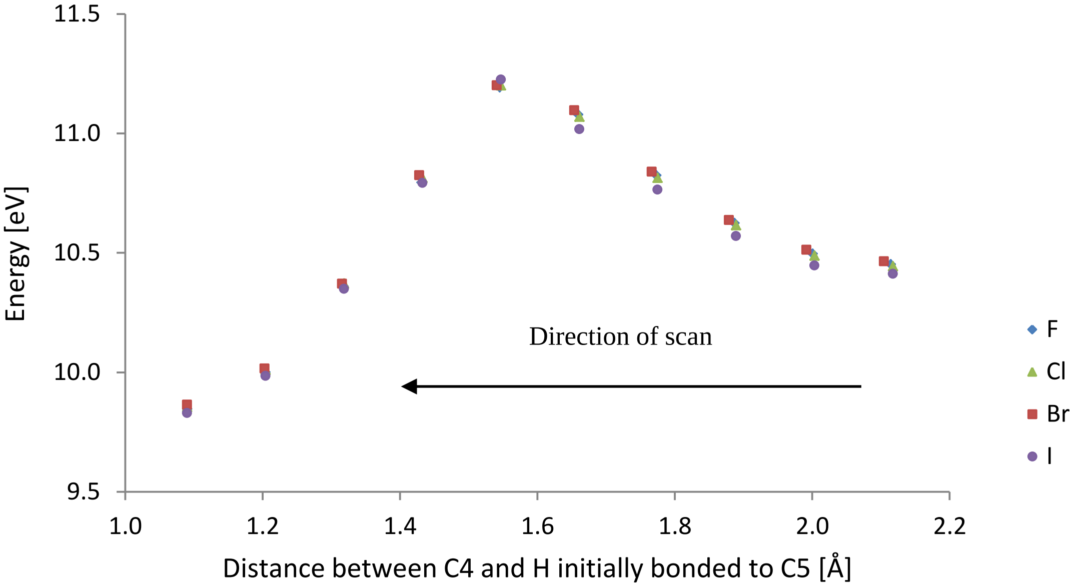

Figure 2.15 Energy curve describing the H-shift from C5 to C4.

The C_3H_6 cleavage with the rate limiting H atom transfer step goes through a higher energy transition state then the C_2H_4 cleavage rate limiting step of forming the four-membered ring. On the other hand, cleaving the propene away results in a lower minimum state where the silicon containing fragment has a strong η^2 bonding between the Si atom and the ethylene fragment. This can be seen by the shortened bond distance. In the case of the Cl-substituted ring, the Si-C2 and Si-C3 bond distances were 2.28 Å and 2.35 Å, respectively before cleavage and 1.97 Å after cleavage. This is summarized in **Table 2.1**.

Table 2.1 Change of bond distances during H-shift (Cl-substituted ring).

	Si-C2 [Å]	**Si-C3 [Å]**
Before H-shift	2.35	2.28
After H-shift	2.46	1.88
After cleavage	1.97	1.97

Experiments show that despite the C_3H_6 cleavage results in a lower energy minimum than the C_2H_4 cleavage, the latter is more likely to break off. This is due to the large difference in the energy barrier of the two transition states, the formation of the four-ring and the H-shift, respectively. Comparison for all the four substituted rings, F-, Cl- and Br- and I- is given in **Table 2.2** where the energies of the true thermally corrected transition states and minima are used. All numbers are given in units of eV, the barrier includes the ionization energy and the energy change corresponds to these steps exclusively.

Table 2.2 Thermally corrected barriers and energy changes of transition states. Values in [eV].

	4-ring formation TS (C_2H_4)		**H-shift TS (C_3H_6)**	
	Barrier	Energy change	Barrier	Energy change
F	10.574	-0.076	10.703	-0.657
Cl	10.482	-0.063	10.691	-0.593
Br	10.437	0.367	10.703	-0.754
I	10.363	0.277	10.669	-0.603

2.3.2 Pathway of X-loss – A geometrical approach

The special features of the halogen loss (**Scheme 2.4**) are that the molecule maintains its symmetry and the resulting ionic fragment is the same for all four halogen substituted compounds.

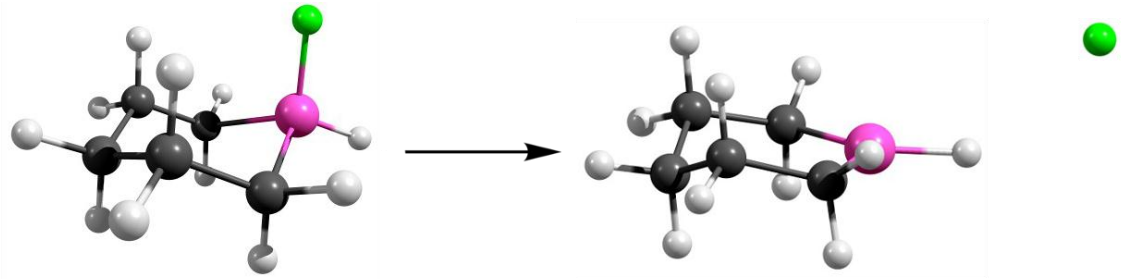

Scheme 2.4 Dissociation of the Si-X bond resulting in a symmetrical ionic fragment.

Relaxed surface scans were carried out for all four halogen containing rings. The results show that when expanding the distance between the silicon and the halogen atoms, the energy of the system increases and converges to a constant value but includes no transition state. During the dissociation, the remaining fragment simultaneously obtains a new configuration. This means that the energy curve for the cleavage is similar to a energy curve describing a simple bond cleavage in a diatomic molecule and the bond dissociation energy is the energy difference of the cleaved geometry optimized structure and the uncleaved neutral molecule.

A clear trend is observed when the four halogen-containing rings are compared in terms of the Si-X bond dissociation energy. The larger the halogen, the longer the silicon-halogen bond distance resulting in lower bond dissociation energy. This is summarized in **Table 2.3** and **Figure 2.16**.

Table 2.3 Si-X bond lengths compared to the Si-X dissociation energies.

	Si-X bond length	Dissociation energy
F	1.58 Å	12.99 eV
Cl	2.01 Å	11.30 eV
Br	2.17 Å	10.70 eV
I	2.46 Å	10.03 eV

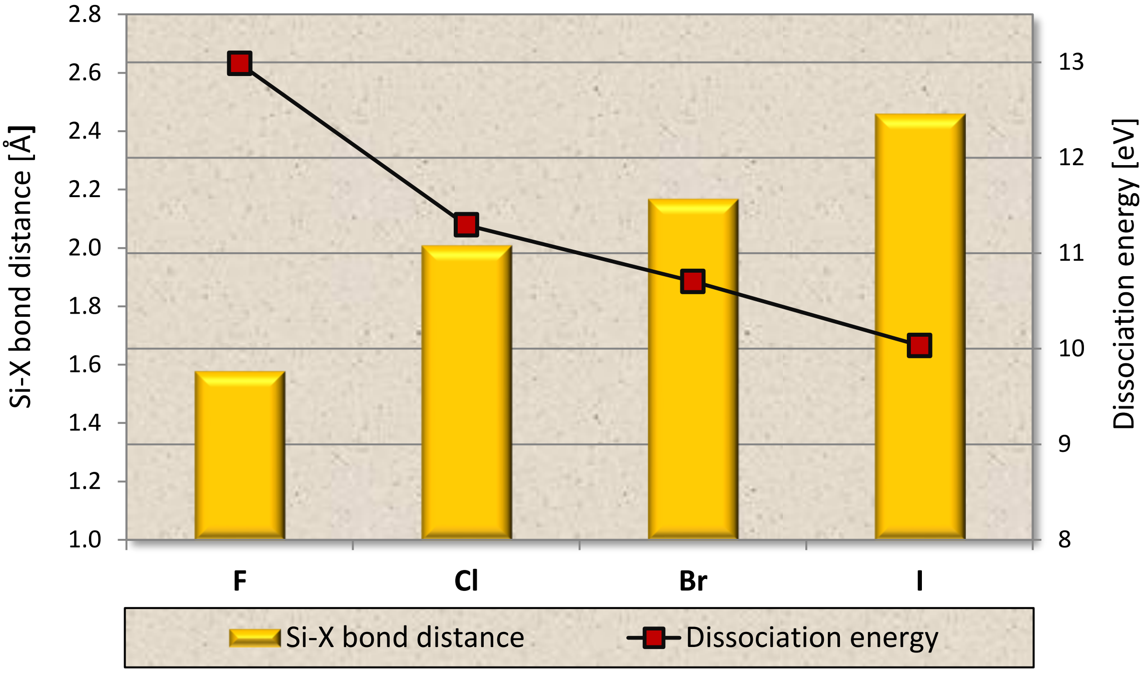

Figure 2.16 Si-X bond lengths compared to the Si-X dissociation energies.

After the halogen removal, the remaining species are the same in all four cases. Further possible breakdown pathways of the resulting fragment are analogous to the pathways following the C3-C4 cleavage mentioned above. This include ethylene and propene losses but as the former was the only of those two detected in the breakdown measurements, no calculations were run for the propene loss. As shown in **Scheme 2.5**, the ethylene loss includes the transition state of forming a four-membered ring.

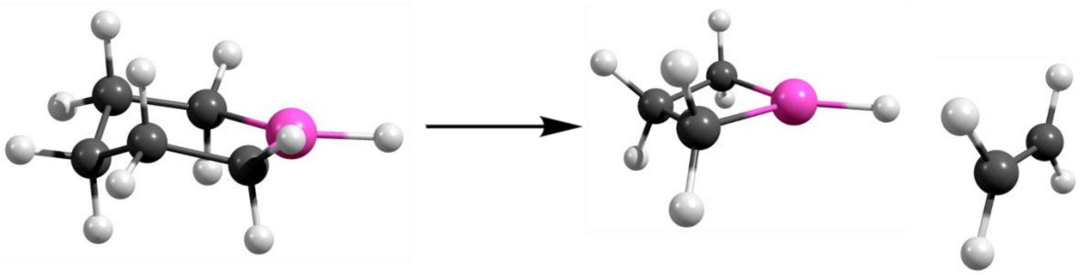

Scheme 2.5 Ethylene loss following a X-loss includes the formation of a four-membered ring.

2.3.3 H-loss

Despite the small mass difference of the parent ion and the H-loss ion, this dissociation was not the simplest to work with. To obtain the correct calculated dissociation threshold, the correct hydrogen atom had to be cleaved off. The determination of which hydrogen is lost was described in the introduction part of section 2.3, showing Si-H loss to be most favourable. Secondarily, the hydrogen cleavage had to be handled with care when constructing the breakdown diagrams as described in the data analysis chapter. The geometry of the dissociation is similar to the halogen loss as can be seen in **Scheme 2.6**, the remaining fragment constantly obtaining a new configuration during the dissociation.

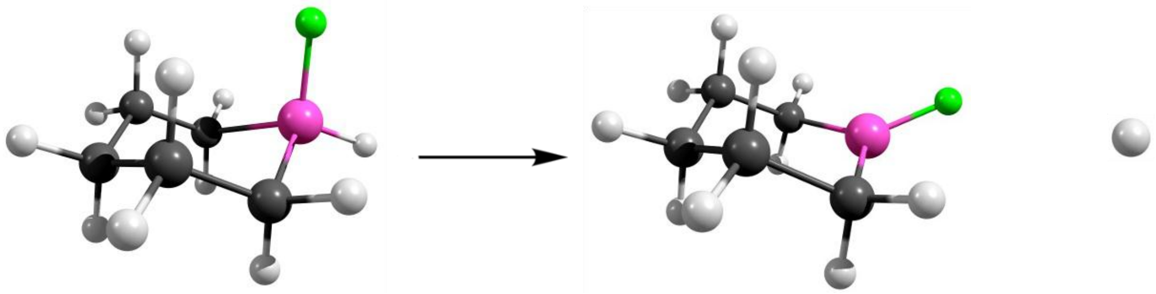

Scheme 2.6 Hydrogen loss. The hydrogen bonded to Si is most easily removed.

As the H-loss only accounts up to 10% fractional abundance, examination of its sequential dissociations was not performed.

2.4 Comparison

It is interesting to compare the energy required to cleave the C3-C4 bond and the Si-X bond. For the former, it is practically constant for all the four rings but the Si-X bond dissociation energy is lower for larger halogens. In the case of the F- and Cl-substituted rings, the C3-C4 bond dissociation energy is significantly lower than for the Si-X bond. Less difference is seen for the Br-substituted ring, the C3-C4 cleavage still being favoured, but for the I-substituted ring having the heaviest halogen, the energy required for the Si-I cleavage is lower than for the C3-C4 cleavage.

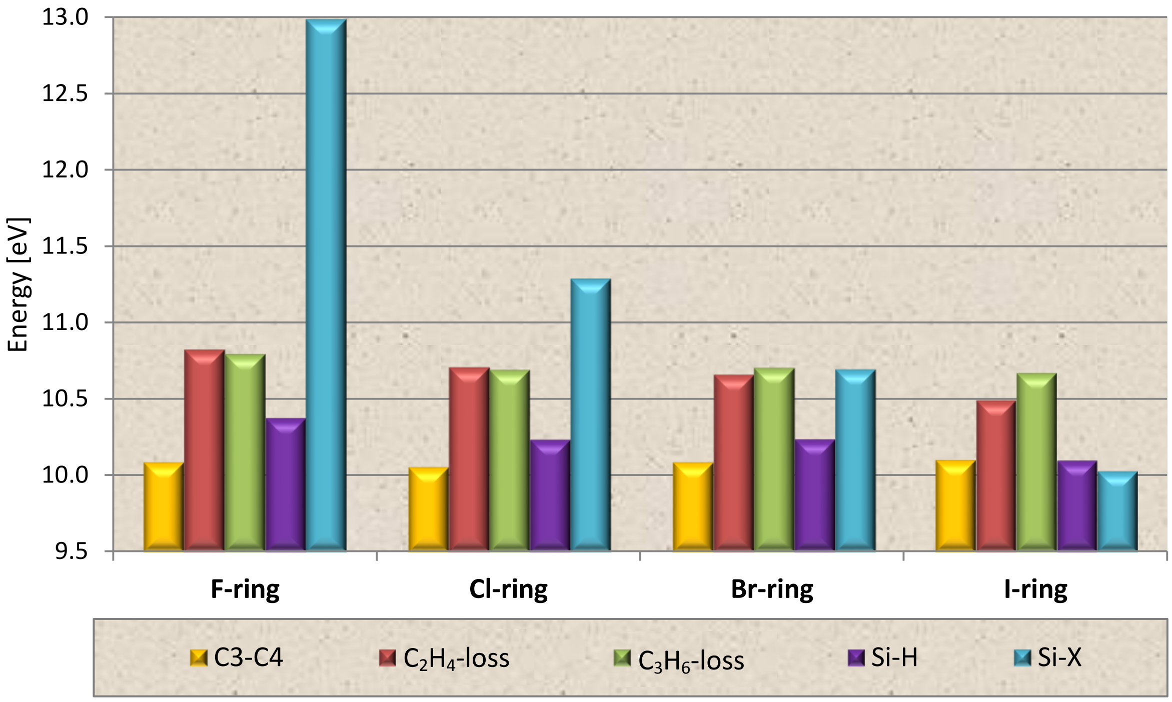

Figure 2.17 Comparison of the main calculated bond dissociation and fragment loss energies.

As the values summarized in **Figure 2.17** will be frequently referred to, they are also displayed in **Table 2.4** below. It should be mentioned that the dissociation energy for ethylene loss refers to the cleavage itself but for the propene loss, the transition state corresponding to the hydrogen shift is at higher energy than the cleaved structure.

Table 2.4 The main calculated bond dissociation and fragment loss energies, values given in eV.

	F-ring	**Cl-ring**	**Br-ring**	**I-ring**
C3-C4	10.08	10.05	10.08	10.10
C_2H_4 loss	10.82	10.70	10.66	10.49
C_3H_6 loss	10.79	10.69	10.70	10.67
Si-H	10.43	10.23	10.23	10.10
Si-X	12.99	11.30	10.70	10.03
2x C_2H_4 loss	12.54	12.29	12.21	12.00

2.5 Calculated breakdown energy diagrams

For each halogen-substituted ring, calculated dissociation pathways are summarized schematically in the four following breakdown energy diagrams. All energy values in these diagrams correspond to the true transitional states and minima. In each diagram, the energy value of the parent ion has been thermally corrected to 298 K. Also, the zero point energy has been added to the energy values of all ionic fragments to represent ions at 0 K. As can be seen in the diagrams, the energy scale does not begin at zero. The energy of the parent ions corresponds to the calculated ionization energy which is the energy difference of the ion at 298 K and the neutral molecule at the same temperature (discussed in section 2.7). This means that the zero energy value on the vertical scale is defined as the total energy of the neutral molecule at 298 K.

Further discussion about the calculated diagrams and the comparison of measured values will be given in sections 2.6.1-2.6.4.

2.5.1 F-substituted ring

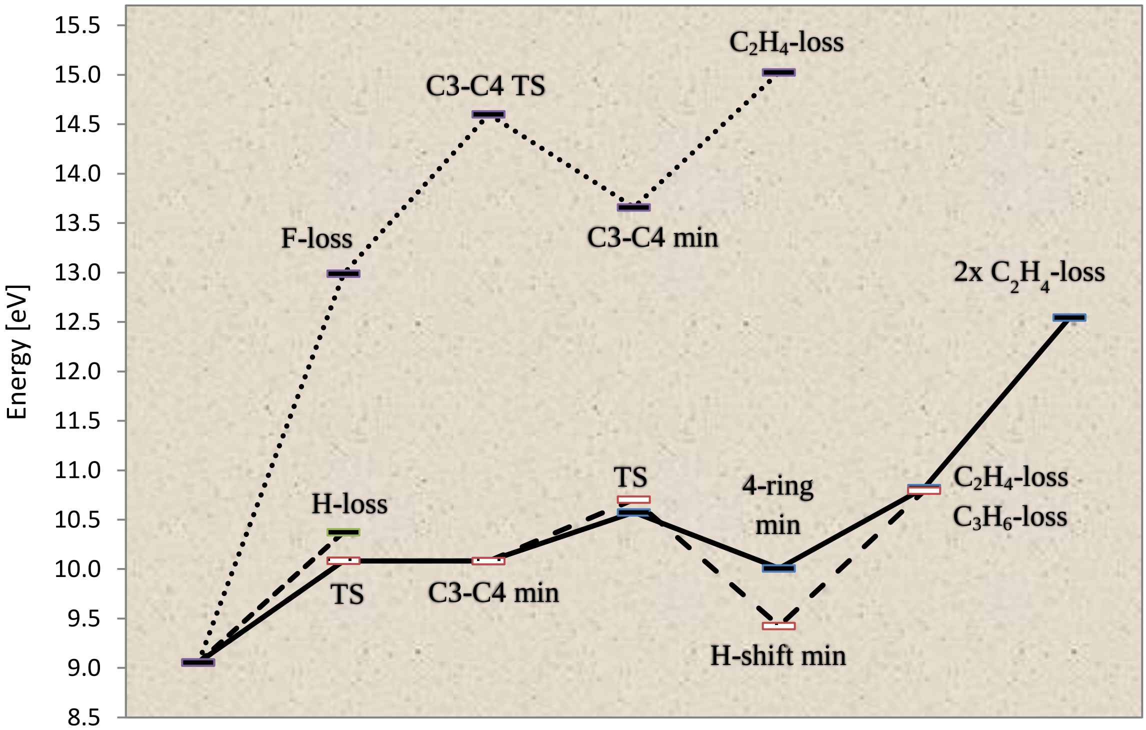

Figure 2.18 Calculated breakdown energy diagram of $SiC_5H_{11}F$.

2.5.2 Cl-substituted ring

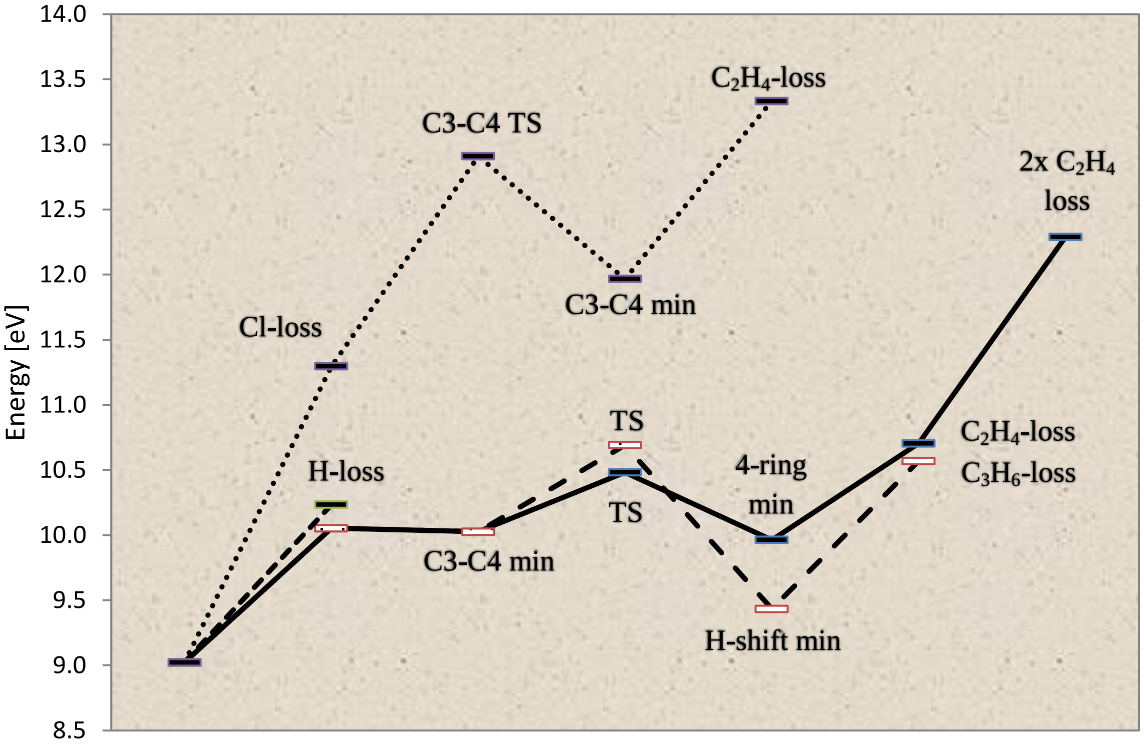

Figure 2.19 Calculated breakdown energy diagram of $SiC_5H_{11}Cl$.

2.5.3 Br-substituted ring

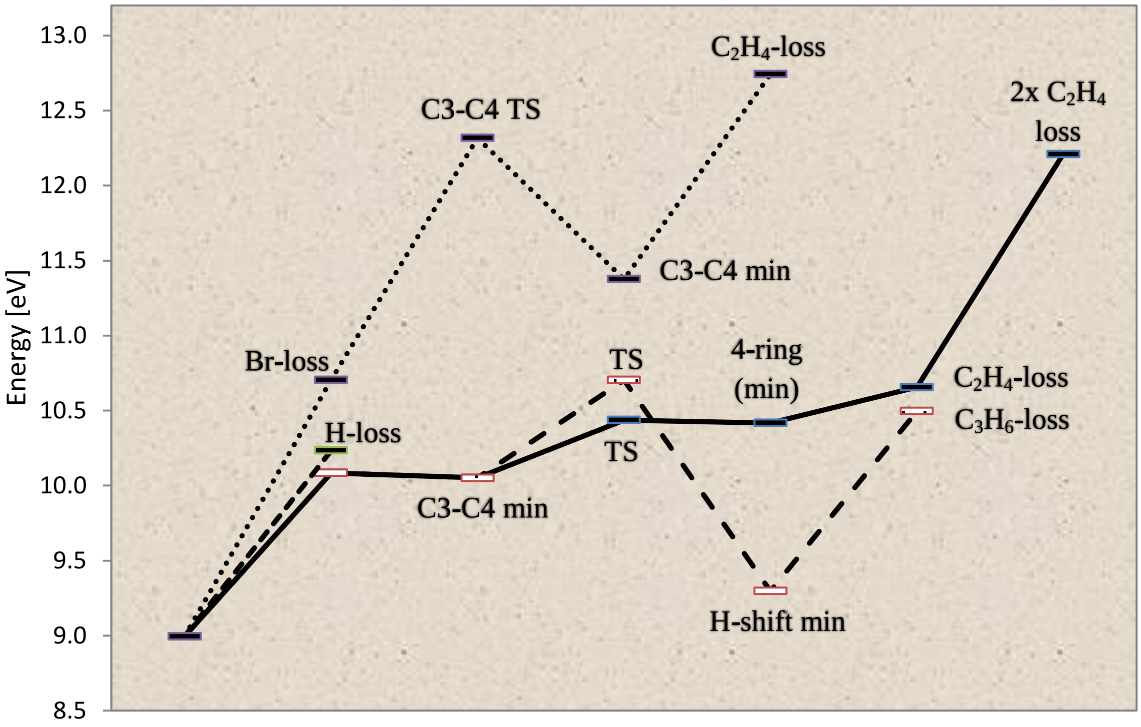

Figure 2.20 Calculated breakdown energy diagram of $SiC_5H_{11}Br$.

2.5.4 I-substituted ring

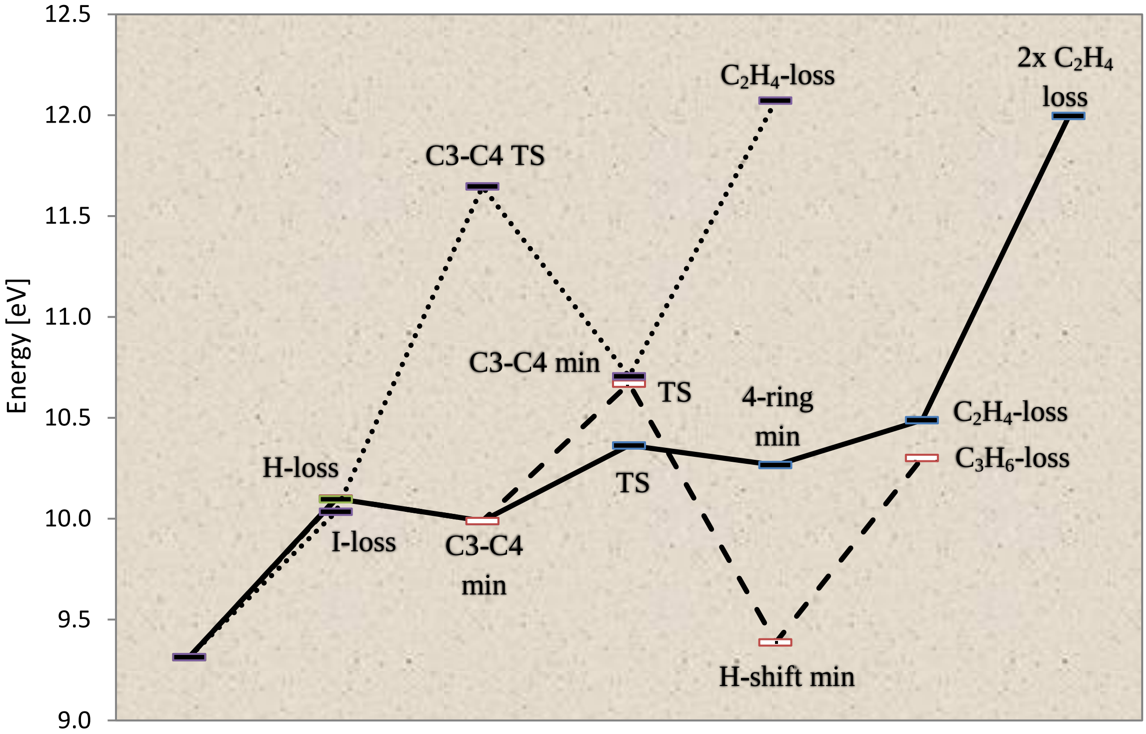

Figure 2.21 Calculated breakdown energy diagram of $SiC_5H_{11}I$.

2.6 Experimental breakdown diagrams

The iPEPICO experiments produce a vast number of data. When constructing the breakdown diagrams, some of the data points are omitted. This is done to make the appearance of the breakdown diagram smoother. In addition, if the fractional abundance of an ionic fragment does not reach 20%, it is sometimes omitted from the diagram but covered in the text. Nevertheless, the H-loss ionic fragment is always included because it had to be extracted from the parent mass ion peak through the COG analysis as described in section 2.1.1.

The bond dissociation energies cannot be read directly from the breakdown diagrams but have to be modeled to obtain values comparable to the calculated values. However, a rough comparison will be given in tables following every breakdown diagram to demonstrate the consistence of these two. The values in the right column of the tables are not absolutely true but are a visual estimation from the breakdown diagram. In the case of slow dissociations where the fractional abundance peaks rise very slowly, only the energy value corresponding to the appearance of the fraction peak is used as a guideline.

2.6.1 F-substituted ring

The breakdown diagram of the F-substituted silacyclohexane was described thoroughly in section 2.1.1 and will not be repeated here. In **Figure 2.22**, the breakdown diagram has been refined a bit. The propene loss curve has been omitted from the diagram. Its fractional abundance started to rise at about the same energy as the ethylene loss (**Figure 2.5**) and the H-loss curves but it only reached up to about 16%. The main ionic fragments detected are $SiC_3H_7F^+$, representing an ethylene loss which dissociates further by losing another ethylene, leaving the ionic fragment $SiCH_3F^+$.

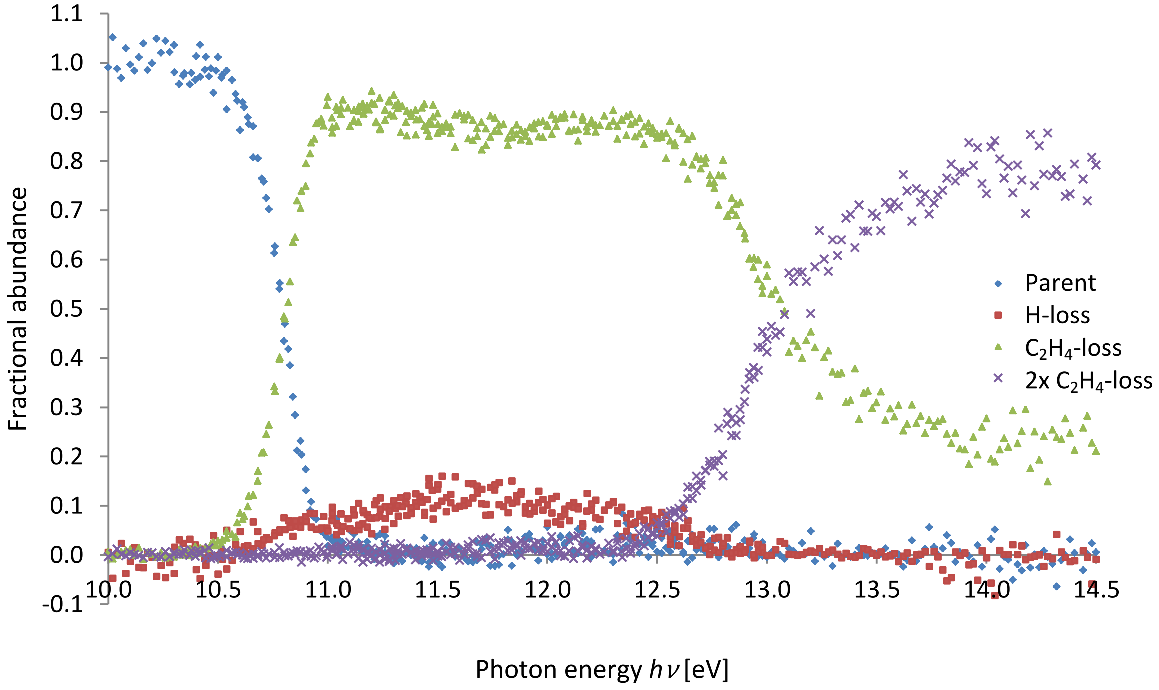

Figure 2.22 Breakdown diagram of $SiC_5H_{11}F$. The propene loss is omitted.

Overall, the breakdown diagram is in a good qualitative agreement with the calculated energy diagram (**Table 2.5** and **Figure 2.18**) since the lower limit of the experimental dissociation energy should be close to the correct value. The propene loss fragment peak which was omitted from the diagram is also shown in the table.

Table 2.5 Comparison of calculated and experimental breakdown values [eV].

	Calculation	**Experiment**
C_2H_4 loss	10.82	10.5-11.0
2x C_2H_4 loss	12.54	12.3-13.6
C_3H_6 loss	10.79	from 10.5
H-loss	10.43	from 10.5

2.6.2 Cl-substituted ring

The breakdown diagram for the Cl-substituted ring (**Figure 2.23**) is analogous to that of the F-substituted ring. The major difference is that the propene loss curve is now included. It rises up to a maximum of about 18%. Also, Cl-loss was detected, its peak starting to rise at about 11.8 eV, but it only rose up to 10% of the fractional abundance and it was omitted from the breakdown diagram.

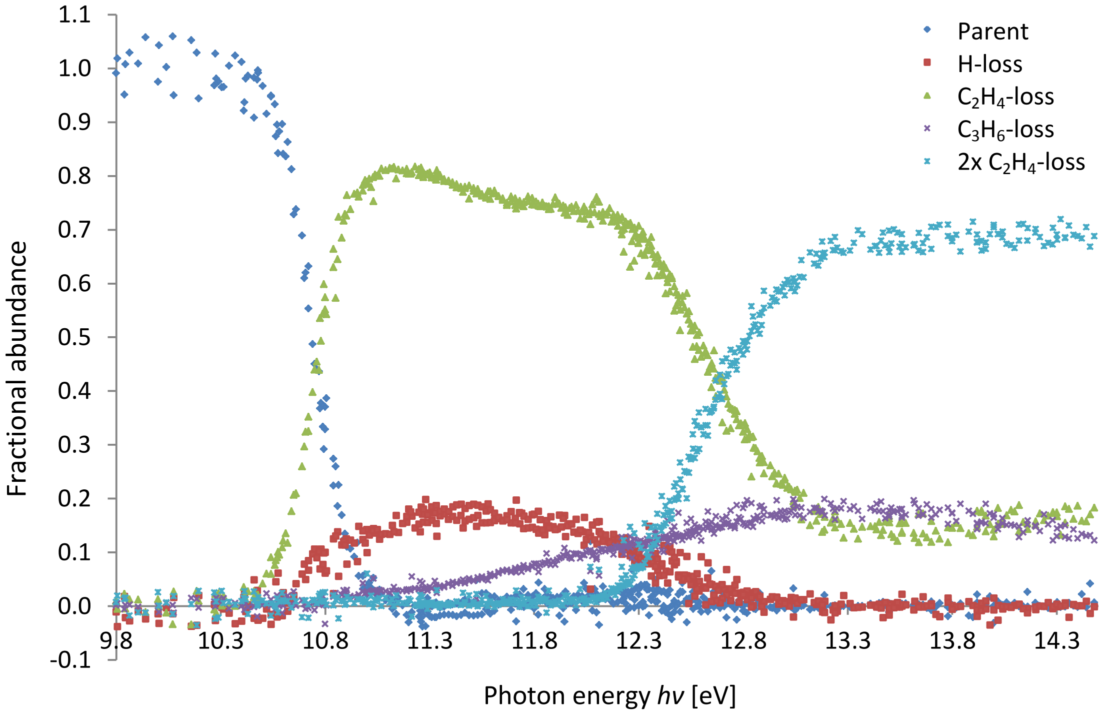

Figure 2.23 Breakdown diagram of $SiC_5H_{11}Cl$. The Cl-loss peak is omitted.

Since all observed dissociations, except the halogen loss, are slow, the photon energy where the ion starts to dissociate should be closer to the true dissociation energy value. The parent ion starts to dissociate by losing an ethylene fragment at around 10.4 eV, the fractional abundance of the parent ion going down to 0% at 11.0 eV. The second ethylene loss is detected between 12.1 and 14.3 eV. This is in good agreement with the calculated dissociation energies of 10.70 eV and 12.29 eV, respectively. The dissociations of the hydrogen, halogen and ethylene losses show slower rising fractional abundances, seemingly starting to rise at energies little higher than their real dissociation onsets. The values are compared in **Table 2.6**.

Table 2.6 Comparison of calculated and experimental breakdown values [eV].

	Calculation	**Experiment**
C_2H_4 loss	10.70	10.4-11.0
2x C_2H_4 loss	12.29	12.1-14.3
C_3H_6 loss	10.69	from 10.7
H-loss	10.23	from 10.4
Cl-loss	11.30	from 11.8

2.6.3 Br-substituted ring

The appearance of the breakdown diagram of the Br-substituted ring is very similar to that of the chlorinated ring. The only difference is that the halogen loss abundance rises up to 20% and is included in the diagram.

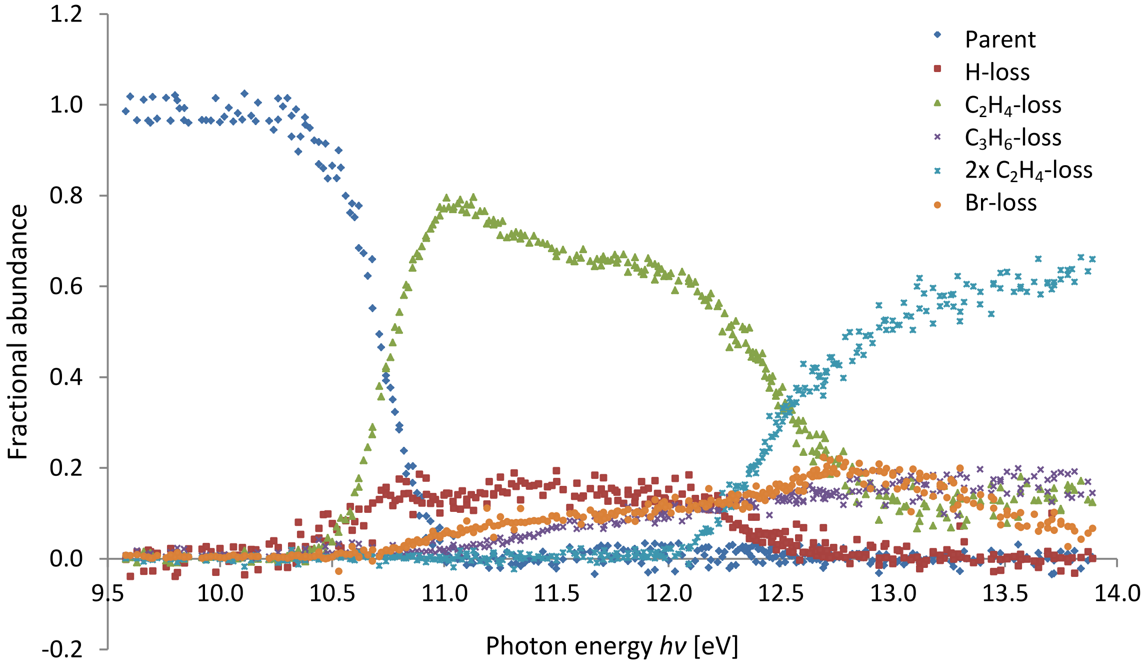

Figure 2.24 Breakdown diagram of $SiC_5H_{11}Br$.

As for the Cl-ring, the calculated value for both the first and second ethylene loss is in good agreement with the breakdown diagram. Also, the calculated dissociation energies for the slower dissociations are a bit lower than where their abundance peaks start to rise in the diagram.

Table 2.7 Comparison of calculated and experimental breakdown values [eV].

	Calculation	**Experiment**
C_2H_4 loss	10.66	10.3-11.0
2x C_2H_4 loss	12.21	from 12.0
C_3H_6 loss	10.70	from 10.9
H-loss	10.23	from 10.3
Br-loss	10.70	from 10.7

2.6.4 I-substituted ring

Of all the dissociations discussed in this project, only one can be considered as being a fast one. This is the iodine cleavage. For fast dissociations, the true dissociation threshold is more easily read from the experimental breakdown diagram. It is the energy value where the ion starts to dissociate. In a good correspondence to the calculated breakdown diagrams (**Table 2.8**), the first dissociation of the I-substituted ring is the cleavage of the silicon-iodine bond. This makes the appearance of the breakdown diagram for the I-substituted ring different from the others (**Figure 2.25**), showing a clear and fast first dissociation step with a subsequent fragmentation of an ethylene loss.

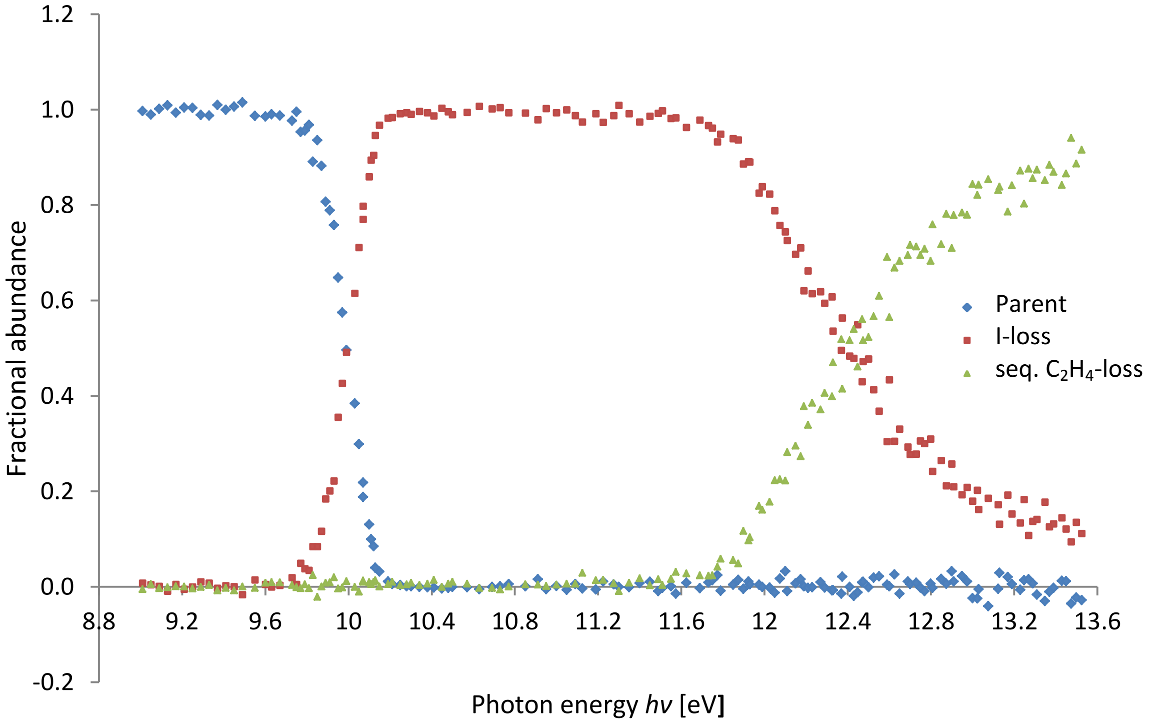

Figure 2.25 Breakdown diagram of $SiC_5H_{11}I$.

The first dissociation is detected at energy 9.7-10.2 eV in the breakdown diagram, giving good agreement with the calculated value of 10.03 eV. The sequential fragmentation is detected from 11.7 eV in the diagram but has a littler lower calculated value of 11.65 eV. This is in line with the energy comparison for the sequential dissociation of the other ring systems.

Table 2.8 Comparison of calculated and experimental breakdown values [eV].

	Calculation	**Experiment**
I-loss	10.03	9.7-10.2
Seq. C_2H_4 loss	11.65	from 11.7

2.7 Ionization energy and excitation spectra

Excitation spectra are extracted from the TPEPICO experimental data by plotting the absorption of the sample as a function of the photon energy. Processing only the ions corresponding to the threshold electrons, these spectra are commonly called Threshold Photoelectron Spectra (TPES) and clearly show the excitation pattern of the molecule (**Figure 2.26**). When the photon energy reaches the ionization energy of the molecule, the absorption starts to rise. The ionization energy is therefore easily read from the TPES.

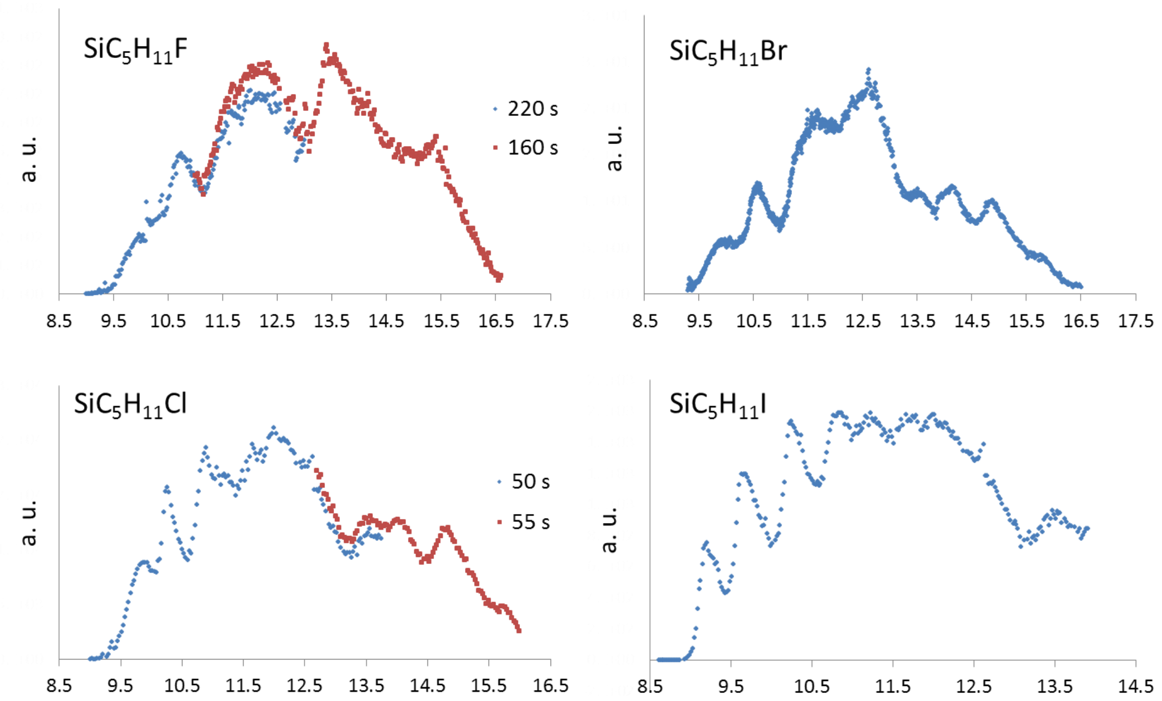

Figure 2.26 TPES showing the absorbtion as a function of photon energy.

Unequal absorption also explains the various scattering seen in the experimental breakdown diagrams. When the absorption is low, more scattering is seen in the breakdown diagrams. For a better comparison, TPES and BD for each halogen substituted ring are shown in appendices A-C. Ionization values read from the TPES and the calculated values are compared in **Table 2.9**. In all cases except for the I-substituted ring, the calculated value is about 0.2 eV lower than the experimental value. The opposite is detected for the I-substituted ring, where the calculated value is about 0.4 eV higher than the experimental.

Table 2.9 Comparison of calculated (at 298 K) and experimental values for ionization energy.

Substituent	Calculated [eV]	Experimental [eV]
F	9.06	9.24
Cl	9.02	9.33
Br	9.00	9.20
I	9.31	8.93

2.8 Modeling

As mentioned in section 2.2.1, by using the TPEPICO technique it is possible to determine the dissociative photoionization onset energy and the ionization energy with accuracy of 1 meV. But these accurate values cannot be read directly from the breakdown diagrams. The breakdown processes have to be modeled to obtain values comparable to the calculated results. A program, written by Sztáray, Bodi and Shuman, has been designed to fit experimental TPEPICO data in order to extract dissociation energies and dissociation rate constants [48]. The program analyzes the data from the spectroscopy experiments and models the processes by calculating various properties of the respective species, for example the energy distribution. For 15 years, the code has been used to analyze almost a hundred systems, the series CF_nBr_{4-n} (n = 0-3), studied by Kvaran's research group at the Science Institute being one example [49].

The modeling technique is the most specialized part of this project. Initially, the intention was to model the most common dissociations in order to have a good comparison to the calculated results. Despite months of effort trying to adopt the tactics of the modeling technique, I never acquired the skills to use it. One of my best examples of an input file is given in appendix F. It represents the ethylene cleavage from the F-substituted ring and a sequential loss of the same fragment. Various data are imported by the program, including the TOF distribution at various energies, data describing the experimental breakdown as well as rotational and vibrational constants of all respective fragments. At present, the modeling work is still incomplete. It was decided that a more experienced member of the research group would finish the modeling work.

3 Ansa complexes

3.1 Preparation of the precursors

Two precursors are needed for the synthesis of the target compound **3a**. One is 1,1-dilithinated ferrocene stabilized with N,N,N',N'-tetramethylethylenediamine (TMEDA) (**1a**) and the other is 1,3-bis(bromosilyl)propane (**2**).

3.1.1 The isolation of 1a

Due to the stability of ferrocene it is easily obtained commercially. Its reaction with *n*-BuLi lithinates each ring only once, giving 1,1'-dilithioferrocene when reacted with two molar equivalents of *n*-BuLi, as shown in **Scheme 3.1**. The use of TMEDA or 1,4-diazabicyclo[2.2.2]octane (DABCO) in the lithiation was published by Rausch and Ciappenelli in 1967 [50]. TMEDA forms a stable coordination complex with lithinated ferrocene but the distinct advantage of using TMEDA is that no monosubstituted products are obtained and the complex gets considerably more reactive in the metalation reaction than using the organolithium reagent alone, furthermore increasing the yield.

The lithiation takes place in a slurry solution where the only hexane solvent is from the 1.6 M *n*-BuLi solution as described by Bishop *et al.* [51]. TMEDA was used in 20% molar excess. It stabilizes the adduct by donating its nitrogen lone pairs to the lithium atoms.

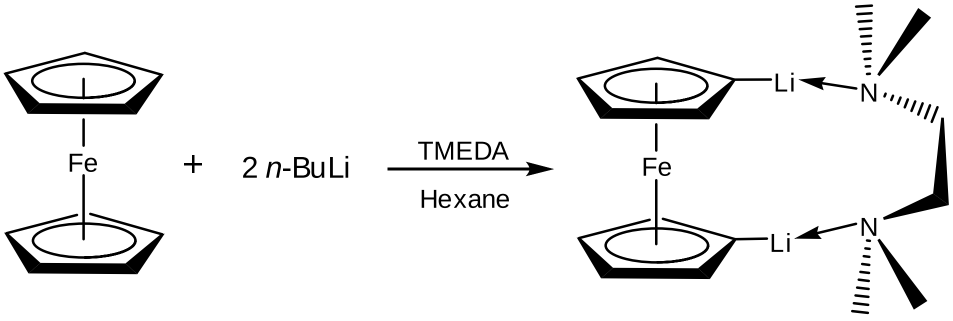

1a

Scheme 3.1 Dilithiation of ferrocene with *n*-BuLi and TMEDA.

The dilithiated ferrocene can be used *in situ* as was done in the first attempt. In subsequent preparations, it was isolated as the dry $(C_5H_4Li)_2Fe\cdot TMEDA$. The adduct is pyrophoric, so it was stored in a glovebox and all manipulations were conducted using either a glovebox or standard Schlenk technique. Attempts to take NMR spectra of **1a** were unsuccessful. It was readily dissolved in $CDCl_3$ but the only compound seen in the NMR spectra was ferrocene and impurities. Since the adduct is very reactive, it was believed to have broken down during the sample preparation or in the $CDCl_3$ solution. To verify if the compound really was the desired one, it was reacted with dichlorodimethylsilane in the known reaction [52] shown in **Scheme 3.2**.

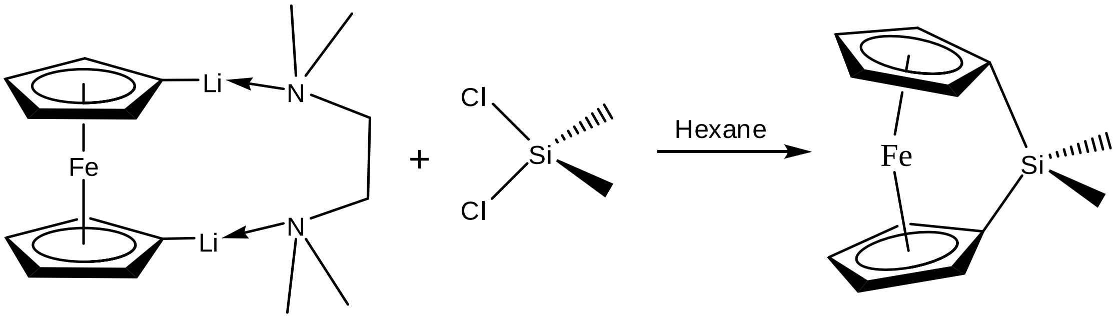

1a

Scheme 3.2 Reaction with $SiMe_2Cl_2$, done to test the purity of **1a**.

NMR spectrum of the product in CD_3CN is given in **Figure 3.1**. The desired product is clearly seen in the spectrum, giving peaks at 4.46 ppm, 4.14 ppm and 0.56 ppm, the same as reported in the reference. Unreacted ferrocene is at 4.16 ppm so the product peak at 4.14 ppm mainly falls thereunder but can still be detected as seen in the zoomed inset figure. The yield is not high but compared to the yield from the literature, 60%, it is acceptable.

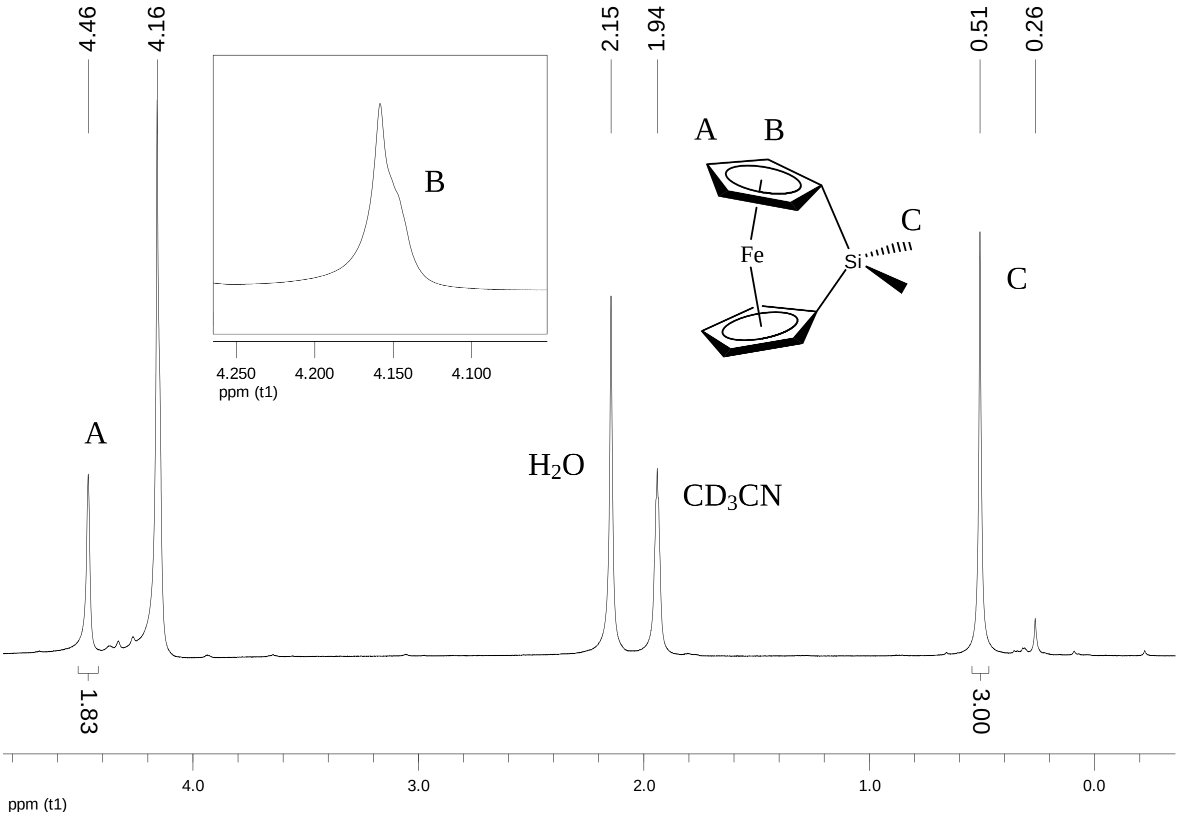

Figure 3.1 ^1H NMR spectrum of the product from the test reaction.

3.1.2 The preparation of 2

The precursor **2** was prepared as described by Mitzel *et al.* [53, 54]. It is done in the three step reaction as shown in **Scheme 3.3**.

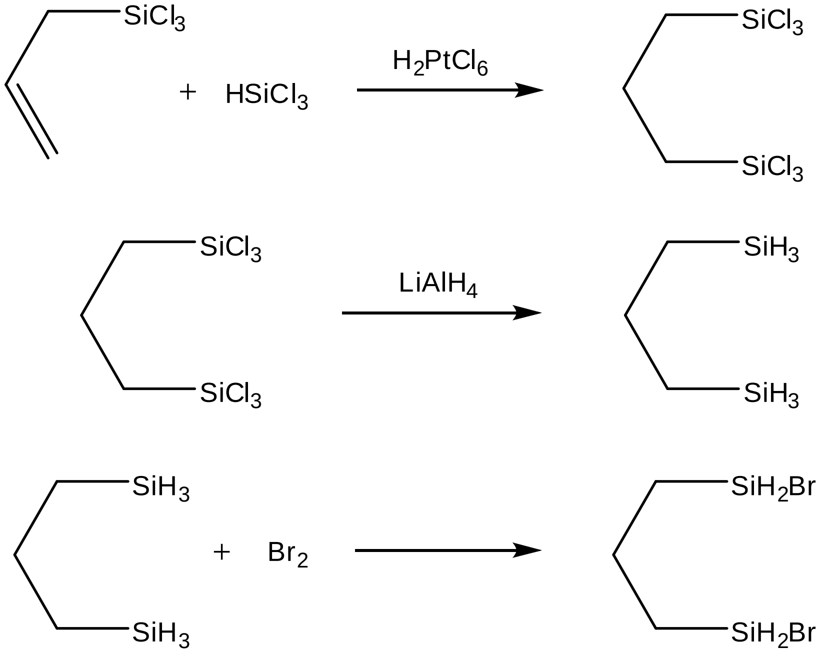

2

Scheme 3.3 Three step synthesis of **2**.

The first step includes the coupling of allyltrichlorosilane with trichlorosilane by using the Speier catalyst (0.1 M H_2PtCl_6 in 2-propanol). The 1,3-bis(trichlorosilyl)propane obtained is reduced to disilapropane with lithium aluminium hydride and thereafter dibrominated in the final step to yield the product. The main product is the dibrominated compound but mono-, and tribrominated products are also produced. The amount of the unwanted side product is kept at lower level by careful heat and speed control of the reaction, as well as using exactly two molar equivalents of the bromine. Fractional distillation using a Vigreux column at reduced pressure was carried out to separate the products, the desired dibrominated compound being the middle fraction. The fractional distillation was performed two times giving a quite pure final product. Its density was measured three times giving average value of 1.547 g/mL.

Mitzel et al reported a 57% total yield for all three reaction steps, making the total yield of 39% in this work fairly acceptable. The yields from each step from both the reference and this work are summarized in **Table 3.1**.

Table 3.1 Summary of the yields for the three step synthesis of **2**.

Step	Reference	This work
1	91 %	81 %
2	75 %	69 %
3	83 %	70 %
Total	57 %	39 %

3.2 Attempted synthesis of 3a

Silicon containing compounds bearing alkyl, aryl or heteroaromatic ligands linked to the Si atoms are easier to work with than those having only hydrogen bonded to the Si atom. Two SiH_2 units are contained in the bridging unit of compound **3a**. Their great reactivity is what makes the synthesis of the compound so challenging. All manipulations of both the precursors and the final product have to be carried out under dry, oxygen free, nitrogen or argon atmosphere. To avoid contact with water, all glassware was heated and evacuated while still hot prior to use.

The synthesis of **3a** involves the coupling of the two precursors as seen in **Scheme 3.4**. The first approach was to take the easy way by, directly after the preparation of **1a**, reacting it with **2** in a slurry hexane solution. This procedure was described by Bishop *et al* where dimethyliodoarsine was used for the synthesis of Ferrocene-1,1'-bis(dimethylarsine) [51].

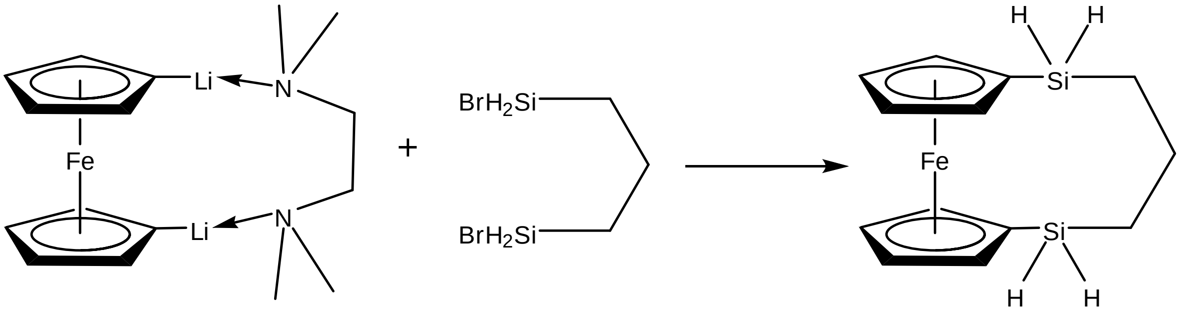

1a **2** **3a**

Scheme 3.4 Coupling of the two precursors resulting in the desired formation of **3a**.

According to the reactions described in the literature, compound **1a** is only partly soluble in hexane, giving suspensions but not clear solutions. Due to the obvious precipitation of the salt LiBr during the reaction, some kind of coupling of the two precursors had clearly taken place. The work up included the filtration of the salt from the solution, additional hexane and TMEDA condensed in a cooling trap with heating and reduced pressure and residual ferrocene sublimated.

^1H NMR spectrum (**Figure 3.2**) revealed that all $-SiH_2Br$ of reactant **2** had been used since the signal for these hydrogens at 4.49 ppm was not detected. It also revealed that a mixture of products had been formed. Additionally to the ferrocene peak at 4.16 ppm, at least six signals were detected in the aromatic region of the spectrum at 4.0-4.5 ppm. Shielding effects from the metal atom cause the chemical shifts of the aromatic signals to be shifted towards higher field ending up in the same region as the non-aromatic SiH_2 signal at 4.28 ppm. This signal can easily be characterized by three reasons; its position, its shape and the two satellite peaks located at 4.04 and 4.52 ppm (see Appendix L). No hydrogens are bonded to the ipso carbon atoms, making solely the coupling to the two hydrogens on the adjacent carbon of the bridging chain determine the peak's triplet shape. Above 4.50 ppm no signals are detected, neither in the spectrum in **Figure 3.2** nor in subsequent spectra in this section (except in **Figure 3.9**).

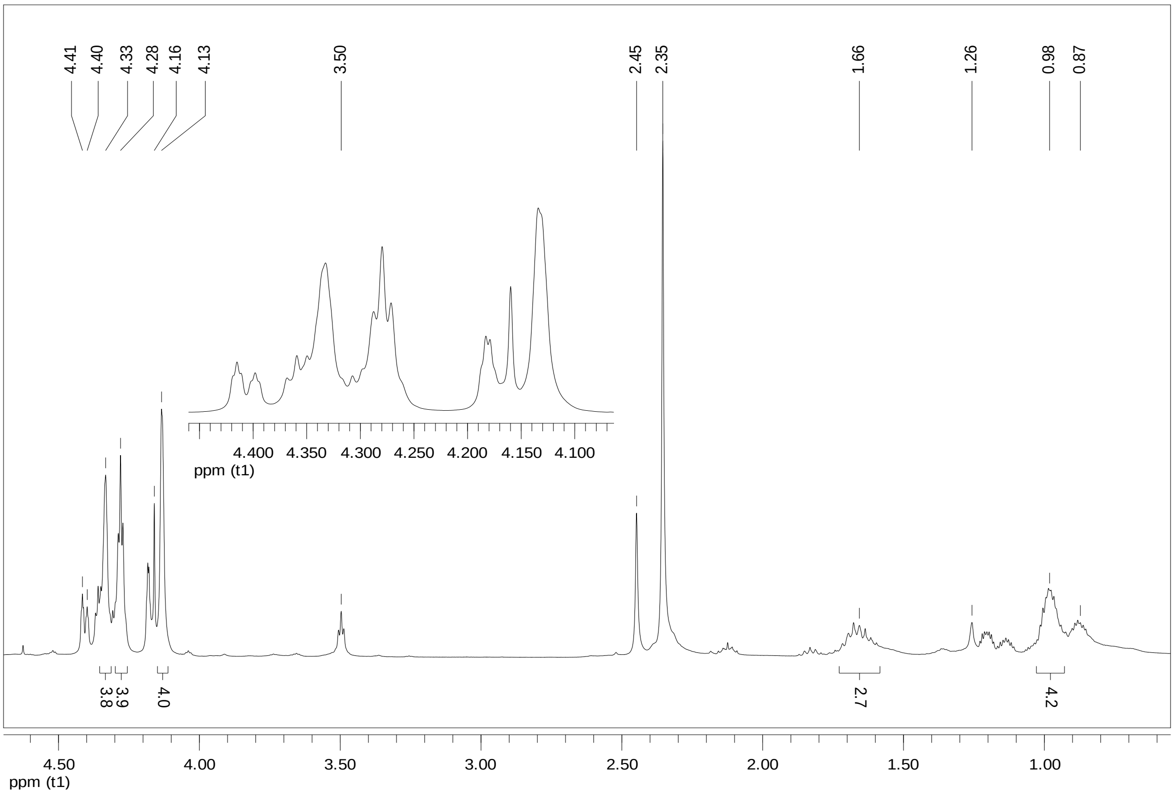

Figure 3.2 ^1H NMR spectrum from the first attempt at synthesis of 3a.

According to the symmetry of the desired product, it should account for two C-H signals from the Cp rings in the aromatic region. Therefore, it was reasonable to expect the number of two products in the mixture being some kind of substituted ferrocene. Also, SiH_3 triplet peak was detected in the NMR spectra at 3.50 ppm, giving rise to some impurities of monobrominated disilapropane. Additionally to the hexane multiplets at 0.88 ppm and 1.26 ppm, at least six signals were seen in the aliphatic region of the spectra. Likewise to the aromatic signal peaks, the propyl bridge of **3a** should give rise to two signals in the aliphatic region of the spectra. The fact that more than four signals are seen in this interval can be interpreted as four of them belong to the same two compounds as gave peaks in the aromatic region while the rest belongs to something else. Later, when the spectra are compared, the aromatic interval of interest is 4.08-4.45 ppm and the aliphatic interval is 0.60-2.25 ppm. No signals are found outside these intervals except the signals corresponding to TMEDA (at 2.35 and 2.45 ppm).

Eight times, a reaction was carried out trying to synthesize compound **3a**. From now on, these attempts are numbered reactions 1-8, whereof the detailed procedures of reactions 1, 4 and 8 are given in the experimental section. The first mixture from reaction 1 will be named 1-A and so forth. Some attempts were made to separate the products of reaction 1, and the results are given names accordingly (A-D) in **Table 3.2**:

Table 3.2 Treatment of products from reaction 1.

1-A	LiBr filtrated from the solution. Hexane and TMEDA condensed in a cooling trap. Ferrocene sublimated.
1-B	Product that sublimated at 170 °C and vacuum from 1-A.
1-C	Product that was not sublimated at 170 °C and vacuum from 1-A.
1-D	Product after filtering the mixture of 1-B and 1-C through 1.5 cm of silica gel.

1-B was sublimated from mixture 1-A at 170 °C and full vacuum, while 1-C was the portion remaining after the sublimation. Finally, the combined mixture of 1-B and 1-C was filtered through silica gel and washed down with hexane. The aromatic region of the ^{1}H NMR spectra of 1-A through 1-D is compared in **Figure 3.3**.

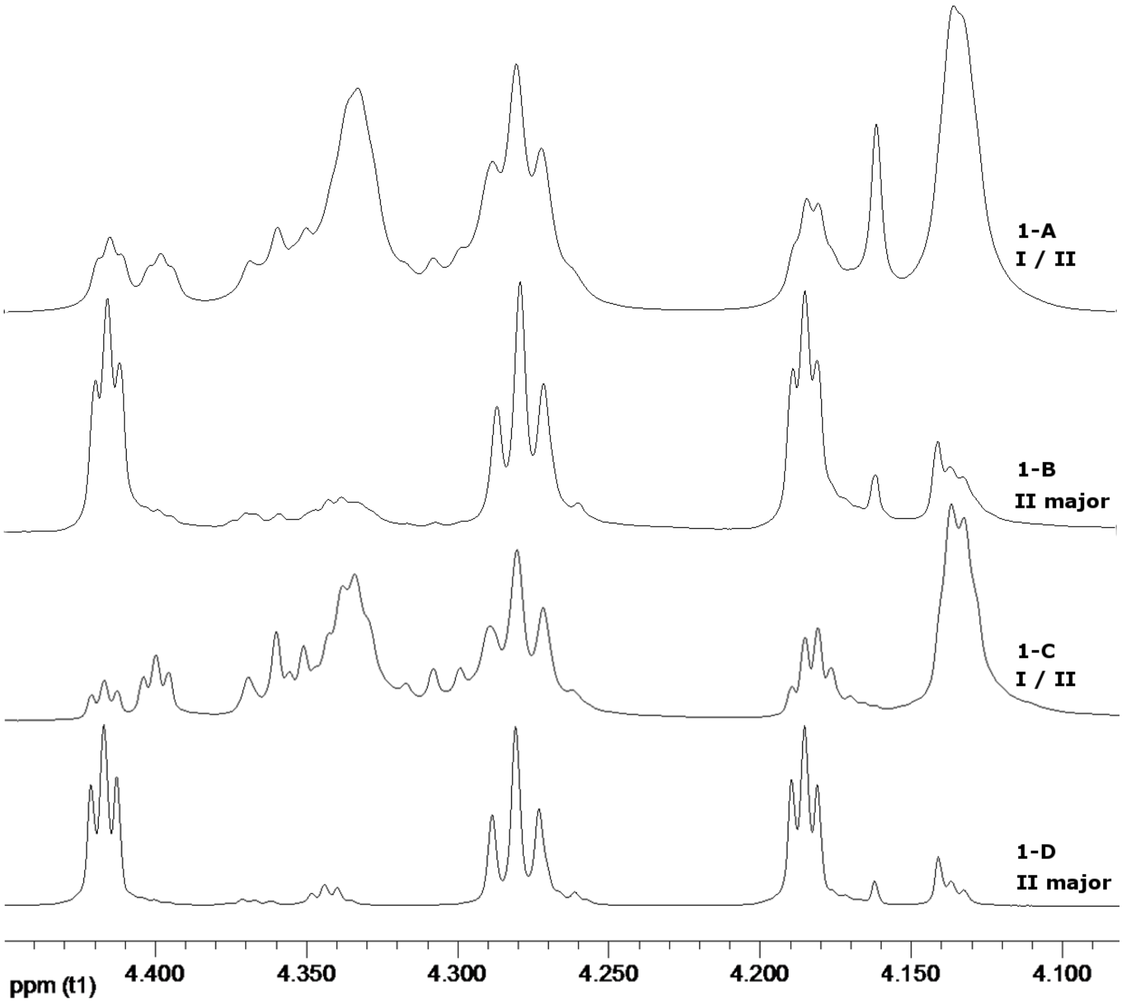

Figure 3.3 Comparison of ^{1}H NMR spectra of products from reaction 1, aromatic region.

Comparing 1-A with 1-B and 1-C shows that the sublimation process separated the products partly, leading to two sets of peaks. This is confirmed in the aliphatic region of the same spectra, **Figure 3.4**. Reactions 2-8 revealed the same two peak sets in their NMR spectra only in different amounts. So the same mixture of products was always formed but different methods yielded different combinations of products.

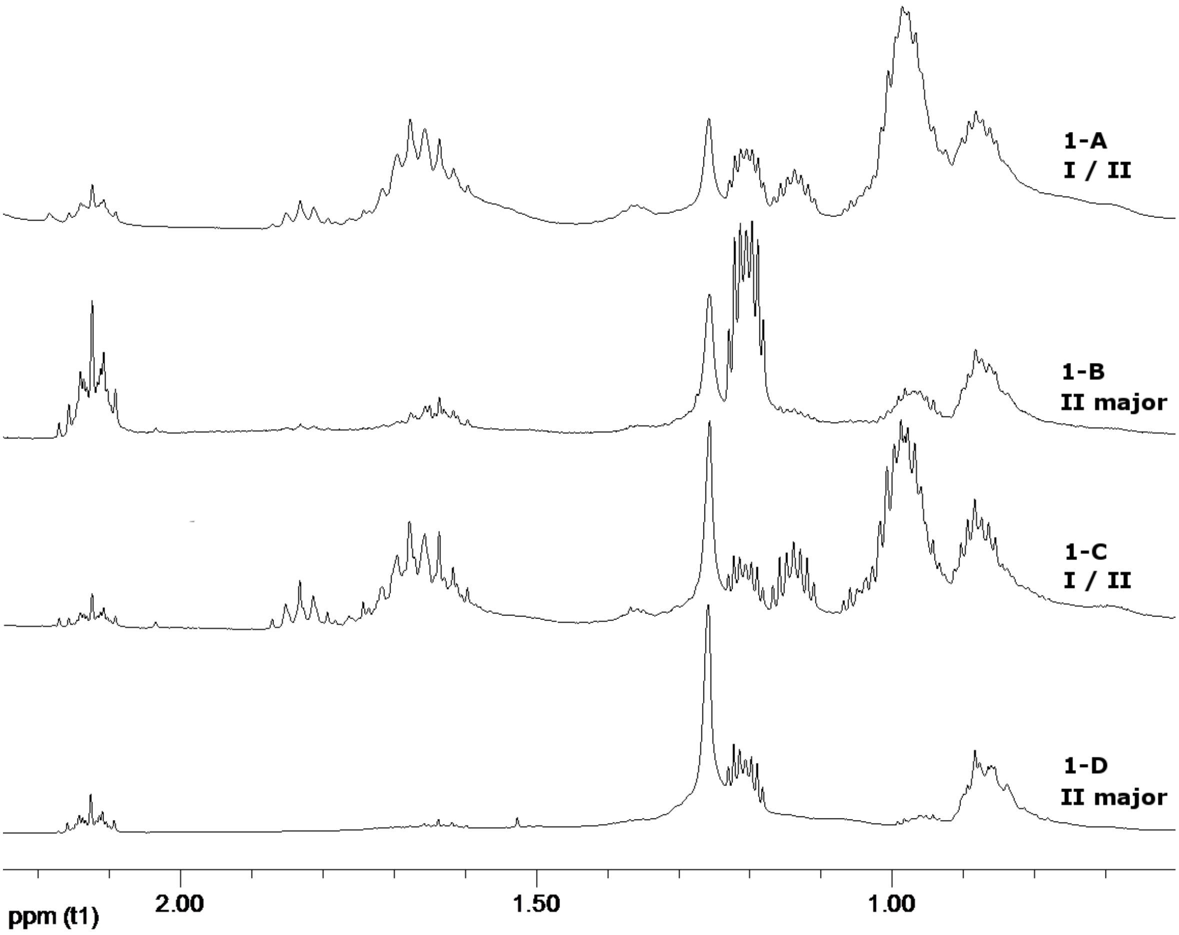

Figure 3.4 Comparison of ^{1}H NMR spectra of products from reaction 1, aliphatic region.

A further purification was obtained for 1-A by filtering the product through a thin layer of silica gel. Because of the reactivity of the product, the gel was dried by heating prior to use and stored under nitrogen atmosphere. Unsymmetrical products should be more polar and should therefore take longer time to pass through the silica gel. Therefore, the compound which passed through is believed to be the desired product **3a**. The method seemed to work fairly good so it was decided to run the product mixture through a 20 cm packed silica column. Since the cromatography had to be carried out under nitrogen atmosphere, a special column with a Schlenk unit was made for this purpose. Three fractions were collected from the column but their ^{1}H NMR spectra were not promising. Too long contact with the silica gel apparently had broken down the compounds.

Multiple reaction conditions and various purification methods resulted in different ^{1}H NMR spectra as mentioned above, so the signals could be interconnected and the three products given numbers, I, II and III. Hereafter, the peak set of 1-B is called II and the peak set of 1-C is called I. Peak set III only contains two signals in the aromatic region while peak set I contains four peaks in the aromatic region. A summary of the most obvious peaks of the three sets is given in **Table 3.3**.

Table 3.3 Chemical shifts of the ^{1}H NMR peak sets I, II and III.

Peak set I **δ in ppm**	**Peak set II** **δ in ppm**	**Peak set III** **δ in ppm**
0.99	1.21	1.15
1.70	2.13	1.83
4.14		
4.28	4.18	4.34
4.33	4.28	4.40
4.36	4.42	

In later attempts, the dry isolated adduct of **1a** was used. First, it was decided to follow a procedure described for the synthesis of 1,1'-Ferrocenediyldiphenylsilane, published by Staley, Wrighton *et al* [52]. The main difference of reactions 1 and 2, besides using the dry adduct in reaction 2, was that the reaction temperature was changed from -10 °C to 20 °C. ^{1}H NMR spectrum of the resulting mixture revealed even worse results compared to reaction 1. Clearly, the same product mixture had been formed but broad peaks in the spectrum can maybe be explained by paramagnetic properties possessed by some of the products. From this point, the reaction conditions were varied by for example using different solvents, changing the temperature and using different filtering methods, but a complete control of the reaction was unfortunately never accomplished.

Bishop *et al* claimed that **1a** is also readily soluble in 1,2-dimethoxyethane (glyme) [51]. This brought about the idea of using glyme as the reaction solvent as was done in reaction 3 and the reaction was carried out at room temperature. ^{1}H NMR spectrum from this reaction only showed peaks corresponding to ferrocene, TMEDA and glyme so the idea was abandoned without further attempts.

Reaction 4 was carried out at 20 °C using hexane solvent, just like reaction 2 but a fresh and more promising portion of the dry adduct **1a** was used. Not surprisingly, the ^{1}H NMR spectrum revealed the same broad peaks again but this time it was attempted to separate the products. **Figure 3.5** and **Figure 3.6** compare the aromatic and the aliphatic regions of the ^{1}H NMR spectra from reactions 2 and 4.

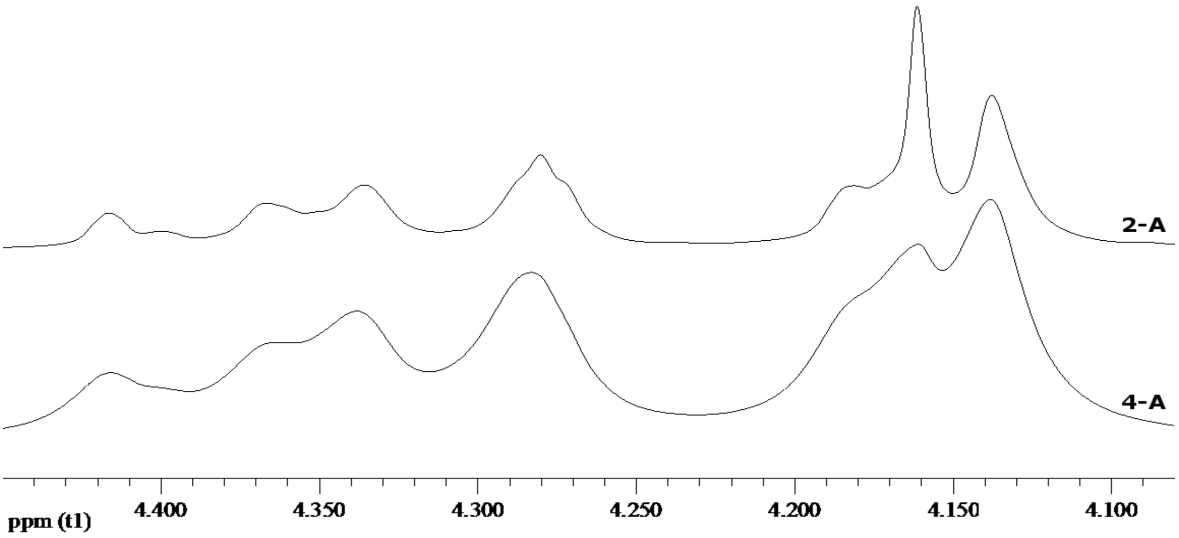

Figure 3.5 Comparison of the aromatic region of ^{1}H NMR spectra from reactions 2 and 4.

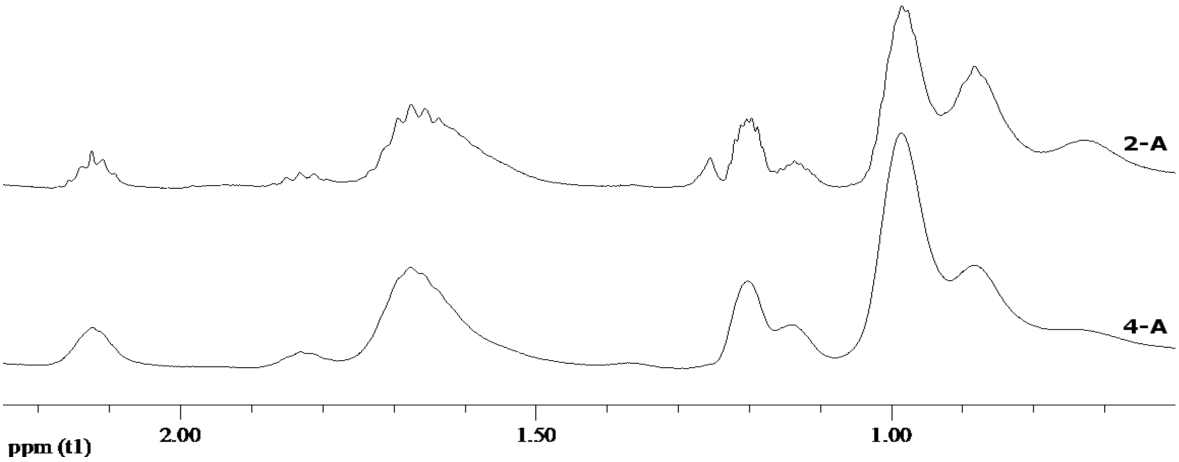

Figure 3.6 Comparison of the aliphatic region of ^{1}H NMR spectra from reactions 2 and 4.

After mixture 4-A had been dried under vacuum, it was planned to dissolve it again in hexane but the solubility had decreased considerably and it was only able to dissolve a fraction of the substance. It was decided to find out what compound would be the first to precipitate from the saturated hexane solution. Condensing off half of the hexane caused a precipitate to form. It is called 4-B while the remaining solvated compound is called 4-C. As seen in the ^{1}H NMR comparison in **Figure 3.7** and **Figure 3.8** the peaks are not as broad after this treatment. Also there is a detectable difference between 4-B and 4-C. There is more of peak set II in 4-C so the compound having this peak set has a greater solubility in hexane. Ferrocene also stays in the solution as seen from its peak at 4.160 ppm.

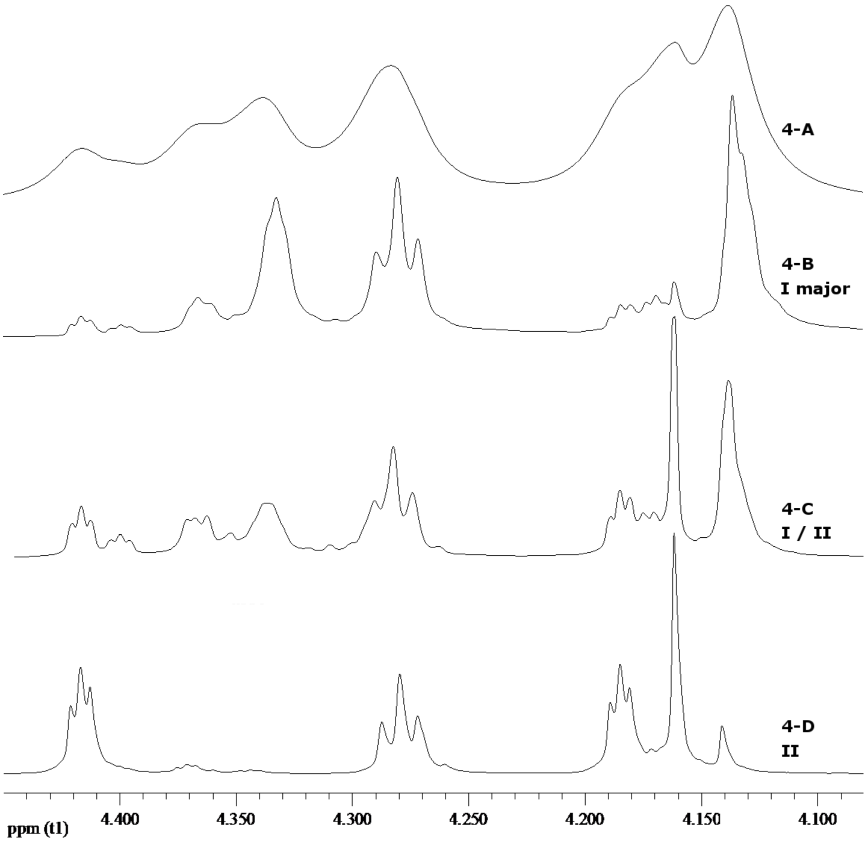

Figure 3.7 Comparison of the aromatic region in ^{1}H NMR spectra of products from reaction 4.

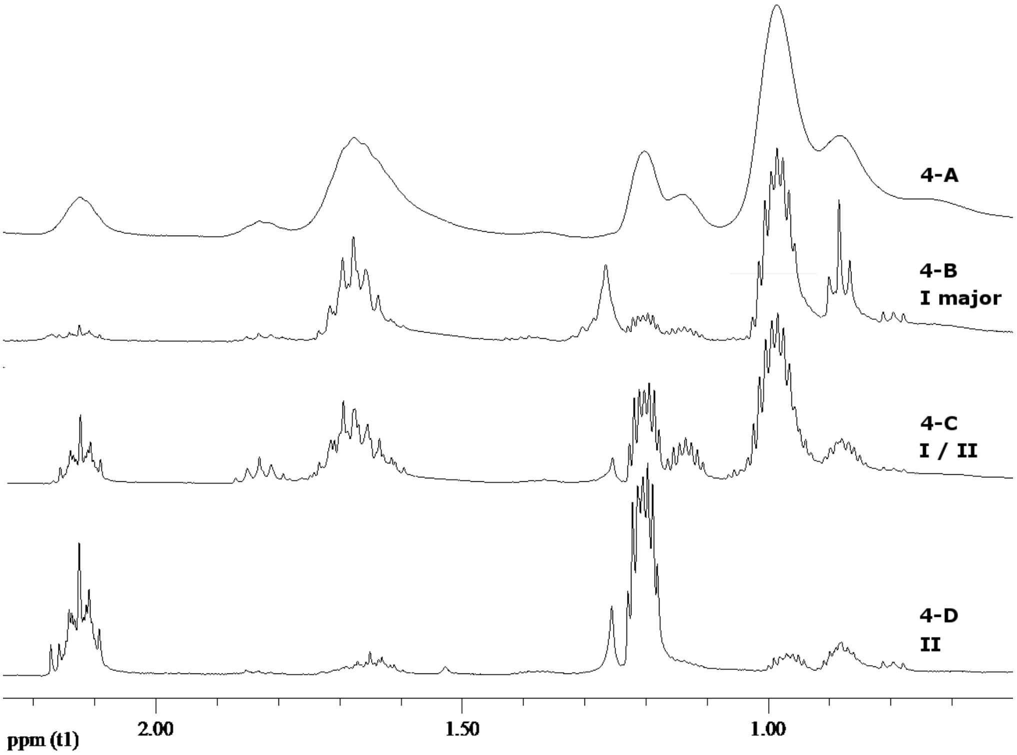

Figure 3.8 Comparison of the aliphatic region in ^{1}H NMR spectra of products from reaction 4.

This means that 4-B must contain a cleaner product of peak set I but 4-C a mixture of peak sets I, II and III. Filtering mixture 4-C through silica gel revealed that the the compound representing peak set II was the first to pass through the gel and should therefore be the less polar compound. This fraction is called 4-D. Compound I is believed to be more polar since it adheres to the silica gel. The chromatography had to be carried out very quickly as it had failed when trying to separate the product mixture of reaction 1. This time, only 1.5 cm of silica gel was used and it was only possible to collect the first fraction. All treatment of the product mixture from reaction 4 is summarized in **Table 3.4**.

Table 3.4 Treatment of products from reaction 4.

	LiBr filtrated from the solution.
4-A	Hexane and TMEDA condensed in a cooling trap.
	Ferrocene sublimated.
	4-A was partly solved in hexane;
4-B	First precipitation from hexane.
4-C	What stayed solvated.
	4-C was filtered through silica gel.
4-D	What passed first through 1.5 cm silica gel.

Despite substance 4-D was dried in vacuum for 4 hours, the resulting product contained fairly much hexane as seen in its NMR spectrum. Therefore, it is believed that hexane crystallized with the product giving peak set II.

From previous reactions, condensing the hexane solvent off the mixture and then dissolving again proved to be a bad way of handling these compounds. In reaction 5 it was decided to keep the hexane solvent on throughout most of the process. The reaction was carried out at -20 °C, the mixture filtered through celite and attempts made to separate the products by running it through 1.5 cm of silica gel and all this was done in the same hexane suspension. Two fractions were collected from the chromatographic packed silica gel column; the first fraction, 5-A, and the second fraction, 5-B. The first fraction showed peaks in the ^{1}H NMR spectrum that had never been observed before during this work.

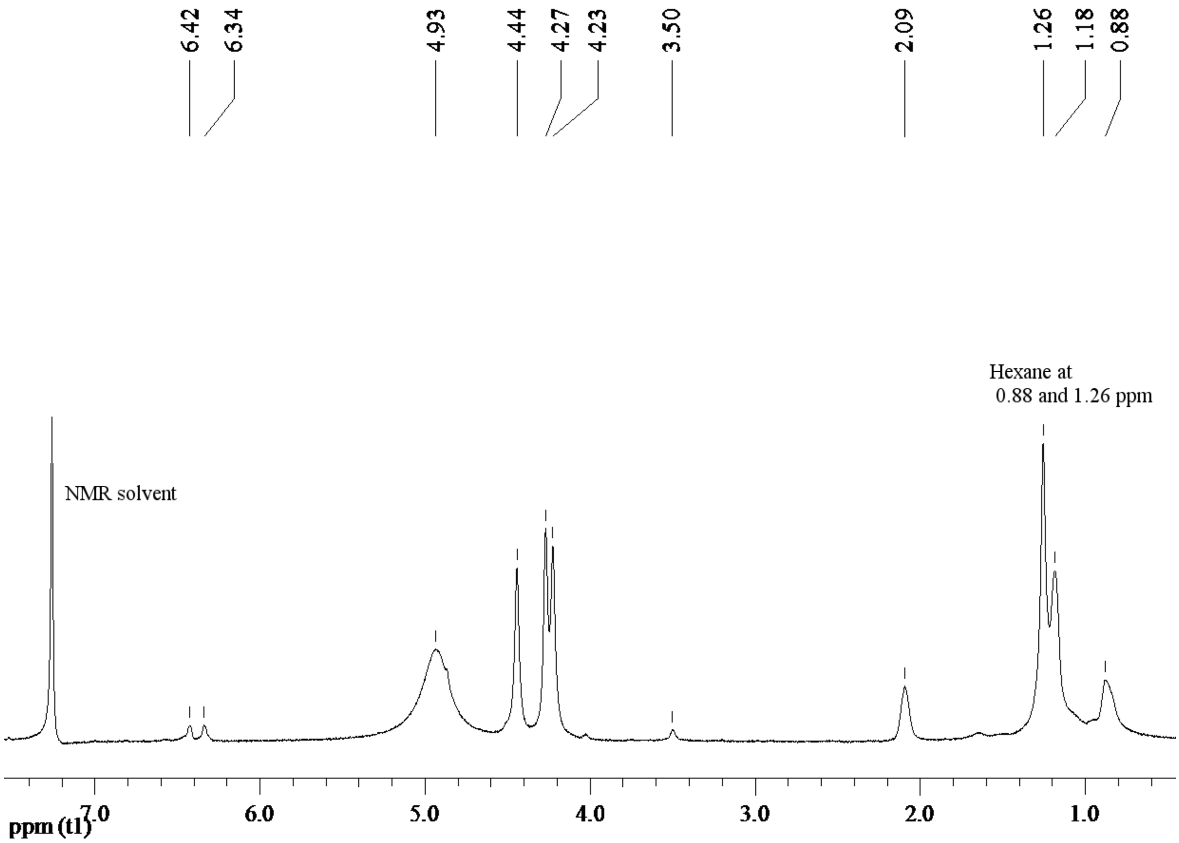

Figure 3.9 ^{1}H NMR spectrum of product 5-A.

It was decided to take ^{13}C NMR, COSY and DEPT 135 as well and all these spectra are displayed in the appendix. While working on the synthesis, these results were not believed to be successful and were not worked further with. At the time, all focus was on separating and isolating the products who had already been detected in preceding reactions. It was too late, not until during the writing of this thesis, when these spectra were compared to the calculated ^{1}H and ^{13}C NMR chemical shifts, showing that this fraction was indeed very promising, in terms of the calculated results. This comparison will be discussed later in section 3.3.

The second fraction, 5-B, was run through the silica with diethyl ether. Peak set II was not detected in its ^{1}H NMR spectrum but a mixture of peak sets I and III. This fraction was kept dry for three months and by that time, crystals were seen in the bottle. The contents were treated so as to make new crystals grow from saturated hexane solution but seven months of waiting only resulted in oily droplets.

By searching through the literature, the synthesis of a similar compound, diphenylsilane[1]ferrocenophane $Fe(\eta^5\text{-}C_5H_3{}^tBu)_2SiPh_2$ was found. This reaction was carried out at -78 °C using diethyl ether as a solvent [55]. In reaction 6, this procedure was followed, using the same reaction solvent and temperature. In the work-up, the solvent was condensed off and hexane added for filtering and recrystallization. Rough summary of the treatment of products from reaction 6 are given in **Table 3.5**. This includes two step recrystallization from hexane followed by sublimation of the latter precipitate.

Table 3.5 Treatment of products from reaction 6.

6-A	Filtration through celite. First recrystallization from hexane.
6-B	Second recrystallization from hexane.
6-C	Sublimated from 6-B.

First recrystallization from hexane, 6-A, gave ^{1}H NMR spectrum showing fairly clean peak set I so another recrystallization was carried out in an attempt to obtain even cleaner product, 6-B. The difference between the spectra of 6-A and 6-B was not much but still detectable. It was not surprising to find only mixture of peak sets I and III in these spectra, when thinking back to reaction 5. There, the mixture was treated with diethyl ether while reaction 6 was carried out using diethyl ether as a solvent. In both of these reactions, compound II was not observed in the ^{1}H NMR spectra but only mixtures of I and III. Therefore it was of great surprise to see peak set II suddenly appearing in ^{1}H NMR spectrum of 6-C, which is the small amount of substance sublimated from 6-B. The aromatic and aliphatic regions of the spectra from 6-A to 6-C are compared in **Figure 3.10** and **Figure 3.11**, respectively.

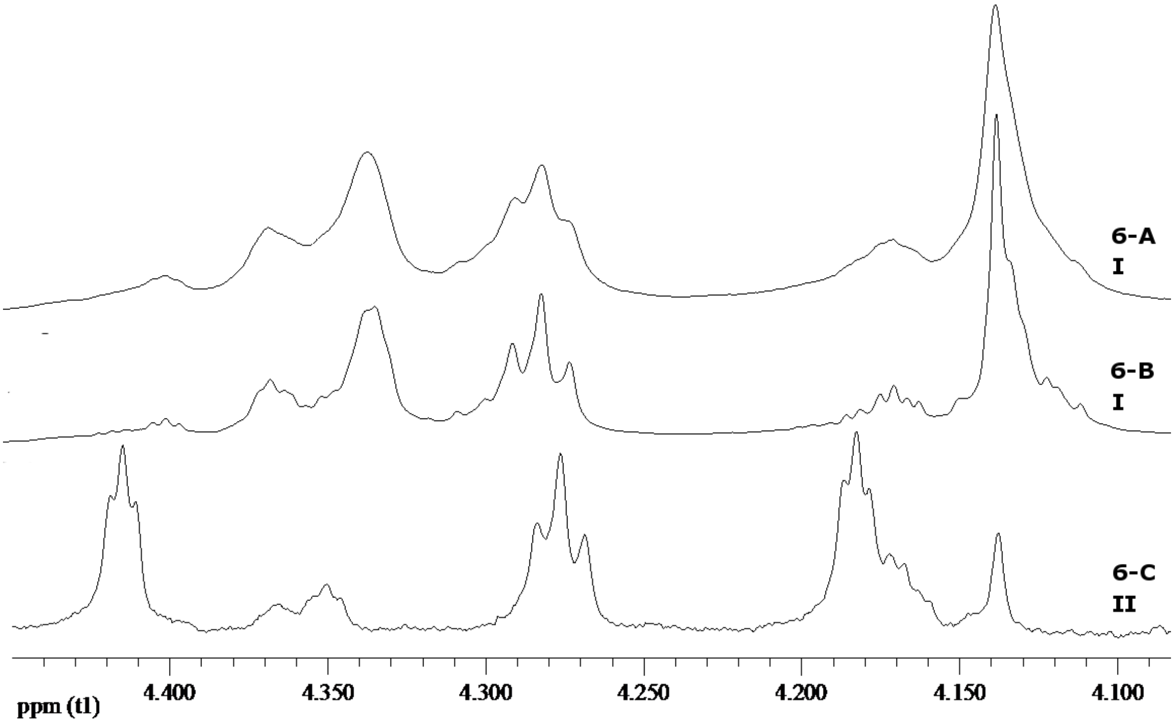

Figure 3.10 Comparison of the aromatic region in ^{1}H NMR spectra of products from reaction 6.

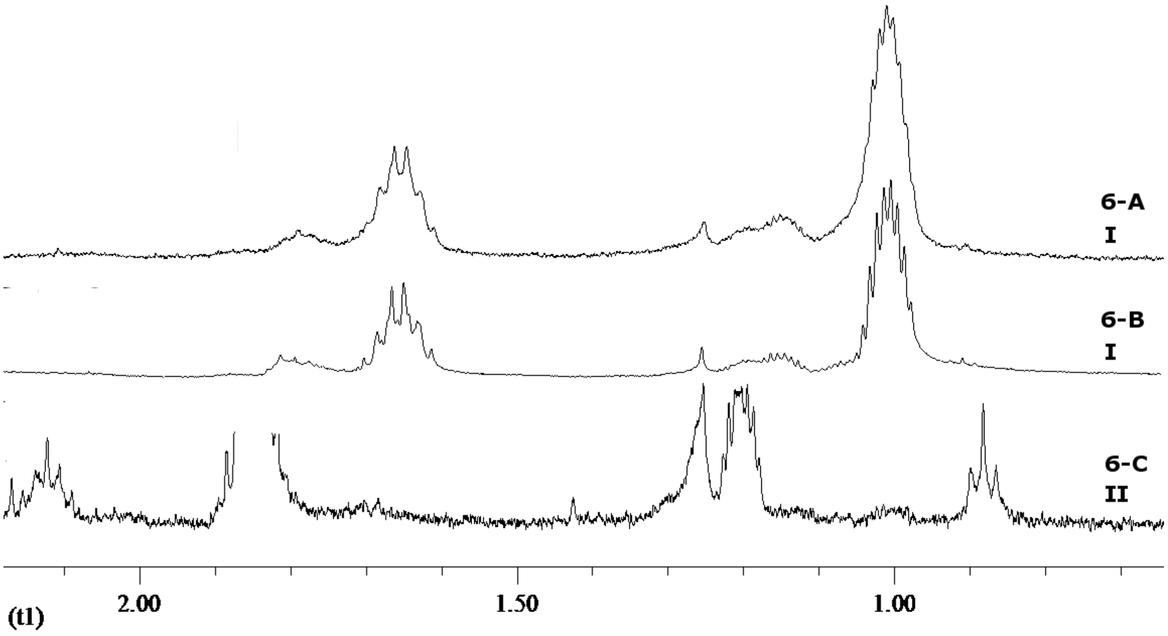

Figure 3.11 Comparison of the aliphatic region in ^{1}H NMR spectra of products from reaction 4.

Compound II had clearly formed during heating. The large multiplet at 1.85 ppm in the 6-C spectra is from THF impurities as it was being used in the lab at the same time. The peak was simply erased from the spectrum in the figure. Another fact worth to mention is the shifting of the peak at 4.28 ppm, which confirms that it is contained in both peak sets I and II. All attempts to crystallize 6-B were unsuccessful only resulting in oily droplets.

Reaction 7 was also carried out in ether solution. Like before, it resulted in a mixture of all three peak sets and attempts to separate the products were not successful. Nothing new was learned from this work.

At this point a very promising method was found in the literature [56-60]. Size exclusion chromatography (SEC) is a gel filtration where Bio-Beads® S-X [61] are used in a packed column to separate compounds by their size. Small compounds permeate the pores of the Bio-Beads and thus take longer to pass through the column. Therefore, the method is also called gel permeation. This makes the larger compounds pass through the column unhindered whereas small compounds are retained in the column. In this work, the desired product is the coupled compound **3a**. It is larger than the unwanted impurities which contain mostly ferrocene and TMEDA. The beads must be used with relatively nonpolar, aromatic solvents such as benzene, toluene or xylene which must be degassed prior to use. The same solvent should be used throughout the process which includes serving as a solvent, swelling the beads and being the mobile phase for the separation.

Since hexane was not one of the the recommended solvents for this purpose, it was decided to use toluene both as the reaction solvent as well as for the Bio-Beads chromatography. Toluene was chosen because of its low freezing point of -95 °C as opposed to the much higher freezing point of benzene 5.5 °C and xylene, having the lowest freezing point of -48 °C for the meta isomer up to 13 °C for the para isomer. This made it possible to carry out the reaction at low temperature in ethyl acetate cooling bath at -78 °C.

The concentrated reaction mixture was separated with gravity flow on a 20 cm Bio-Beads column and three fractions were collected. The middle fraction was a 2 cm broad coloured band on the column and the first and last fraction were what came before and after the coloured band. NMR spectra were taken for all fractions as well as of the reaction mixture. The fractions are listed in **Table 3.6** and comparison of the aromatic and the aliphatic regions of the NMR spectra are seen in **Figure 3.12** and **Figure 3.13**, respectively.

Table 3.6 Treatment of products from reaction 8.

8-A	Reaction mixture after filtration.
8-B	First fraction from Bio-Beads column.
8-C	Middle fraction from Bio-Beads column.
8-D	Last fraction from Bio-Beads column.

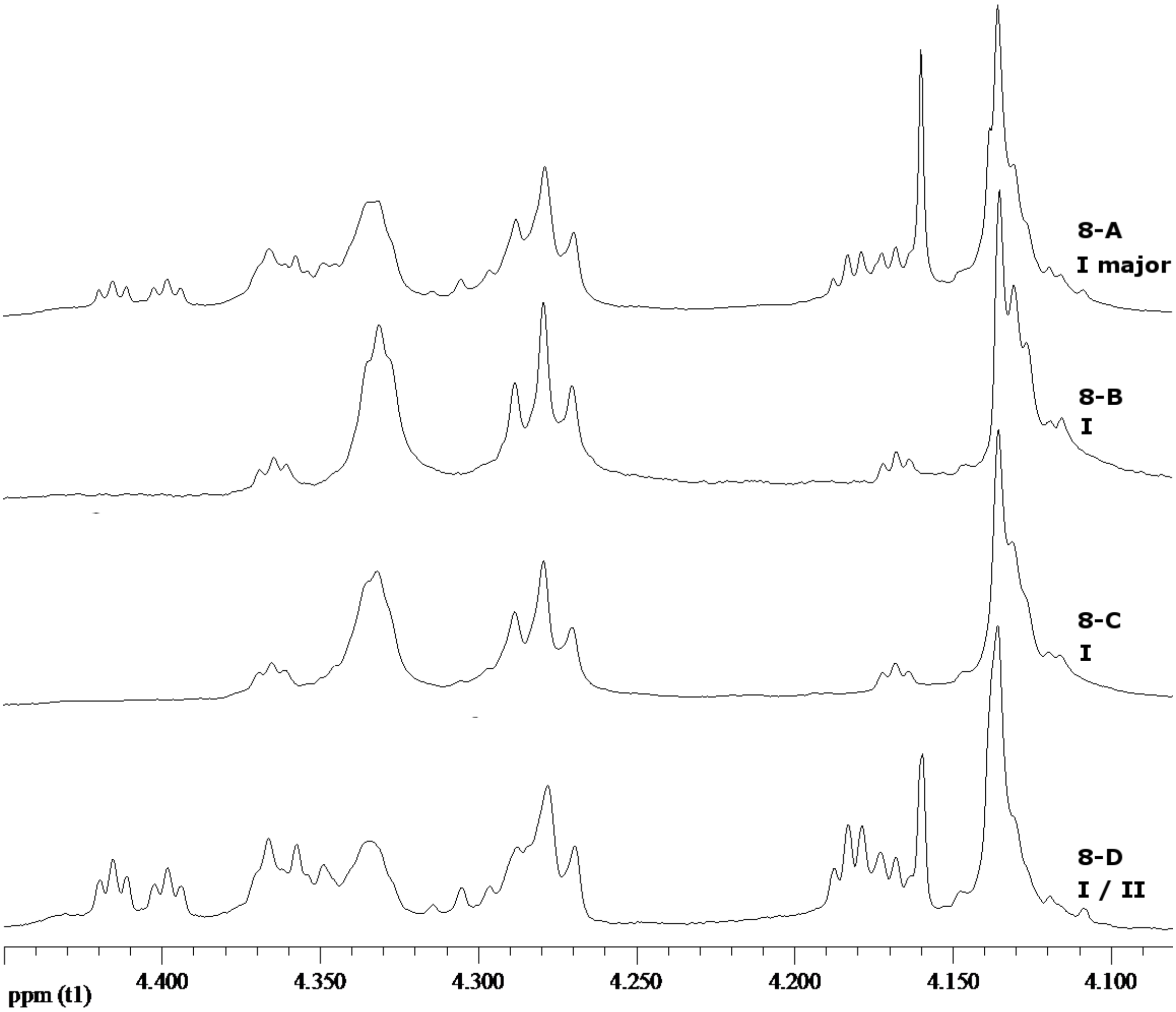

Figure 3.12 Comparison of the aromatic region in ^{1}H NMR spectra of products from reaction 8.

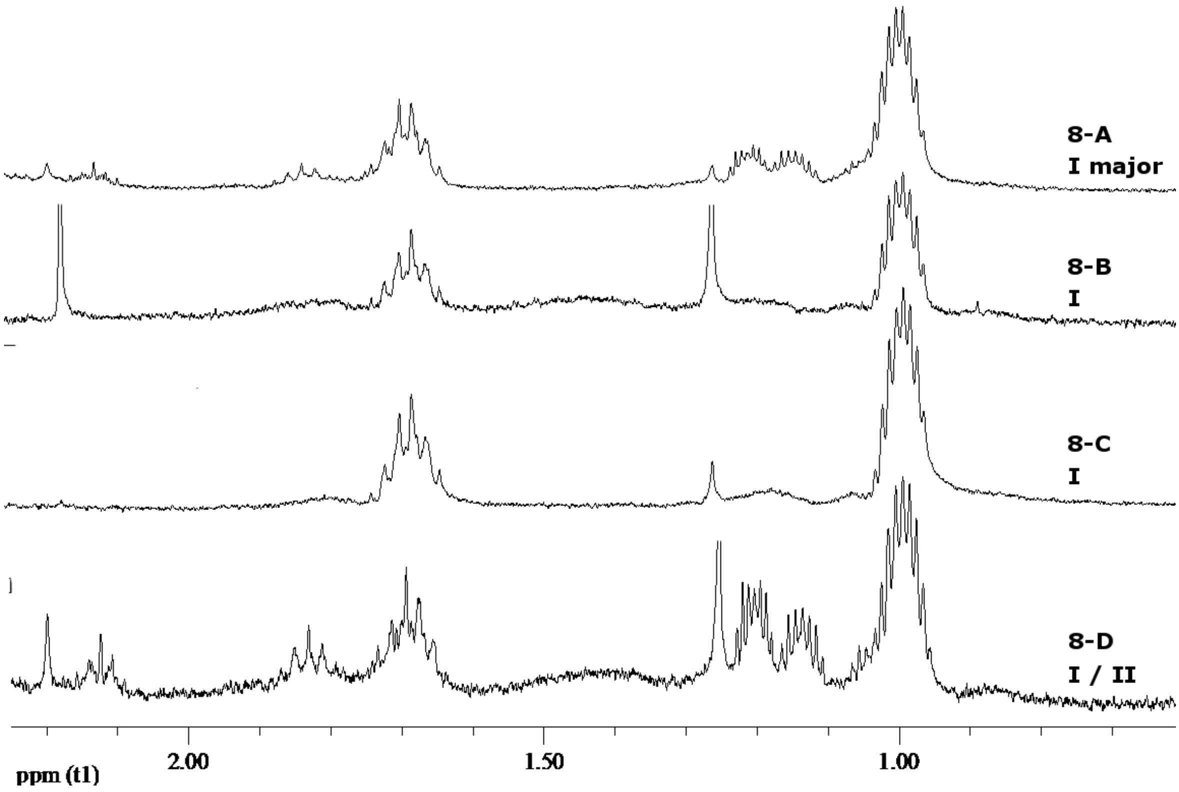

Figure 3.13 Comparison of the aliphatic region in ^{1}H NMR spectra of products from reaction 8.

The NMR spectrum of the reaction mixture, 8-A, contains peak set I and III, ferrocene and some other unknown peaks. Separation had clearly taken place on the column. The spectrum of the last fraction, 8-D, contains peak set III as well as the ferrocene peak at 4.160 ppm and some unknown peaks. The main fraction which included the coloured band seems to account only for peak set I.

Only a small portion of the reaction mixture was put on the column and it was done two times. Owing to the high price of the Bio-Beads it is essential to reuse the column but it is not easy since the smaller molecules adhere to the beads and cause contamination in later rounds. Therefore, the Bio-beads needs to be flushed with a great amount of solvent, which is very time consuming. The two middle fractions were combined and prepared so as to grow crystals.

At this point of the research, a whole year after the project started, the time schedule frame for the synthesis was completely broken. The main focus had shifted to synthesizing only compound **3a**, crystallize it and analyze. Great expectations were put on the growing crystals from fraction 8-C as its spectra seem to reveal the isolated product of compound corresponding to peak set I. It was therefore extremely frustrating to find the flask broken in the refrigerator one month later.

By that time, the computational project described in the first half of this thesis had started. It was believed to take only few months but turned out to be much more time consuming, taking a whole year in process.

3.2.1 Takeaway from the synthesis

Attempts at synthesis and purification of the ansa compounds took place in a period of a whole year and a total of eight reactions were carried out. **Table 3.7** summarizes the reaction conditions for all the eight experiments. They were all ran under different conditions except reactions 6 and 7.

Table 3.7 Summary of reaction conditions for the attempted synthesis of **3a**.

Reaction	Solvent	Phase of **1a**	T [°C]
1	hexane	slurry	-10
2	hexane	dry	20
3	glyme	dry	20
4	hexane	dry	20
5	hexane	dry	-40
6	Et_2O	dry	-78
7	Et_2O	dry	-78
8	toluene	dry	-78

Various methods were applied when trying to separate and isolate the products. During the process and later when the results were reviewed when writing this thesis, some features were discovered about the behavior of the products. Often the products from reactions 1-8 did not crystallize so easily but had oily appearance. Chemical changes caused by treatment with hexane are something really worth to mention. When hexane had been condensed off the reaction mixture and the solvent was added again, the solubility always decreased considerably. Only a small amount could be dissolved again. It was noted that ferrocene is more soluble in hexane than the compounds corresponding to peak sets I, II and III. Compound II forms during heating and when it is dried in vacuum, hexane peaks are always detected in its NMR spectra even though the product is completely dry. This may mean that hexane molecules are captured in the crystal structure of compound II.

In those instances when separation of products on a packed silica gel column was successful, the product corresponding to peak set II in NMR went faster through the gel, therefore being the less polar product. In the work-up of reaction 5, a very interesting behavior of the products was observed. The reaction mixture, which clearly consisted only of compounds I and III was run through a packed silica gel column and the resulting product was a fairly pure compound II. A definite explanation of this behavior is not known. However, it is clear that compound II must have formed during the treatment or while the mixture was running through the column. Another possibility is that compounds I and III react to form compound II.

In those instances when the reaction was carried out in hexane and diethyl ether, precipitation still occurred after the reaction mixture had been filtered. When reacted in toluene, the solution remained clear after filtration.

And finally, all attempts at crystallizing compound I resulted in oily droplets.

3.2.2 Conclusions of ansa compounds

The reason for the oily texture of the products is not believed to be merely due to the purity of the products but rather their properties. Besides the oily appearance, dramatically decreased solubility during treatment implies that polymers evolve in the product mixture. Considering the two precursors, polymer formation is very likely to have taken place. A polymer structure is illustrated in **Figure 3.14**.

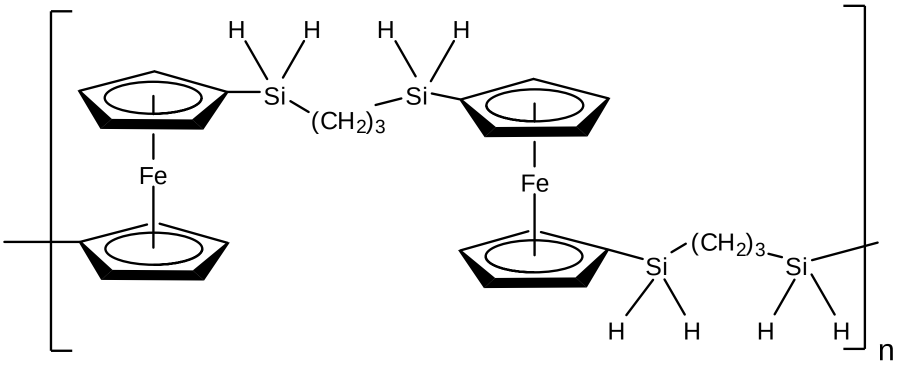

Figure 3.14 A possible product is the polymer.

Another possible structure is the dimer, made up by two ferrocene units interconnected by two disilapropane chains, seen in **Figure 3.15**. Compared to its monomer, this compound should have the same or very similar chemical shifts in NMR spectra and the same fractional integration in ^{1}H NMR spectra. The only presumed difference being their different chemical behavior and molecular masses.

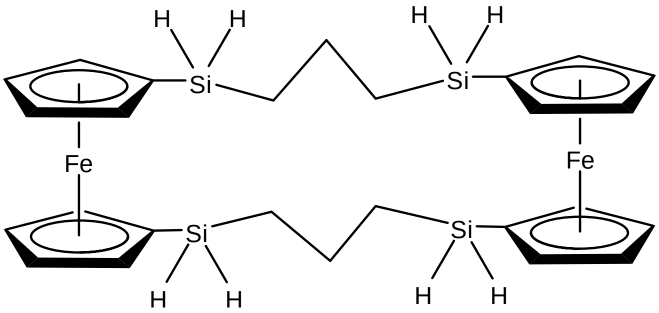

Figure 3.15 One of the possible products is the dimer.

Besides the dimers and polymers, several other byproducts were possibly formed. Unsubstituted ferrocene gives a singlet at 4.16 ppm but if the ferrocene is monosubstituted, the unsubstituted Cp ring still gives the same or very similar signal at 4.16 ppm. Ferrocene is easily removed from the reaction mixture so the presence of monosubstituted ferrocenes explains why its signal is sometimes still seen after its removal. Actually, the formation of byproducts usually affects the NMR spectra by increasing the number of signals. As seen in ^{1}H NMR spectra in **Figure 3.2** and **Figure 3.9**, from reaction 1 and 5, respectively, a triplet corresponding to terminal -SiH_3 is seen at 3.50 ppm. This peak arise when only one of the two Si atom of the chain is bonded and is seen in all spectra from reactions 1, 2, 4 and 5 but is not detected at all in spectra from reactions 6 and 8. The appearance of this peak seems to follow no pattern.

3.3 Calculated NMR shifts of 3a

Due to the puzzling NMR spectra of compound **3a**, it was decided to calculate the expected NMR chemical shifts with computational methods. The calculations were performed by Ragnar Björnsson, using the GIAO method in Gaussian 09. The geometry optimization was based on the BP86 functional using the def2-TZVP basis set. NMR calculations were done using PBE1PBE/6-311+G(2d,p) and also PBE1PBE/aug-pcS-2 with the def2-TZVPP basis set used on the Fe. TMS was calculated at the same level of theory as a reference for ^{1}H, ^{13}C and ^{29}Si. The chemical shift was obtained by subtracting the compounds isotropic shielding from the reference isotropic shift. Average values were used for the chemically identical atoms in the compound. The computed results are summarized in the first column of **Table 3.8**-**Table 3.10**. The ^{1}H and ^{13}C NMR chemical shifts are compared to peak sets I and II as well as the most promising peak set from one of the fractions of reaction 5, namely 5-A. There are no experimental ^{29}Si NMR results available but the calculated chemical shift is nevertheless shown in **Table 3.10**.

Since the true molecular structures corresponding to peak sets I, II and 5-A have not been determined, their chemical shift values do not necessarily correspond to the carbon/hydrogen positions listed in the first column of each table.

Table 3.8 Calculated ^{1}H NMR chemical shifts for compund **3a**. Comparison to observed peak sets I, II and 5-A. Values in ppm.

	calc.	set I	set II	5-A
$C_iCHC\textit{H}$ (on Cp)	3.97	4.33	4.42	4.27
$C_iC\textit{H}$ (on Cp)	3.84	4.14	4.18	4.23
$Si\textit{H}_2$	4.88	4.28	4.28	4.93
$SiCH_2C\textit{H}_2$	2.16	1.70	2.13	2.09
$SiC\textit{H}_2$	1.16	0.99	1.21	1.18

Table 3.9 Calculated ^{13}C NMR chemical shifts for compound **3a**. Comparison to observed peak sets I, II and 5-A. Values in ppm.

	calc.	set I	set II	5-A
$C_iCH\textit{C}H$ (on Cp)	74.49	72.16	71.47	75.07
$C_i\textit{C}H$ (on Cp)	79.14	75.07	74.74	71.77
C_{ipso}	67.66	68.58	63.71	29.69
$SiCH_2\textit{C}H_2$	23.01	21.44	20.10	20.02
$Si\textit{C}H_2$	11.96	14.70	10.58	10.53

Table 3.10 Calculated ^{29}Si NMR chemical shift for compound **3a**.

	δ ppm
Si	344

When comparing the calculated chemical shifts and the chemical shifts of peak set II in **Table 3.8** it is obvious that either the calculations are not correct or the synthesized compound is simply something else. These results were very frustrating as peak set II was believed to correspond to the desired product.

3.4 Attempted synthesis of 3b

In 1968, thirteen years after the discovery of bis(benzene)chromium, it was lithinated for the first time by Elschenbroich [62]. Like for ferrocene, the metalation takes place with *n*-BuLi in presence of TMEDA but *n*-BuLi alone does not react [63]. While Elschenbroich was studying this method, Rausch *et al* reported the application of the TMEDA/*n*-BuLi reagent to the metalation of ferrocene, meaning that the discoveries were done simultaneously but independently of each other. Elschenbroich and Rausch's ideas still originated from the same background [64, 65].

The metalation reaction of bis(benzene)chromium is carried out at elevated temperature of 70 °C in cyclohexane, but the coupling to **2** (**Scheme 3.5**) was attempted both at room temperature and in a cooling bath at -78 °C.

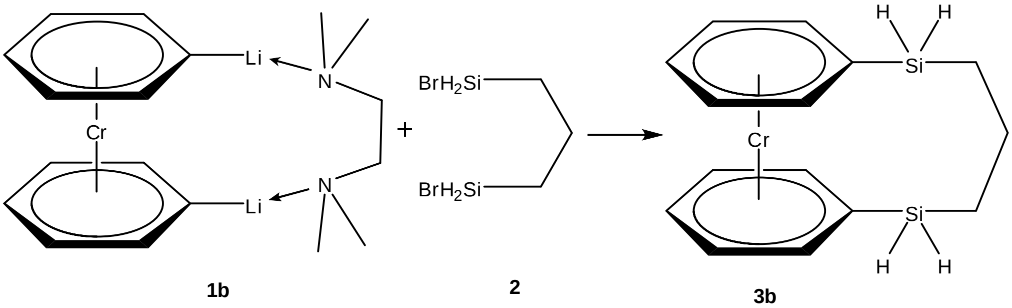

1b **2** **3b**

Scheme 3.5 Coupling of **1b** and **2** resulting in a [5]chromoarenophane.

Elschenbroich's synthetic route to diphenylsilane[1]chromoarenophane was followed except that he used petroleum ether as solvent in the coupling reaction. Since the lithiation is carried out at 70 °C, cyclohexane (having boiling point of 81 °C) is used as solvent. The coupling reaction was carried out directly after the lithiaton. In the first attempt, in a cyclohexane slurry of **1b** but in the second attempt the cyclohexane was decanted off after the lithiation and replaced by hexane, since hexane has the much lower freezing point of -95 °C as opposed to 6.5 °C for cyclohexane. Compounds **1b** and **3b** only dissolve partly in these solvents, so during filtration the salt was washed with hot toluene so as to dissolve further any desired products.

After two attempts at the coupling reaction followed by work-up, no plausible product had been isolated. ^{1}H NMR spectra were obtained from all stages of the work-up and only one spectra contained signals in the aromatic interval. It is not reasonable to point out which proton in the complex corresponds to which peak. Nevertheless, the spectrum (taken in $CDCl_3$) is shown in **Figure 3.16**. The peaks in question are the three peaks in the aromatic region having chemical shifts of 3.99 ppm, 4.09 ppm and 4.86 ppm and the two peaks in the aliphatic region at -0.05 ppm and 0.12 ppm, since they do not represent any of the other chemicals used in the reaction, namely toluene, TMEDA and hexane (cyclohexane is not detected in the spectrum).

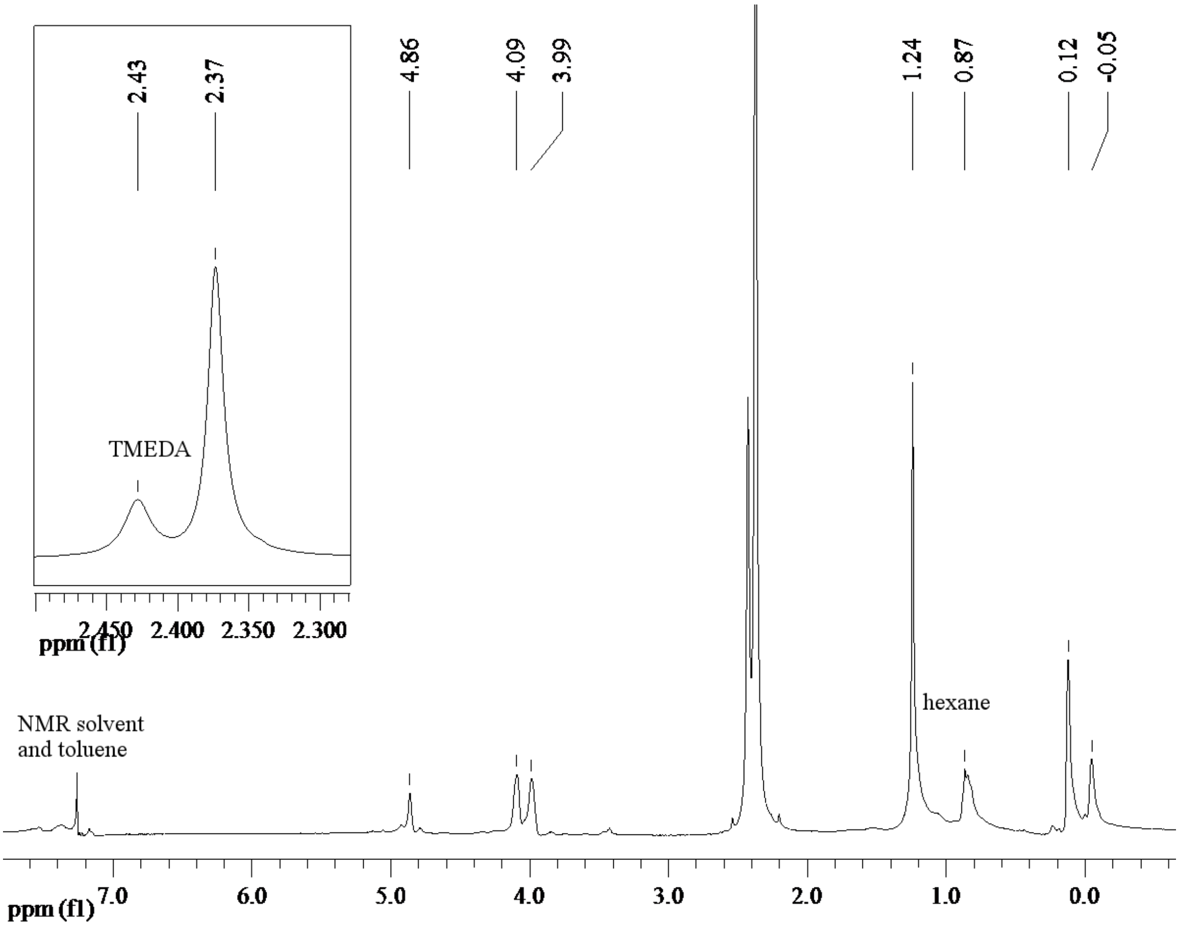

Figure 3.16 The most promising ^{1}H NMR spectrum from the attempted synthesis of **3b**.

It is worth pointing out that neither of the two precursors bis(benzene)chromium nor **2** is detected in the spectrum.

At this stage of the process it was decided to put the chromoarenophane work aside for a while and continue working on the isolation of the ferrocene-containing complex. The plan was to return back to the chromoarenophane after the ferrocenophane had been synthesized and isolated. But that was never done.

4 Other work

4.1 Nysted reaction

1,3-disilacyclohexane, **4**, is among the numerous silicon containing six-membered ring systems that have been prepared in Árnason's research group at the Science Institute. The known synthetic route to this compound is the reaction of **2** with a methylene di-Grignard as shown in **Scheme 4.1** [66].

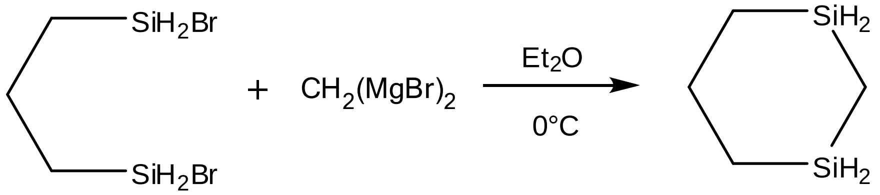

2 **4**

Scheme 4.1 The standard synthetic route to **4** is by reacting **2** with $CH_2(MgBr)_2$.

The drawback of this method is the poor yield of the final reaction of only 17% as well as the very time-consuming synthesis of the two precursors. **2** is synthesized in the three step reaction shown in section 3.1.2 and the preparation of the di-Grignard is extremely challenging and requires very specialized equipment.

Since **2** was available pure and in a generous quantity, it's utilization in other possible reactions was ideal. In the search for an improvement of the synthesis of **4**, the proposed reaction of **2** with the Nysted reagent [67] was carried out (**Scheme 4.2**)

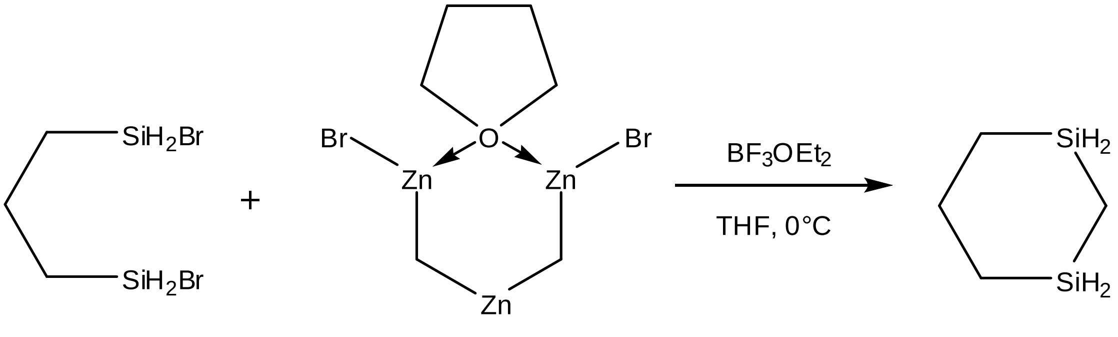

2 **Nysted** **4**

Scheme 4.2 The proposed formation of **4** in the one step reaction of **2** with the Nysted reagent.

Success in this reaction would be a significant simplification to the previously known synthetic route since the Nysted reagent is commercially available. Each molecule of the reagent possesses two *gem*-dimetallic subunits and is therefore assumed to have high potential for methylenation of carbonyl compounds and is indeed recognized for that functionality in the presence of the Lewis acid $BF_3{\cdot}OEt_2$ as described by Matsubara *et al*

[68]. This brought up the idea that the doubly Zn-bonded CH_2 goups could be able to attack both of the electrophilic Si atoms in **2**, resulting in the closed ring structure of **4**.

This side-project was not intended to be explored in detail, unless the outcome from the first reaction would be fairly promising. Matsubara's procedure used in the methylenation of dodecan-2-one was followed and the product investigated by ^{1}H NMR. Reported chemical shifts of **4** are at δ = -0.02, 0.70-0.83, 1.84-2.00 and 3.94 ppm so if the compound had been formed in the reaction, its peak were well hidden under peaks of impurities and unknown products in much greater amount, as clearly seen in **Figure 4.1**.

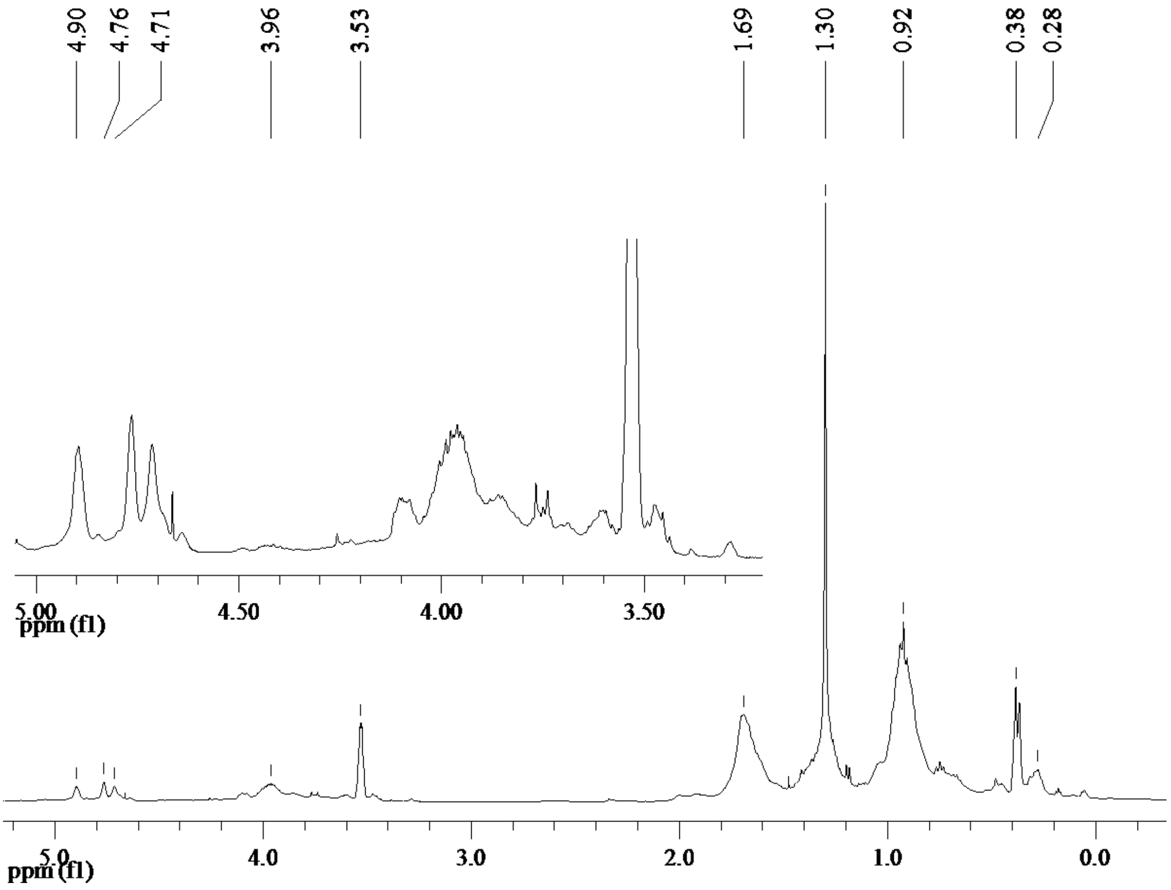

Figure 4.1 ^{1}H NMR spectrum from the only attempted synthesis of **4**.

4.2 Mass spectrometric studies of a titanasiloxane complex

In 2008, the eight-membered ring **6**, along with several side products, was surprisingly prepared in Árnason's research group at the Science Institute via the reaction illustrated in **Scheme 4.3** [69].

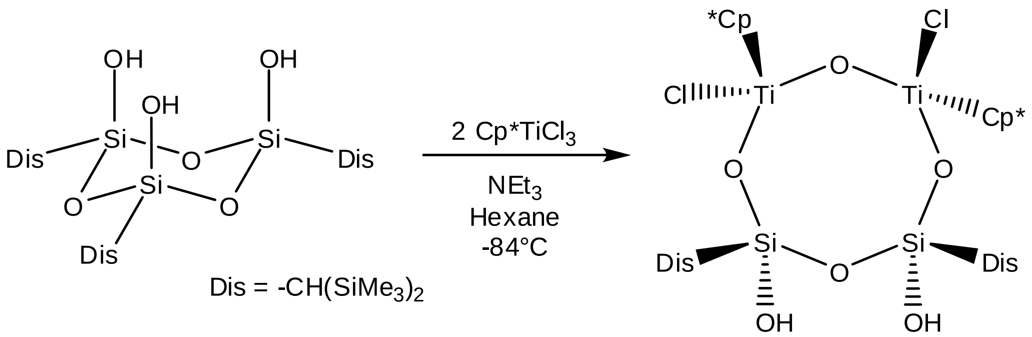
OH
OH
OH
Si
Si
Si
Dis
Dis
Dis
O
O
O
Dis = -CH(SiMe3)2
2 Cp*TiCl3
NEt3
Hexane
-84°C
*Cp
Cl
Cl
Ti
Ti
Cp*
O
O
O
O
Si
Si
Dis
Dis
OH
OH

5 **6**

Scheme 4.3 Formation of the eight-membered ring **6**.

The complex was isolated and characterized by ^{1}H, ^{13}C and ^{29}Si NMR spectroscopy, X-ray analysis and mass spectrometry in 2008. It later turned out that more precise mass spectrometry analysis was needed of the compound and it was a part of my B.Sc. project to prepare a new sample for that purpose [70]. In the timeframe of my Master studies, the mass spectrometry measurements were performed. A requirement to the mass spectrum was that it had to contain isotopic pattern which could explicitly verify the chemical formula of the complex, $C_{34}H_{70}O_6Ti_2Si_6Cl_2$.

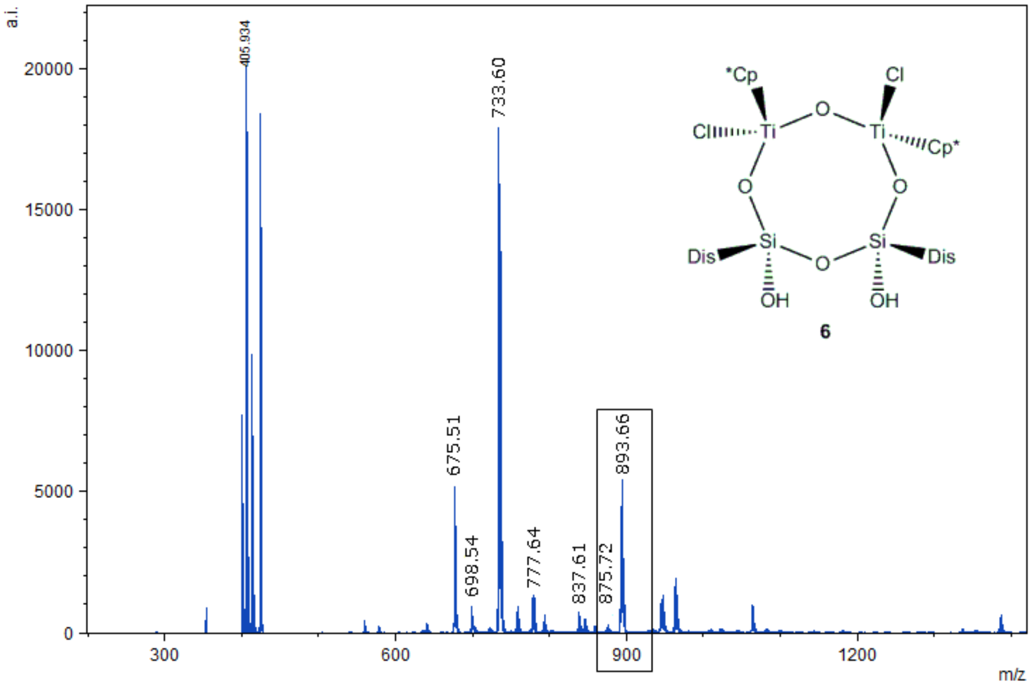

Figure 4.2 Mass spectrum of **6**. The marked peak was analyzed and simulated.

No mass peak was detected for the intact molecular ion and the peak that comes closest is the framed peak of spectrum in **Figure 4.2**. It corresponds to the ion after a H_2O-loss, having the mass of 893.66 amu. In order to obtain consistency between the masses in the spectra and of the molecular fragments, a great deal of speculation was needed. When a shift of +1.45 amu was realized between the real fragment masses and the mass values in the spectra, the experimental values fitted excellently to the calculated simulations. Out of the 12 mass peaks listed in **Table 4.1**, the isotopic pattern of four peaks was simulated and they are marked in the table. The values in the table are the shifted values, by +1.45 amu.

Table 4.1 Fragmentation of **6** observed in its mass spectrum.

Mass [amu]	Fragment lost	m/z [%]	Simulated
908.2		0	
893.660	H_2O	27	yes
875.720	2x H_2O	1	yes
858.656	H_2O and Cl	1	yes
846.872	?	2	
837.609	2x HCl	4	yes
793.522	?	3	
777.639	?	7	
758.532	H_2O and Cp*	5	
733.595	H_2O and $C(SiMe_3)_2$	90	
698.542	?	5	
675.511	?	26	

Simulations were performed in the Mnova Suite graphical software program, version 8.0.0. [71]. The calculated isotopic patterns are in very good agreement with the experimental mass spectrum. As an example, the simulation of the –H_2O peak at 893.66 is shown in **Figure 4.3**. The experimental spectrum is above and the simulated spectrum is below and has been flipped. Mnova calculates it when provided a chemical formula. It fits nicely to the experimental isotopic pattern. All the four simulation results, which are marked in **Table 4.1**, are given in appendix R.

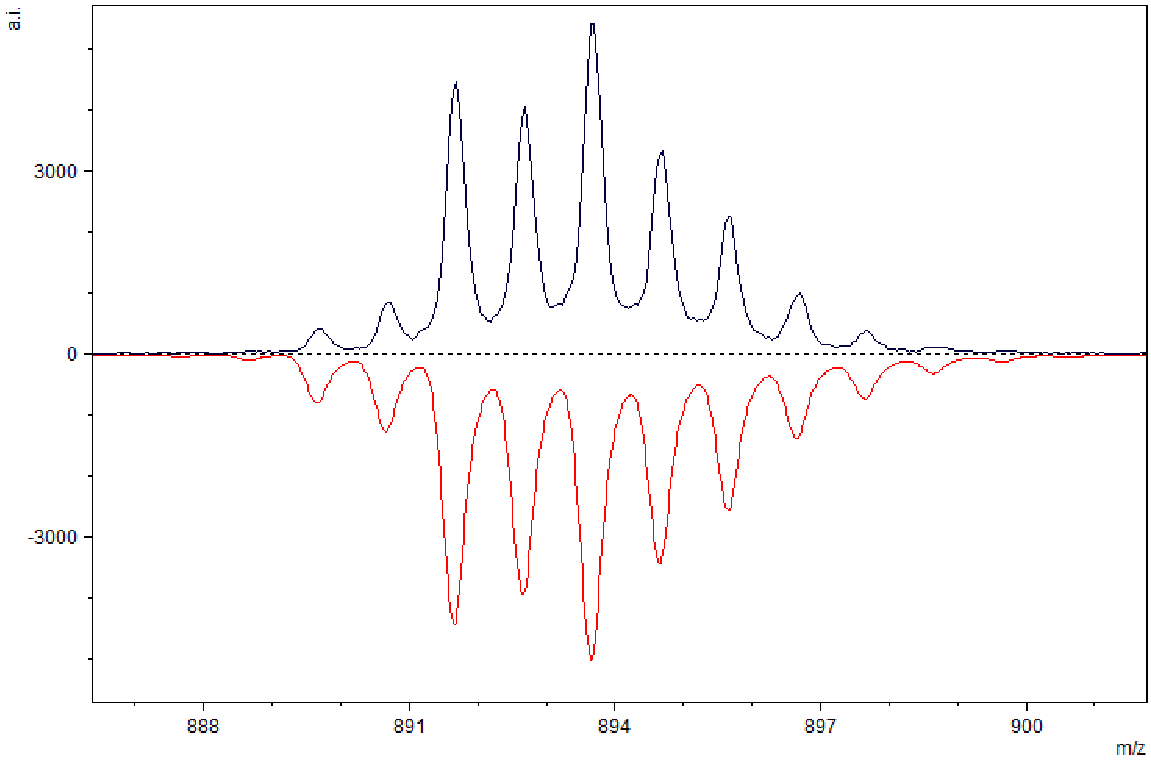

Figure 4.3 The peak of the mass spectrum of **6** corresponding to H_2O-loss. The experimental spectra is above and the simulated below.

5 Summary

In the first part of the thesis, the breakdown analysis of 1-monohalogenated 1-silacyclohexanes $(CH_2)_5SiHX$; X = F, Cl, Br, I were discussed in detail. Dissociation energies were calculated by computational methods for the most common breakdown pathways and the computational methods clearly explained. Possible breakdown pathways for the compounds were discussed, illustrated and compared to computational results and calculated breakdown diagrams were constructed for every derivative.

Experimental breakdown analysis was carried out by the Threshold Photoelectron Photoion coincidence (TPEPICO) technique. The experimental method was discussed as well as data processing to obtain the experimental breakdown diagrams.

Breakdown analysis show that all of the four derivatives, except the I-substituted silacyclohexane dissociate in a similar manner. The F-, Cl-, and Br-substituted derivatives commonly dissociate by losing an ethylene fragment at the lowest energy onset but a propene loss is also observed to some degree. On the other hand, the first dissociation step of the I-substituted silacyclohexane is the loss of the halogen atom, resulting in a somewhat different breakdown pathway. Calculated breakdown diagrams revealed that the cleavage of ethylene and propene requires very different molecular rearrangement in order to pass through the transition state of the cleavages. Ethylene or propene loss requires similar energy for all the rings while the Si-X bond energy decreases considerably when going from the lightest halogen derivative to the heaviest, the Si-X bond cleavage being the lowest energy initial dissociation step for the I-substituted ring. Generally, this was in good agreement with the experimental breakdown diagrams.

The second part of the project described the attempted synthesis of the ansa compounds [5]ferrocenophane and [5]chromoarenophane. The synthetic schemes looked very promising on the paper but in practice, the project is an evidence of the backbreaking battle chemists frequently wage in the laboratory. Initially, several derivatives of the ansa complexes were intended to be prepared and their properties meant to be studied by various experimental techniques, first and foremost by crystallographic analysis. Attempts at the synthesis were very time consuming and eventually, the target was only to synthesize and isolate compound **3a**.

A total of eight reactions were carried out by means of different reaction conditions and various methods applied trying to separate the product mixtures. NMR analysis showed that a reaction had clearly taken place and more than one product was formed. By examining the numerous spectra from the reactions, three peak sets corresponding to three different products were found. In lights of the NMR spectra, isolation of two of the products seemed to have been successful but they did not crystallize so crystallographic analysis was not an option. Only viscous oily droplets were obtained for one product while the flask containing the most promising portion of the other product was found broken after months of crystal growth in the freezer.

Unfortunately, a master project is only allowed to take limited time so I was disarmed in the synthetic battle. However, I am convinced that compound **3a** can be prepared and isolated but not sure if it can be crystallized. Maybe the presence of the bridging chain accounts for the oily character of the compound.

Since ferrocene and its derivatives are significantly more stable than the compounds derived from bis(benzene)chromium, I wanted to master the former category first. This plan turned out to leave limited time for the latter. No reliable results came from the attempted synthesis at the [5]chromoarenophane.

6 Experimental section

6.1 General comments

All manipulations were carried out under nitrogen or argon atomosphere using standard Schlenk techniques or a glove box. Solvents were dried prior to use and used freshly distilled. TMEDA was used distilled from KOH. 2-Propanol was distilled from CaH_2. Pentane, hexane, toluene, THF, diethyl ehter, *n*-buthyl ether and glyme were dried over sodium metal wire using benzophenone as an indicator.

All NMR spectra were recorded on a Bruker AVANCE 400 MHz spectrometer, at room temperature, using $CDCl_3$ as a solvent unless other solvents are specified. Chemical shifts (δ) are reported in ppm downfield from external TMS and are referred to the respective solvent‘s residual signals, $CHCl_3$ in $CDCl_3$ at 7.26 ppm in ^{1}H NMR and at 77.16 ppm in ^{13}C NMR. Mass spectra were recorded by Helga Dögg Flosadóttir on a Autoflex III TOF/TOF laser desorption/ionization TOF mass spectrometer UV-MALDI-TOF.

6.2 Experimental

Preparation of silica gel chromatography was done in the following way:

First, the separation of the mixture on silica gel was tested on TLC plates by spotting the mixture, ferrocene and a co-spot on the plate. Three different solvent mixtures were tried as eluents:

- 50/50 petether/diethyl ether: Solvent too polar, no separation.
- 10% dichloromethane/petether: Fairly good separation.
- Hexane: Good separation of products.

Hexane was chosen as the eluent. Silica gel was placed in a Schlenk flask under nitrogen atmosphere. The flask was kept in an oven overnight so as to evaporate water from the gel. While still hot, the pressure was carefully reduced in the flask and then filled with nitrogen gas. This was done few times. Silica gel was transferred onto a sintered glass filter with a Pasteur pipette to form a 1.5 cm layer.

The dry adduct of Dilithiated ferrocene, $(C_5H_4Li)_2Fe \cdot TMEDA$ (1a)

Ferrocene (2.50 g, 0.0134 mol) was placed in a two necked 50 mL round bottomed flask equipped with a magnetic stirrer and fitted with a reflux condenser. A solution of *n*-BuLi in hexane (18.30 mL of 1.6 M solution, 0.0293 mol, 9% exc.) was added to the flask via a cannula. The suspension was rapidly stirred and TMEDA (2.45 mL, 0.0163 mol, 22% exc.) distilled two weeks earlier, added dropwise during 15 minutes. The reaction mixture was stirred for 20 hours, by then the colour had turned from deep red to orange. The thick precipitate was filtered through a sintered glass filter, and washed three times with dry oxygen-free hexane (3 x 10 mL). In the third wash the hexane was used hot. Drying in vacuum for 4 hours yielded a fine orange pyrophoric powder (3.13 g) which was stored in a glovebox under argon atmosphere.

The complex could not be determined by NMR but its presence was tested by reacting it with $SiMe_2Cl_2$ and examining the product from that reaction. It turned out to contain the desired product but also a considerable amount of unreacted ferrocene.

Dimethylsilane[1]ferrocenophane

$SiMe_2Cl_2$ (114 µL, 0.947 mol) and 7 mL of freshly distilled hexane was placed in a round bottomed flask equipped with a magnetic stirrer. 1,1'-Dilithioferrocene·TMEDA (**3a**) (288.0 mg, 0.9169 mol) and 8 mL of hexane was placed in a dropping funnel which was fitted to the flask. The content of the funnel was added to the flask in a period of one hour and the remains washed down with 3 mL of hexane. The reaction mixture was stirred overnight and by then it had turned from orange red to brown red. Hexane and excess $SiMe_2Cl_2$ were removed under vacuum and condensed into a -196 °C trap. 10 mL of hexane was added and stirred for 10 minutes before filtering through a sintered glass to remove LiCl. After drying in vacuum, the product had a very thick texture. By vacuum sublimation for two hours in 40 °C water bath, pale orange product was collected on the cold finger. ^1H NMR (CD_3CN): $\delta = 4.46$ (C_iHCHCH, t, 2H); 4.14 (C_iCH, t, 2H); 0.51 ($SiCH_3$, s, 3H).

1,3-bis(bromosilyl)propane (2). Prepared in the three following steps:

A. 1,3-bis(trichlorosilyl)propane

Allyltrichlorosilane, $CH_2{=}CH_2CH_2SiCl_3$, (88 mL, 0.602 mol) was added via a syringe into a 500 mL round bottomed flask equipped with a magnetic stirrer and fitted with a reflux condenser and an adding funnel. Trichlorosilane, $HSiCl_3$, (Caution! reacts violently with water) (68 mL, 0.674 mol) was placed in the dropping funnel. A Speier catalyst solution was prepared in the following way: H_2PtCl_6 (41 mg, $8\cdot10^{-5}$ mol) was placed in a test tube and 1.0 mL of freshly distilled 2-propanol and 5 mL of $HSiCl_3$ (taken from the adding funnel) added. The mixing is exothermal causing the solution to heat up. The Speier catalyst was divided evenly between the flask and the dropping funnel. The contents of the flask were refluxed for 15 minutes at 120 °C causing the solution to darken from pale yellow brownish to almost black and thereafter the solution from the funnel was added slowly. The reaction was exothermic, keeping the mixture warm while the dropping occurred. After the addition, the reaction mixture was refluxed at 95-105 °C for 2 hours and then transferred to a 500 mL round bottomed Schlenk flask. Excess trichlorosilane was condensed off into a -196 °C trap at reduced pressure. The product was separated from the mixture by reduced pressure distillation at 113 °C and 15 torr, giving 152.14 g of the product (152.1 g, 0.489 mol, 81% yield). ^1H NMR: $\delta = 1.52\text{-}1.61$ ($SiCH_2CH_2$, m, 4H); 1.86-2.01 ($Si\text{-}CH_2CH_2$, m 2H). $^{13}C\{^1H\}$ NMR (101 MHz): $\delta = 16.02$ ($SiCH_2CH_2$); 26.41 ($Si\text{-}CH_2CH_2$).

B. 1,3-disilapropane

1,3-bis(trichlorosilyl)propane (152.14 g, 0.489 mol) from step A and 50 mL of freshly distilled *n*-butyl ether was placed in a dropping funnel. Separately, 200 mL of n-Butyl ether was placed in a 1000 mL three necked round bottomed flask, equipped with a magnetic stirrer and fitted with a reflux condenser. The flask was placed in a 0 °C ice bath and after the solvent had surely reached the temperature of 0 °C, $LiAlH_4$ (27.9 g, 0.735 mol) was added slowly while stirring and keeping the flask in the bath. The resulting $LiAlH_4$/n-Butyl ether solution was a gray suspension. Now, the adding funnel was fitted to the flask and the pressure of the system reduced to 350 torr. The content of the funnel was added in a period of 2 hours. After the reaction mixture had been stirred for 17 hours, the temperature was raised up to 80 °C for 2 hours. The product was condensed from the reaction mixture to a -196 °C trap at reduced pressure, and the final product (35.0 g, 0.336 mol, 69% yield), fractionally distilled using a 20 cm Vigreux column at 1 atm and 35-42 °C. ^{1}H NMR: δ = 0.81-0.96 (SiCH_2CH$_2$, m, 4H); 1.55-1.67 (SiCH$_2$CH_2, m, 2H); 3.49 (SiH_3, t, 6H, ^{3}J = 3.9 Hz).

C. 1,3-bis(bromosilyl)propane (2)

1,3-disilapropane (34.88 g, 0.3344 mol) from step B and 130 mL of freshly distilled pentane was added to a 500 mL three necked round bottomed flask equipped with a magnetic stirrer and fitted with a reflux condenser. The flask was placed in a -40 °C ethyl acetate cooling bath. To a 100 mL adding funnel, 65 mL of freshly distilled pentane and Br_2 (34.4 mL, 0.669 mol) was added and the funnel fitted to the flask. The bromine was not purified specially prior to use. It was added at such a rate that only a slight brownish colour appeared in the solution, keeping the cooling bath at -30 °C to -40 °C. As the freezing point of the bromine is only -7 °C, the cooling bath had to be kept at a level below the surface of the liquid in the flask to prevent the bromine from freezing before it reached the solution. For each mol of bromine reacted, one mol of hydrogen bromide gas is produced, which was conducted through a paraffin filled valve along with a constant flow of nitrogen gas. After the complete addition of the bromine in 3.5 hours, the solution had turned pale yellow but after 13 hours of stirring it was clear again. The resulting solution was a mixture of mono-, di-, and tribrominated products and by fractional distillation using a 20 cm Vigreux column, the middle fraction was collected at vacuum and 55-60 °C (61.0 g, 0.233 mol, 70% yield). Three density measurements gave average value of 1.547 g/mL. This information was utilized in subsequent reactions to quantify correctly the molar amount, by using an Eppendorf pipette. ^{1}H NMR: δ = 1.24-1.33 (Si-CH_2CH$_2$, m, 4H); 1.72-1.85 (Si-CH$_2$CH_2, m, 2H); 4.49 (SiH_2, t, 4H, ^{3}J = 2.8).

Attempted synthesis of 1,3-Disilapropane[5]ferrocenophane (3a)

Reaction 1

In this reaction, the dilithiated ferrocene was used *in situ* so its preparation will also be described here.

Freshly distilled TMEDA (4.10 mL 27.3 mmol), 1.6 M *n*-BuLi solution in hexane (16.8 mL, 26.9 mmol) and 3.5 mL hexane was placed in a 250 mL, three-necked, round bottomed flask. The flask was equipped with a magnetic stirrer and fitted with a reflux condenser and an adding funnel. Ferrocene (2.50 g, 13.4 mmol) and 10 mL of hexane was placed to the funnel and added dropwise over two hours. The reaction mixture turned from being light yellow to bright orange. After stirring overnight, the mixture, which had lightened up again and got a thicker texture, was transferred to a dropping funnel.

1,3-bis(bromosilyl)propane (**2**) (3.48 g, 13.3 mmol) and 10 mL of freshly distilled hexane was placed in a 250 mL three-necked round bottomed flask equipped with a magnetic stirrer and fitted with a reflux condenser. The dropping funnel was fitted to the flask and the flask placed in a -10 °C cooling bath. The temperature was kept at -10 °C while the mixtures were combined dropwise over one hour. The reaction mixture was allowed to warm up slowly to room temperature and stirred for two days. By then, the mixture had three layers; precipitate at the bottom, a suspension in the middle and a clear but coloured solution on top. This was filtered through a sintered glass to remove LiBr and any insoluble materials. The resulting filtrate was a clear bright orange-peach coloured solution but after a weekend of standing untouched it lost its bright colour and a precipitate had formed. Hexane was distilled off at atmospheric pressure and 50 °C, leaving a red brown viscous mud. The wet appearance of the product indicates that the product still contains some TMEDA or even hexane so the pressure was reduced slowly down to vacuum and the heat was raised up to 105 °C. The mixture thickened and ferrocene sublimated from the mixture, resulting in product 1-A.

40 mL of freshly distilled hexane was put on 1-A, dissolving it only partly. The red-orange solution was transferred into a clean flask and a day later the hexane was condensed off into a -196 °C cooling trap under reduced pressure. During the condensation, crystals precipitated on the interior of the flask. After one hour of heat and vacuum, a thick viscous liquid remained on the bottom of the flask. NMR spectra of the crystals and the liquid revealed very different products, named 1-B and 1-C, respectively. The fractions could not be separated and were kept in the same flask for 4 months.

15 mL of freshly distilled hexane was added to the flask but only a portion of its contents dissolved. The concentrated solution was transferred via cannula onto a 1.5 cm layer of silica gel on a centered glass filter. A part of the mixture went through the silica gel while a part remained on the top of the gel. The procedure was repeated three times, so a total of 45 mL yellow/orange solution was collected. The hexane was condensed off into a -196 °C cooling trap and the resulting yellow-brown coloured viscous remains dried in vacuum for 2 hours (fraction 1-D).

Reaction 4

1,1’-Dilithioferrocene·TMEDA (0.4794g, 1.526 mmol) and 6 mL of freshly distilled hexane was added to a two necked round bottomed flask equipped with magnetic stirrer and fitted with a reflux condenser. This was stirred for 30 min to form a light orange slurry. To a dropping funnel, 3 mL of hexane and 1,3-bis(bromosilyl)propane (272 µL, 1.606 mmol, 5% exc.) was added and the funnel fitted to the flask. The content of the funnel was added dropwise over 30 min to the slurry and flushed down with 7 mL of hexane. The reaction is exothermic so the temperature of the mixture raised and its colour became browner. After stirring overnight, the mixture was filtered through a sintered glass to remove LiBr and flushed down with 8 mL of hexane. The filtrate was left untouched for 20 hours and by then some precipitate had formed. All hexane was condensed off into a -196 °C cooling trap. While the volume was being reduced, yellow brownish grains precipitated along with viscous oily liquid of the same colour. The resulting mixture was stripped under vacuum for one hour.

Five days later, attempts were made to dissolve the contents again in hexane but the solubility had decreased considerably and only a portion of the mixture did dissolve in 50 mL of hexane. The solution was decanted into another flask, leaving the undissolved viscous material which is believed to be a polymer of some sort. The volume of the solution was decreased under reduced pressure making viscous droplets precipitating from the solution and falling into the interior of the flask. These droplets could not been captured since they continuously leaked down to the bottom. When half of the hexane had been condensed off, the flask was put into a -40 °C cooling bath. Now, the viscous precipitate was more visible on the bottom. After the flask had been left at room temperature overnight, the solution was decanted from the precipitate via a cannula. The viscous precipitate was dried in vacuum, resulting in product 4-B (see text).

All the solvent was condensed off the decanted solution with reduced pressure into a -196 °C cooling trap, resulting in product mixture 4-C (see text). Its contents was planned to be separated by running it through silica gel. The product mixture (4-C) was dissolved in 40 mL of freshly distilled hexane and transferred onto the gel via cannula and run through with 50 mL of hexane, giving a yellow solution. The rest of the mixture stayed on top of the silica gel. Lack of time caused it not to be run through until the day after, with 50/50 ether/hexane solution. The products turned out to have broken down on the silica during that waiting. All the hexane solvent was condensed off the yellow solution with reduced pressure into a -196 °C cooling trap and the resulting substance dried in vacuum for 4 hours (product 4-D).

Reaction 8

Swelling of Bio-beads and preparing the column

Degassing of toluene: 50 mL of freshly distilled toluene was added to a flask which was placed in a liquid nitrogen bath at -196 °C. When the toluene was frozen, vacuum was put on the flask. When the toluene was allowed to melt again, solvated air leaved the liquid. This was repeated three times.

One tablespoon of Bio-beads S-X8 and 50 mL of degassed toluene were placed in a 250 mL Schlenk flask and allowed to swallow over a weekend. A small piece of cotton was placed at the bottom of a 20 cm glass chromatographic column with a diameter of 1 cm. The column had been constructed specially for this work by adding a Schlenk vessel on the solvent reservoir. Thus, the system could be kept under nitrogen atmosphere at all times. The swollen Bio-beads were transferred with a Pasteur pipette into the column and 80 mL of freshly distilled toluene flushed through the column with gravity flow to reach baseline equilibration.

Reaction and work-up

Dry 1,1’-Dilithioferrocene·TMEDA (161.7mg, 0.515mmol) was dissolved in 10 mL of freshly distilled toluene in a two necked round bottomed flask equipped with magnetic stirrer and fitted with a reflux condenser to make a red brown solution. 1,3-bis(bromosilyl)propane (96 µL, 148 mg, 0.566 mmol) was added via an Eppendorf pipette and the reaction mixture allowed warming up to room temperature slowly. After stirring overnight, the mixture was filtered through a sintered glass and the filtrate stirred for 4 days while the Bio-beads column was being prepared. The volume of the solution was decreased by reduced pressure condensation of hexane into a -196 °C trap until the solution seemed to be concentrated. 0.5 mL of this solution was separated on the Bio-beads packed column, using toluene as the eluent.

When the concentrated reaction mixture was examined a week later, a viscous oily precipitate was seen on the bottom of the flask, but no crystals. 0.5 mL of this solution was put on the bio-beads column but this time, a part of the mixture did not go through but stayed on the top. The solution containing the most promising fraction of the column, namely the 2 cm coloured band was prepared so as to grow crystals. The toluene was condensed off and a small amount of hexane/toluene put on instead. After two months, this flask was found broken in the refrigerator, giving no results.

Attempted synthesis at 1,3-Disilapropane[5]chromoarenophane (3b)

Reaction 1

A. Dilithiated bis(benzene)chromium, (C6H5Li)2Cr·TMEDA (1b)

10 mL of freshly distilled cyclohexane and 1.6 M *n*-BuLi/hexane (1.56 mL, 2.496 mmol) was placed in a cone-shaped flask equipped with a magnetic stirrer and fitted with a reflux condenser. To this mixture, freshly distilled TMEDA (350 µL, 2.44 mmol) was added and bis(benzene)chromium (104 mg, 0.50 mmol). The black powder did not dissolve but gave the solution a green colour. Stirring at 70 °C for one hour darkened the colour of the solution considerably and turned it to red brown.

B. 1,3-Disilapropane[5]chromoarenophane (3b)

The mixture from A was allowed to cool to room temperature under stirring. Bis(bromosilyl)propane (55 µL, 0.32 mmol) was added in one portion to the mixture via Eppendorf pipette. The addition caused white smoke to form in the flask and the colour of the mixture to turn brown. After stirring overnight, the reaction mixture contains a lot of precipitate which was filtrated through a sintered glass and washed two times with 10 mL portions of freshly distilled hexane. Directly after the filtration, precipitation was still developing in the filtrate so it was allowed to stand for two hours and by then the mat yellow/brown liquid was decanted into another flask. The solvent was condensed into a -196 °C cooling trap and the product dried in vacuum.

Reaction 2

A. Dilithiated bis(benzene)chromium, (C6H5Li)2Cr·TMEDA (1b)

Bis(benzene)chromium (147 mg, 0.70 mmol) was placed in a 50 mL cone shaped flask equipped with a magnetic stirrer and fitted with a reflux condenser. Adding 8 mL of freshly distilled cyclohexane did not dissolve the black powder but gave the suspension a green colour. To this was added in one portion TMEDA (530 µL, 3.53 mmol) via Eppendorf pipette. An adding funnel was fitted to the flask and 3 mL of freshly distilled cyclohexane and 1.6 M *n*-BuLi solution (2.20 mL, 3.53 mmol) added to the funnel. Under vigorous stirring and 70 °C, the contents of the funnel were added dropwise in 30 minutes and the temperature and stirring kept for additional hour. The colour of the suspension changed to red brown.

B. 1,3-Disilapropane[5]chromoarenophane (3b)

After stirring the mixture from A overnight it was placed in a -10 °C bath for 10 minutes without stirring and most of the cyclohexane decanted off the brown solid and replaced by 7 mL of freshly distilled hexane. 3 mL of hexane was placed in an adding funnel with bis(bromosilyl)propane (77 µL, 0.455 mmol). The reaction flask was placed in a -78 °C ethyl acetate cooling bath and stirred for 15 minutes before adding dropwise the contents of the funnel over a period of 30 minutes, under stirring. When the first drops hit the mixture, white smoke was seen in the flask but much less then when reacted at room temperature. The adding funnel was flushed with 2 mL of hexane. After keeping the temperature at -78 °C for one hour, the reaction mixture was allowed to warm up to slowly to room temperature while stirring and the stirring continued for one day.

0.5 cm of dry celite was placed on a centered glass filter and wet with freshly distilled and hot toluene. The reaction mixture was transferred onto the celite via a Pasteur pipette and filtered with 50 mL of toluene at 100 °C. As soon as the temperature of the toluene decreased again, precipitation was seen in the filtrate. The filtrate was slowly cooled down to -20 °C and kept at -18 °C in a freezer over a weekend and by then a lot of yellow precipitate was seen in the flask under a clear solvent. This was filtrated on sintered glass while still cold and washed three times with cold toluene. The resulting yellow powder (68 mg) was dried in vacuum for 3.5 hours.

Attempt to simplify the synthesis of 1,3-disilacyclohexane (4) (Nysted reaction)

The content of a Nysted reagent bottle was stirred vigorously with a magnetic stirrer. 5.68 g of the reagent (20% wt.% suspension in THF, 2.5 mmol) and 6 mL of THF was placed in a round bottomed flask equipped with a magnetic stirrer and the flask placed in a 0 °C ice bath. A solution of $BF_3{\cdot}OEt_2$ (0.28 g, 2.0 mmol)[3] in 4 mL of THF was added and the resulting mixture stirred at 0 °C for 10 minutes. A solution of 1,3-bis(bromosilyl)propane in 5 mL of THF was then added to the reaction mixture at 0 °C. Initially, the suspension was white but a grey tone was soon detected. After stirring at room temperature for 20 hours, the reaction mixture had turned dark grey. The THF solvent was condensed off at reduced pressure into a -196 °C cooling trap, leaving thick grey mud which was stripped under vacuum for drying. Freshly distilled pentane was added and the resulting mixture filtered through sintered glass. The solvent was condensed from the filtrate and the white solid product (0.14 g) dried in vacuum for 1.5 hours.

Sample preparation for mass spectrometric analysis of 6

For sample preparation, 3 mg of bisbenzimide was mixed with 0.5 mL of CCl_2H_2 and spotted on an anchorschip sample carrier, followed by a hexane solution of **6**. This was done in an argonfilled glovebox. A mass spectrum was obtained from the linear flight negative ion mode.

m/z = 908.2 (M^-, 0%); 893.660 (M^- -H_2O, 27%); 875.720 (M^- -2H_2O, 1%); 858.656 (M^- -H_2O -Cl, 1%); 846.872 ((M^- -?, 2%); 837.609 (M^- -2HCl, 4%); 793.522 (M^- -?, 3%); 777.639 (M^- -?, 7%), 758.532 (M^- -H_2O –Cp*, 5%); 733.595 (M^- -H_2O –$C(SiMe_3)_2$, 90%); 698.542 (M- -?, 5%); 675.511 (M^- -?, 26%).

---

[3] **Important note**: In the reference it is stated that $BF_3{\cdot}OEt_2$ was used in 10 mol% in their reaction. However, in the experimental chapter in the paper, 1.0 mmol of the reactant is used against 0.14 g of $BF_3{\cdot}OEt_2$. 0.14 g equals 1.0 mmol but according to the main text they intended to use 0.1 mmol. This proceidure was followed, using the molar amounts multiplied by 2. Therefore 0.28 g (2.0 mmol) of $BF_3{\cdot}OEt_2$ was used and this is 100 mol%.

References

1. Baer, T., Phys. Chem. Chem. Phys., 2005: p. 1507-1513.
2. Eliel, E.L. and S.H. Wilen, *Stereochemistry of Organic Compounds*. 1994, New York: Wiley.
3. Juaristi, E., *Conformational Behaviour of Six-Membered Rings: Analysis, Dynamics, and Stereoelectronic Effects*. Methods in Stereochemical Analysis. 1995, New York: VCH.
4. Leventis, N., S.B. Hanna, and C. Sotiriou-Leventis, J. Chem. Ed., 1997. **74**: p. 813.
5. Cuevas, G. and E. Juaristi, J. Am. Chem. Soc., 2002. **124**: p. 13088.
6. Taddei, F. and E. Kleinpeter, J. Mol. Struct. (THEOCHEM), 2004. **683**: p. 223.
7. Booth, H. and J.R. Everett, J. Chem. Soc., Perkin Trans. , 1980. **2**: p. 255.
8. Greenwood, N. and A. Earnshaw, *Chemistry of the Elements, 2nd ed.* 1997: Elsevier Butterworth Heinemann.
9. Guðnason, P.I., *Kísilinnihaldandi sexhringir*. 2003, University of Iceland.
10. Wallevik, S.Ó., et al., Organometallics, 2013. **32**: p. 6996-7005.
11. Björnsson, R., *Theoretical studies of silicon-containing six-membered rings*. 2008, University of Iceland.
12. Bodi, A., R. Björnsson, and I. Árnason, J. Mol. Struct., 2010. **978**: p. 14-19.
13. Girichev, G.V., et al., Chem. - Eur. J., 2007. **13**: p. 1776.
14. Girichev, G.V., et al., Chem - Eur. J., 2009. **15**: p. 8929.
15. Wallevik, S.Ó., et al., J. Phys. Chem. A, 2010. **114**: p. 2127.
16. Baer, T., et al., Phys. Chem. Chem. Phys., 2005. **7**: p. 1507-1513.
17. Bodi, A., et al., Rev. Sci. Instrum., 2009. **80**(034101).
18. Snæbjörnsson, Þ., *1-Halogen-1-silacyclohexan: Smíði, hreinsun og auðkenning*. 2012, University of Iceland.
19. Kealy, T.J. and P.L. Pauson, Nature, 1951. **168**(4285): p. 1039.
20. Miller, S.A., J.A. Tebboth, and J.F. Tremaine, J. Chem. Soc., 1952: p. 632-635.
21. Wilkinson, G., J. Organomet. Chem., 1975. **100**: p. 273-278.
22. Cotton, F.A., J. Organomet. Chem., 2001. **637-639**: p. 18-26.
23. Pauson, P.L., J. Organomet. Chem., 2001. **637-635**: p. 3-6.
24. Werner, H., *Landmarks in Organo-Transition Metal Chemistry - A Personal View*. Profiles in Inorganic Chemistry, ed. J. John P. Fackler. 2009, New York: Springer.
25. Elschenbroich, C., *Organometallics - Third, Completely Revised and Extended Edition*. 2006, Xeinheim, Germany: WILEY-VCH Verlag GmbH & Co. KGaA.
26. Bellas, V. and M. Rehahn, Angew. Chem., 2007. **46**: p. 5082-5104.
27. Osborne, A.G. and R.H. Whiteley, J. Organometal. Chem., 1975. **101**: p. C27-C28.
28. Roesky, H.W. and M. Lücke, Angew. Chem., 1989. **101**: p. 480.
29. Roesky, H.W. and M. Lücke, Angew. Chem. Int. Ed. Engl., 1989. **28**: p. 493.
30. Paquet, C., et al., Chem. Mater., 2004. **16**: p. 5205.
31. Manners, I., Chem. Commun., 1999. **1999**: p. 857-865.
32. Fisher, E.O. and W.Z. Hafner, Naturforsch., 1955. **10b**: p. 665.
33. Fischer, E.O. and H. Brunner, Z. Naturforsch, 1961. **16B**: p. 406.
34. Organometallics, 2002. **21**: p. 2800-2820.
35. Organometallics, 2002. **21**: p. 1520-1530.
36. Berenbaum, A. and I. Manners, Dalton Trans., 2004(13): p. 2057-2058.

37. Foucher, D.A., et al., Macromolecules, 1993. **26**: p. 2878-2884.
38. Finckh, W., et al., Organometallics, 1993. **12**: p. 823-829.
39. Hultzsch, K.C., et al., Organometallics, 1995. **14**: p. 5496-5502.
40. Pampaloni, G., Coord. Chem. Rev., 2010. **254**: p. 402-419.
41. Boekelheide, V., Top. Curr. Chem., 1983. **113**: p. 87.
42. Elschenbroich, C., et al., Organometallics, 1990. **9**: p. 889-897.
43. Baer, T., *Advance in Chemical Physics*, in *The Dissociation Dynamics of Energy-selected Ions*, I. Prigogine and S.A. Rice, Editors. 1986, John Wiley & Sons, Inc.: North Carolina, U.S.A.
44. Bodi, A., N.S. Shuman, and T. Baer, Phys. Chem. Chem. Phys., 2009. **11**: p. 11013-11021.
45. Neese, F., WIREs Comput Mol Sci, 2012. **2**: p. 73-78.
46. Allouche, A.-R., J. Comput. Chem., 2010. **32**(1): p. 174-182.
47. Zhurko, G.A. and D.A. Zhurko. *www.chemcraftprog.com*.
48. Sztáray, B., A. Bodi, and T. Baer, J. Mass. Spectrom., 2010. **45**: p. 1233-1245.
49. Bodi, A., Á. Kvaran, and B. Sztáray, J. Phys. Chem. A, 2011. **115**: p. 13443-13451.
50. Rausch, M.D. and D.J. Ciappenelli, J. Organomet. Chem., 1967. **10**: p. 127-136.
51. Bishop, J.J., et al., J. Organometal. Chem., 1971. **27**: p. 241-249.
52. Fisher, A.B. and J.B. Kinley, J. Am. Chem. Soc., 1979. **101**(22): p. 6501-66506.
53. Mitzel, N.W., et al., Inorg. Chem., 1997. **36**: p. 4360-4368.
54. Schmidbaur, H. and C.Z. Dörzback, Naturforch., 1986. **42**: p. 1088-1096.
55. Masson, G., et al., Macromolecules, 2006. **39**: p. 3720-3730.
56. Li, J., et al., J. Org. Chem., 2000. **65**: p. 7379-7390.
57. Marcellus, C.G., et al., Organometallics, 1986. **5**: p. 1395-1400.
58. Padmaja, K., et al., Inorg. Chem., 2006. **45**: p. 5479-5492.
59. Schweikart, K.-H., et al., J. Mater. Chem, 2002. **12**: p. 808-828.
60. Wagner, R.W., T.E. Johnson, and J.S. Lindsey, J. Am. Chem. Soc., 1996. **118**: p. 11166-11180.
61. Nobel, A. *Bio-Rad Laboratories*. 2000; Available from: http://www.bio-rad.com/webroot/web/pdf/lsr/literature/LIT263.pdf.
62. Elschenbroich, C., J. Organomet. Chem., 1968. **14**: p. 157-163.
63. Fritz, H.P. and E.O. Fischer, Z. Naturforsch., Teil B, 1957. **12**: p. 67.
64. Butte, W.A. and G. Eberhardt, J. Org. Chem., 1964. **29**: p. 2928.
65. Langer, A.W., Trans. N. Y. Acad. Sci. II, 1965. **27**: p. 741.
66. Gudnason, P.I. and I. Arnason, Org. Lett., 2009. **11**: p. 2015-2017.
67. Nysted, L.N., *The Nysted reagent*, in *Chem. Abstr. 1975, 83, 10406q*. 1975.
68. Matsubara, S., M. Sugihara, and K. Utimoto, LETTERS, 1998. **SYNLETT**: p. 313-315.
69. Eyjólfsdóttir, E.I., *Synthesis, analysis and reactions of novel titanasiloxane complexes. M. Sc. Thesis*. 2008, University of Iceland.
70. Sigurðardóttir, K.L., *Nucleophilic Trifluoromethylation of Substituted Hexasilacyclohexane and the Synthesis of a Titanasiloxane Complex*. 2011, University of Iceland.
71. *Mestrelab Research - Chemistry Software Solutions*. Available from: http://mestrelab.com/software/mnova-suite/.

Appendices

List of Appendices

Appendix A: Experimental BD and TPES excitation spectrum of $SiC_5H_{11}F$. 81

Appendix B: Experimental BD and TPES excitation spectrum of $SiC_5H_{11}Cl$. 82

Appendix C: Experimental BD and TPES excitation spectrum of $SiC_5H_{11}Br$. 83

Appendix D: Experimental BD and TPES excitation spectrum of $SiC_5H_{11}I$. 84

Appendix E: Example of an ORCA input file... 85

Appendix F: Example of an iPEPICO modeling program input file 86

Appendix G: Example of a iPEPICO script... 87

Appendix H: 0 K and 298 K energy of all fragments. 88

Appendix I: ^{1}H NMR spectrum of 1,3-bis(bromosilyl)propane 89

Appendix J: ^{1}H NMR spectrum of 8-C, peak set I 90

Appendix K: ^{13}C NMR spectrum of 8-C, peak set I 91

Appendix L: ^{1}H NMR spectrum of 4-D, peak set II 92

Appendix M: ^{13}C NMR spectrum of 4-D, peak set II 93

Appendix N: ^{1}H NMR spectrum of 5-A... 94

Appendix O: ^{13}C NMR spectrum of 5-A. 95

Appendix P: DEPT_135 NMR spectrum of 5-A. 96

Appendix Q: ^{1}H ^{13}C COSY NMR spectrum of 5-A. 97

Appendix R: Calculated and experimental isotopic mass patterns of 6 98

Appendix A: Experimental BD and TPES excitation spectrum of $SiC_5H_{11}F$.

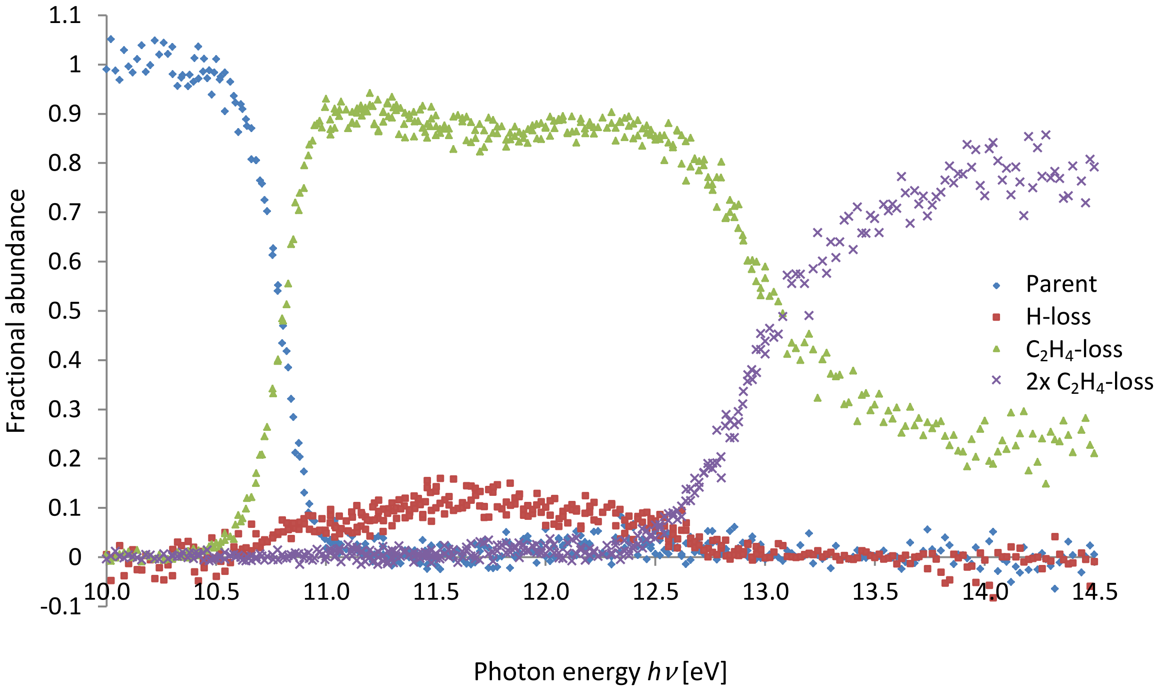

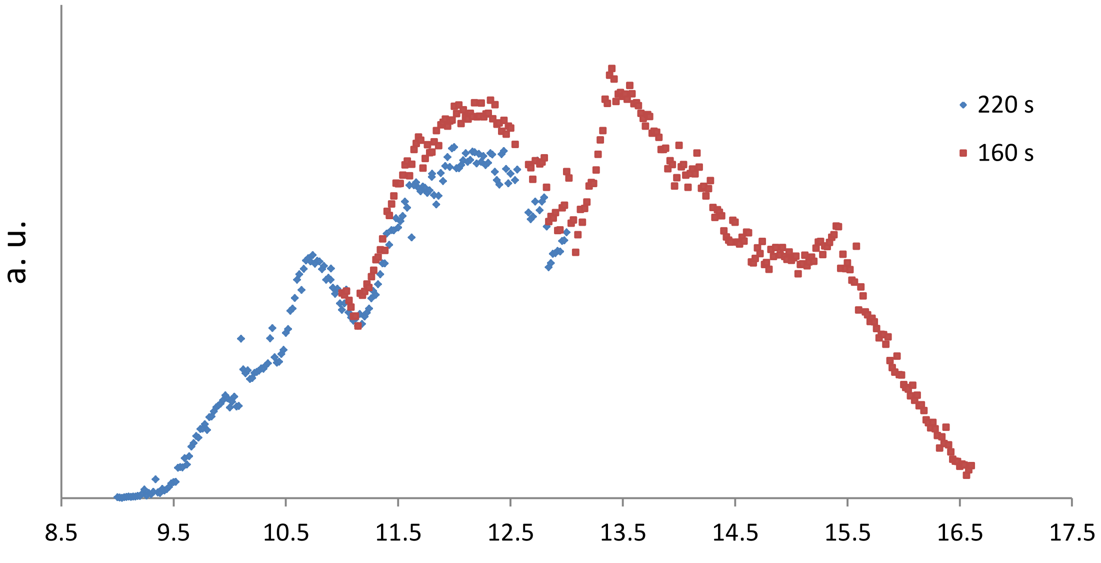

Appendix B: Experimental BD and TPES excitation spectrum of $SiC_5H_{11}Cl$.

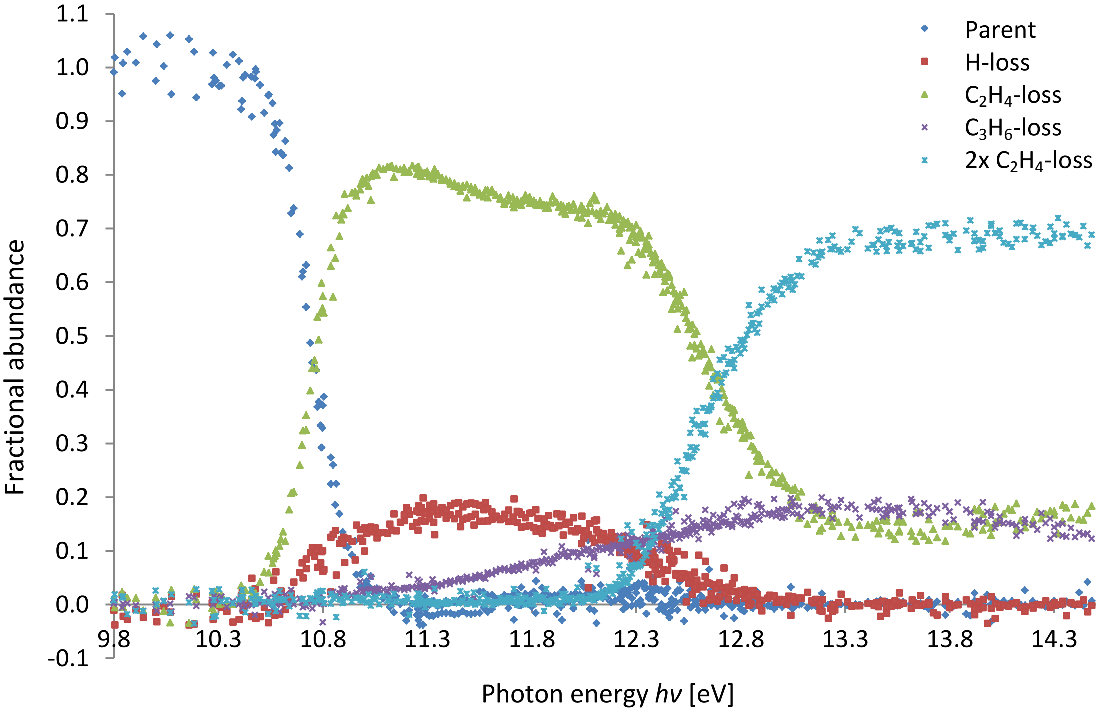

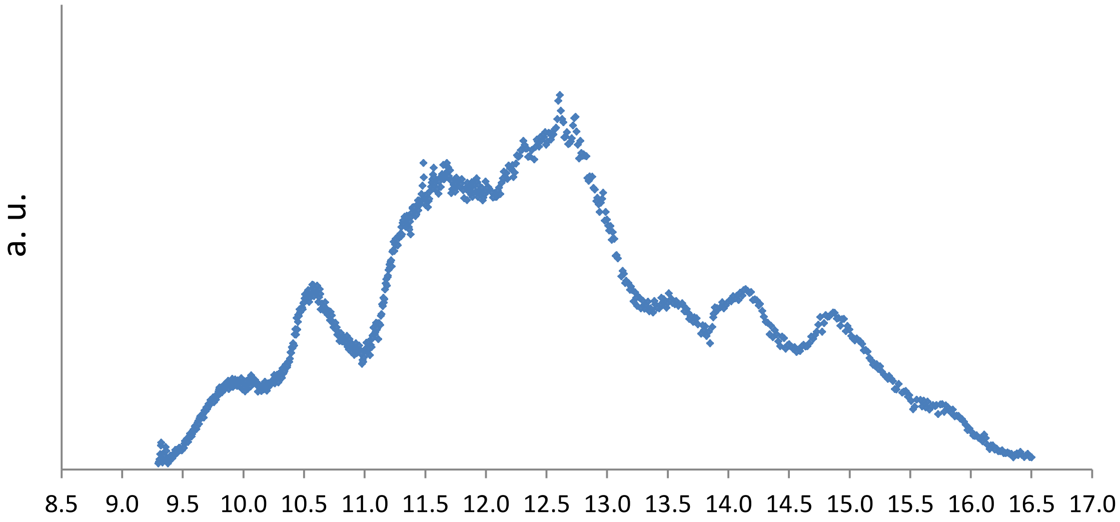

Appendix C: Experimental BD and TPES excitation spectrum of $SiC_5H_{11}Br$.

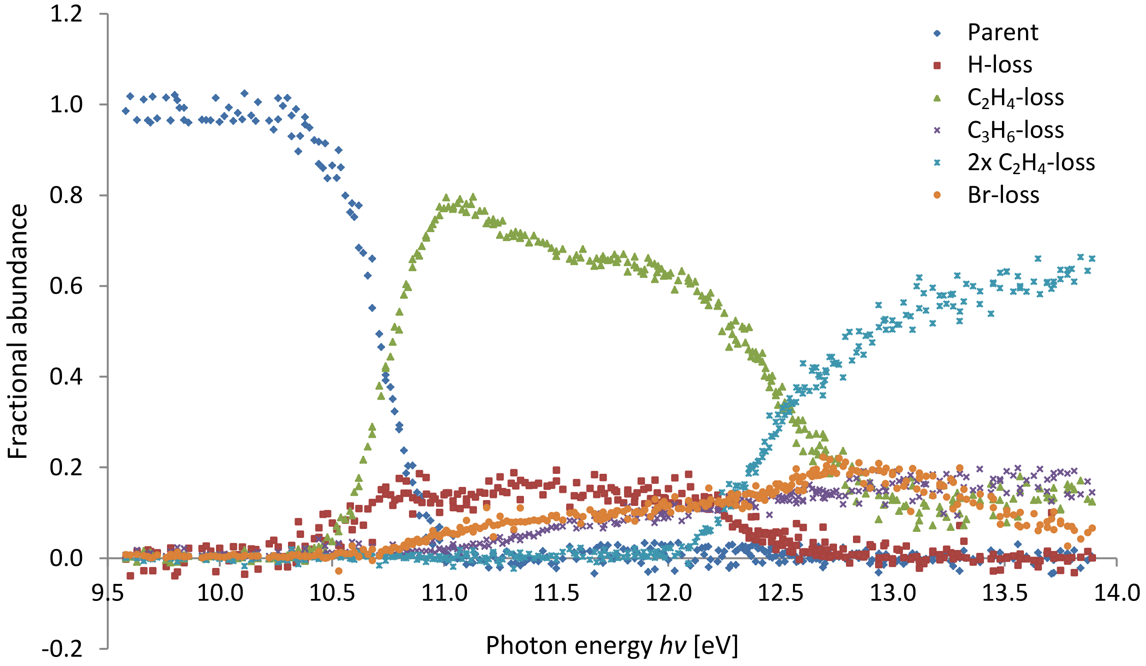

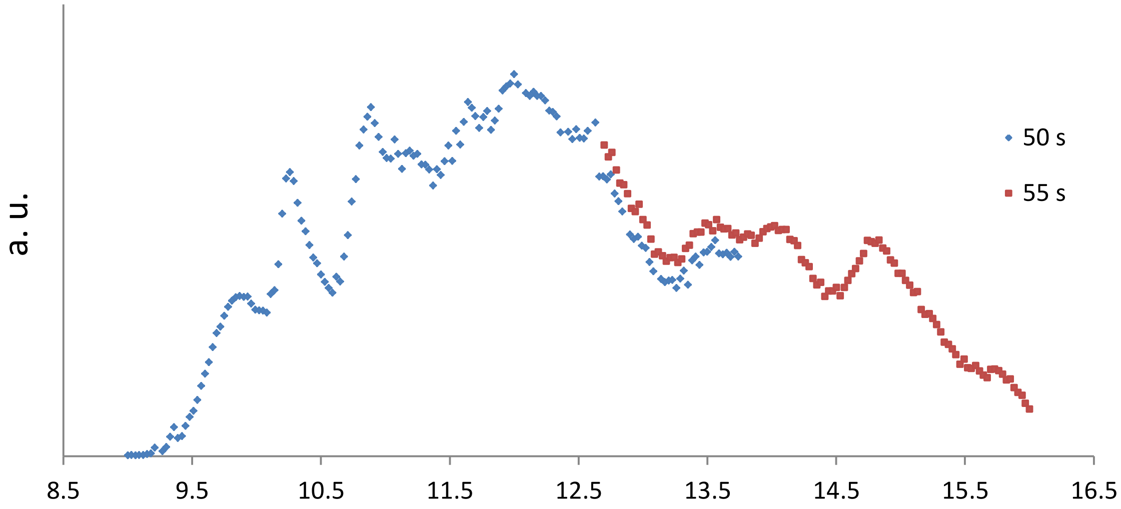

Appendix D: Experimental BD and TPES excitation spectrum of $SiC_5H_{11}I$.

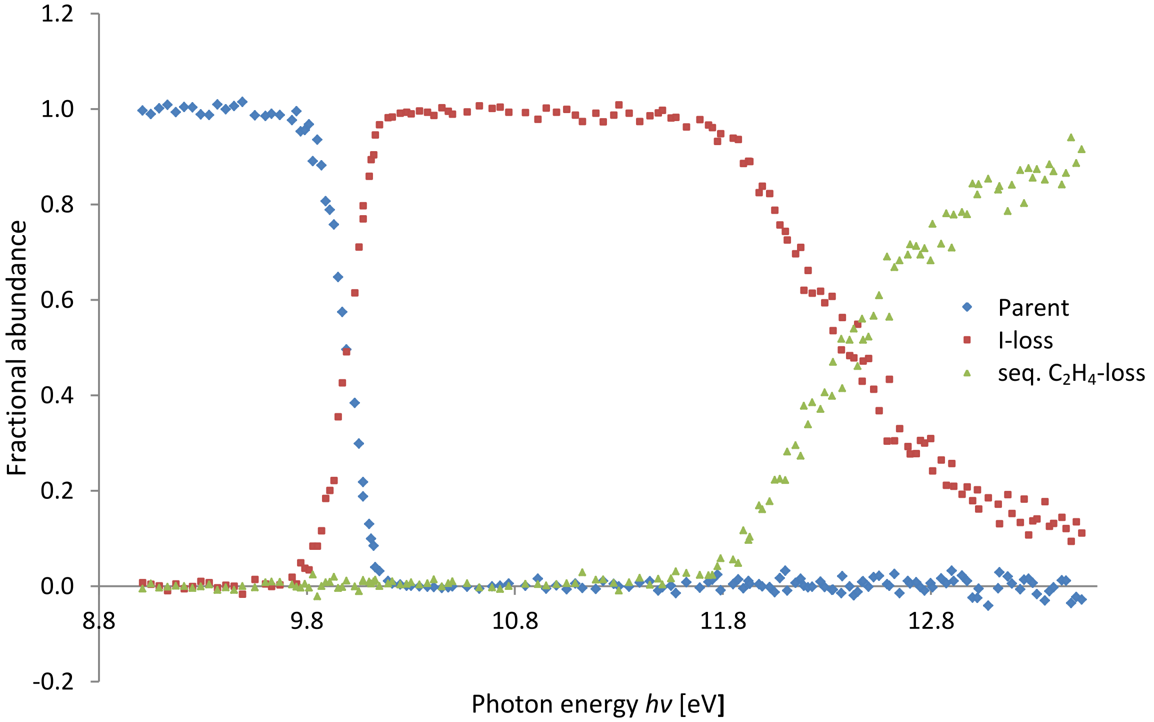

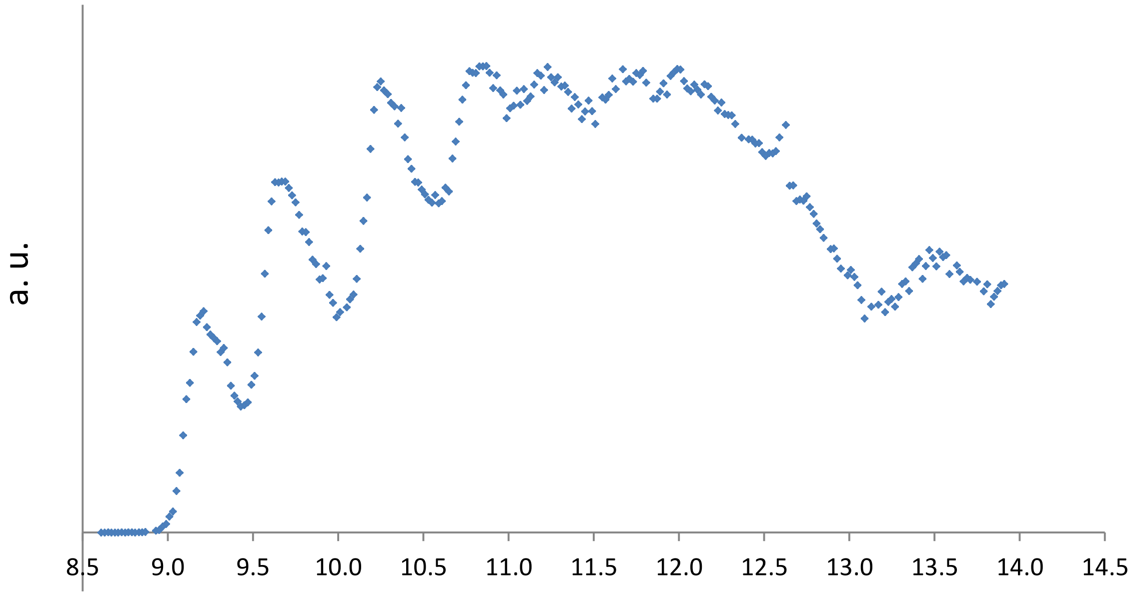

Appendix E: Example of an ORCA input file.

```
# ===============================================================
# Orca input file made in Gabedit
# ===============================================================
! Opt PW6B95 VDW10BJ TIGHTSCF Grid4 NoFinalGrid
! def2-TZVP def2-TZVP/J RIJCOSX

%geom Scan
B 1 4 = 3.34796, 2.18686, 10
end
end

* xyz 1   2
 C  -0.838342 -1.392400 0.659055
 Si  0.323339 0.034737 0.575072
 C  -0.012710 2.283837 0.848800
 C  -1.107435 1.771326 0.242977
 C  -2.437658 -0.716737 -1.165495
 C  -1.495545 -1.744858 -0.683960
 H  -0.218695 -2.213712 1.030888
 H  -1.582651 -1.207354 1.434260
 H  1.216373 0.232399 1.717937
 F  1.103395 0.189857 -0.787635
 H  0.856395 2.581507 0.276953
 H  0.010846 2.469486 1.912542
 H  -2.004355 1.550357 0.801627
 H  -1.165639 1.680320 -0.833102
 H  -2.559183 -0.532861 -2.220109
 H  -3.206231 -0.342002 -0.505732
 H  -2.026806 -2.692245 -0.534554
 H  -0.732495 -1.951645 -1.429509
*
```

Appendix F: Example of an iPEPICO modeling program input file

Modeling for F-ring breakdown

```
OUTP 1
ADIA 9.15
FWHM 9
PRES 24
RESO 18
TEMP 298.0
SYMM 2 1 2
TAIL -1600 1000
SMID 18 18
NEUE C SiC5H11F.freq
NEUR SiC5H11F.rot
IOND C C
IONF iSiC5H11F.freq iSiC3H7F.freq
IONR C C
IORF iSiC5H11F.rot iSiC3H7F.rot
MULT 2 1
FPST 1 1 1
RIGT 0 0 0
RIGF 10000 10000 10000
TSSU C C C
TSSF iSiC3H7F.freq iSiC5H10F.freq iSiCH3F.freq
TSRS C C C
TSRF iSiC3H7F.rot iSiC5H10F.rot iSiCH3F.rot
LIGV C2H4.freq H.freq C2H4.freq
LIGR C2H4.rot H.rot C2H4.rot
LDIM 2
IDIM 3
TDIM 3
BARR 9509 7867 5000
BRTR 10
PHOT 9.639 9.8001 9.9803 10.1003 10.1999 10.4594 10.5802 10.6198 10.6405 10.7004 10.7201 10.7602 10.7798
10.8405 10.8803 10.9199 10.9804 11.0398 11.0921 11.1596 11.3201 11.6008 11.8015 11.9398 12.1612 12.1998 12.3200
12.4203 12.4797 12.5810 12.6799 12.7401 12.8219 12.8780 12.9397 12.9804 13.0797 13.1209 13.1600 13.3804 13.4793
13.5808 13.6806 13.7609 13.8591 14.0811 14.3408 14.6001 14.9802 15.2797
BRAK -0.62 0.39 0.20 1.15 0.15 1.44 3.66 7.89 11.99 20.80 24.54 33.28 39.82 63.53 73.92 81.56 87.21 91.05 90.88
91.71 91.79 89.72 88.05 87.65 89.02 87.63 84.53 88.73 86.73 83.68 81.00 77.16 69.09 66.82 58.45 54.65 49.54 43.53
40.03 31.45 29.79 28.14 26.75 26.17 24.80 23.69 23.52 23.57 23.31 23.08
BRAK 1.44 0.21 1.08 0.25 1.08 1.42 3.74 3.22 1.79 3.34 4.89 5.73 5.78 4.53 7.84 9.05 8.34 6.75 8.62 6.65 8.28 10.44
11.02 9.38 6.73 9.62 9.53 8.75 6.99 4.97 2.08 1.93 0.33 1.88 0.41 0.68 2.65 0.19 0.37 -0.34 0.45 0.30 -0.09 1.03 0.54
0.08 0.61 0.72 0.27 1.79
BRAK -0.68 -0.24 -0.24 0.50 0.46 1.44 0.57 -0.59 0.12 0.68 -0.59 -0.47 1.47 0.47 -1.46 0.87 0.49 0.04 0.18 1.11 0.91 -
1.03 0.39 2.32 1.96 0.49 2.45 2.54 4.16 8.46 16.01 18.23 28.98 29.58 38.05 42.16 48.85 55.57 57.41 69.19 69.42 71.70
74.38 71.48 75.97 76.57 76.90 76.83 76.54 76.21
EXPT 4 8 12 16 20 24 28 32 36 40 44 48
EXFI F_4.tof F_8.tof F_12.tof F_16.tof F_20.tof F_24.tof F_28.tof F_32.tof F_36.tof F_40.tof F_44.tof F_48.tof
STOF F_TOF_calc.tof3
MCAS 751
MASS 118 90 62 117
PEAK 645 420
TOFP 2 2 2 2
TOFD 2
TOF1 5.5e-2 1.0e-2 55.0e-2 675 1065
SRAT model.rrkm
CURV 9.30 .01 250 bd.txt
 OPTT
 OPTP 11 21
 OPTP B1 B2
 OPTP D1 D2 P2
```

Appendix G: Example of a iPEPICO script

Script for I-ring

```
Output[CurrInFolder,I_2.txt]
SetNoiseIter[3]
AddCoincCrit[AddEvent[Im1,0,0,ROIAll,nil,Im1]]
Center := ROICircle[(-0.038;0.006),0.02,1]
Ring := ROIRing[(-0.038;0.006),0.02,0.04,1]
AddCoincCrit[AddEvent[Im1,0,0,Center,TOFStart,Im1],AddEvent[Ch6,0,50,nil,TOFStop,nil]]
AddCoincCrit[AddEvent[Im1,0,0,Ring,TOFStart,Im1],AddEvent[Ch6,0,50,nil,TOFStop,nil]]
PrintLn["Center: ", ROIToText[Center], "Ring: ", ROIToText[Ring]]
PrintLn["Masses: ", 226,99,71 ]
PeakCount := 3
P[0,0] := 19.453
P[1,0] := 12.821
P[2,0] := 10.839
P[0,1] := 19.766
P[1,1] := 14.087
P[2,1] := 11.557
CycleFiles[CurrInFolder, *.i2d]

  Load[nil, CycFile, 0, 50, 0.0024]
  PlotImage[Im1Res[1], Im1]
  Print[StripPath[CycFile], LoadedMeasTime, LoadedParam[Start,E], LoadedParam[Start,EF]]
  Print[ImageInt[Im1Res[1],Center], ImageInt[Im1Res[1],Ring]]
  For[K,2,3]
    For[G,0,{PeakCount – 1 }]
      Print[TOFInt[TOFRes[K],P[G,0], P[G,1],9.6]]
    Next
    Print[XXX]
  Next
  PrintLn[]
 Multiply[TOFRes[3],0.2915 ]
 Add[TOFRes[2],TOFRes[3]]
 SaveTOF[TOFRes[2],10,20.5,CycFile,I_TOF,False]

Next
```

Appendix H: 0 K and 298 K energy of all fragments.

All values are displayed in the unit of Hartrees

	F		Cl		Br		I			common		
	298 K	0 K	298 K	0 K	298 K	0 K	298 K	0 K			0 K	298 K
SiC5H11-X	-587.167914	-587.175769	-947.737305	-947.745372	-3062.453479	-3062.461686	-785.052374	-785.060731		SiC5H11(+)	-486.812457	-486.819533
SiC5H11-X(+)	-586.835146	-586.843578	-947.405725	-947.414339	-3062.122895	-3062.131657	-784.710087	-784.718636		SiC3H7(+)	-408.074008	-408.078504
X	-99.866874	-99.871120	-460.498449	-460.502668	-2575.236357	-2575.240574	-297.859871	-297.864119		C3-C4 afterXloss TS	-486.7530253	-486.760264
SiC5H10X	-586.277678	-586.285437	-946.852754	-946.859948	-3061.568673	-3061.576075	-784.172574	-784.180065		C3-C4 afterXloss min	-486.786910	-486.794856
C3-C4 TS	-586.788101	-586.797355	-947.358204	-947.367893	-3062.073024	-3062.082876	-784.671070	-784.681225		C2H4	-78.663114	-78.666148
C3-C4 min	-586.787138	-586.797410	-947.358998	-947.368854	-3062.074056	-3062.084094	-784.674382	-784.685294		C3H6	-118.017133	-118.021108
Lin_4ring TS	-586.769388	-586.779326	-947.341318	-947.352103	-3062.060210	-3062.069933	-784.661174	-784.671534		H	nan	-0.501300
4ring C2H4 min	-586.789931	-586.800185	-947.360731	-947.371187	-3062.059047	-3062.070621	-784.665061	-784.675120				
SiC3H7X (4ring)	-508.097525	-508.104142	-868.670785	-868.677790	-2983.388735	-2983.395735	-705.993724	-706.000791				
SiCH3X	-429.370459	-429.374676	-789.948916	-789.953400	-2904.667879	-2904.672511	-627.274538	-627.279265				
Hshift TS	-586.764801	-586.774585	-947.334332	-947.344420	-3062.049879	-3062.060146	-784.649841	-784.660279				
Hshift min	-586.811259	-586.821546	-947.380021	-947.390651	-3062.100988	-3062.111787	-784.697125	-784.707446				
SiC2H5X (3ring)	-468.744882	-468.750200	-829.322220	-829.327774	-2944.040899	-2944.046629	-666.646873	-666.652714				

Appendix I: ^{1}H NMR spectrum of 1,3-bis(bromosilyl)propane

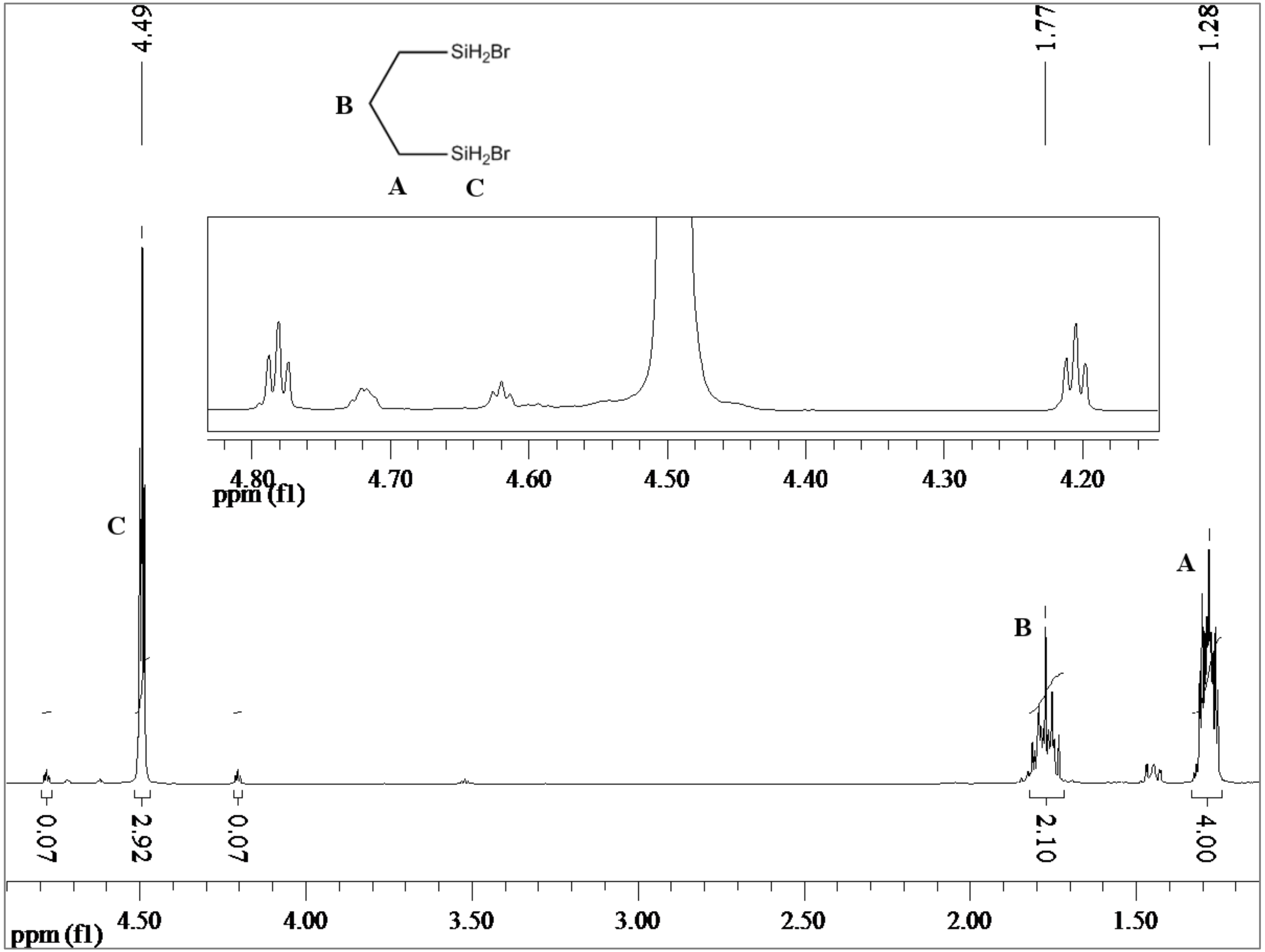

Appendix J: ^{1}H NMR spectrum of 8-C, peak set I

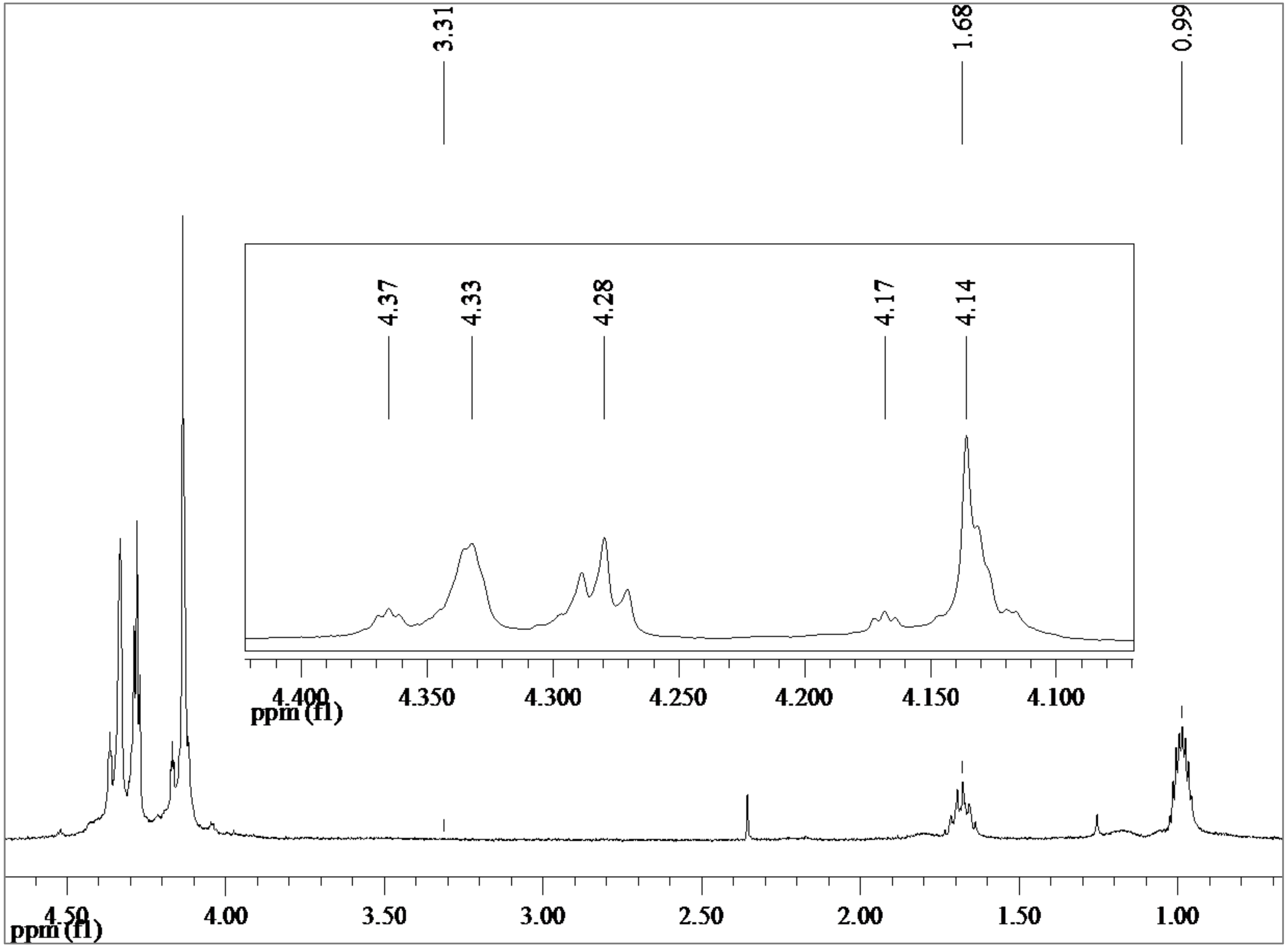

Appendix K: ^{13}C NMR spectrum of 8-C, peak set I

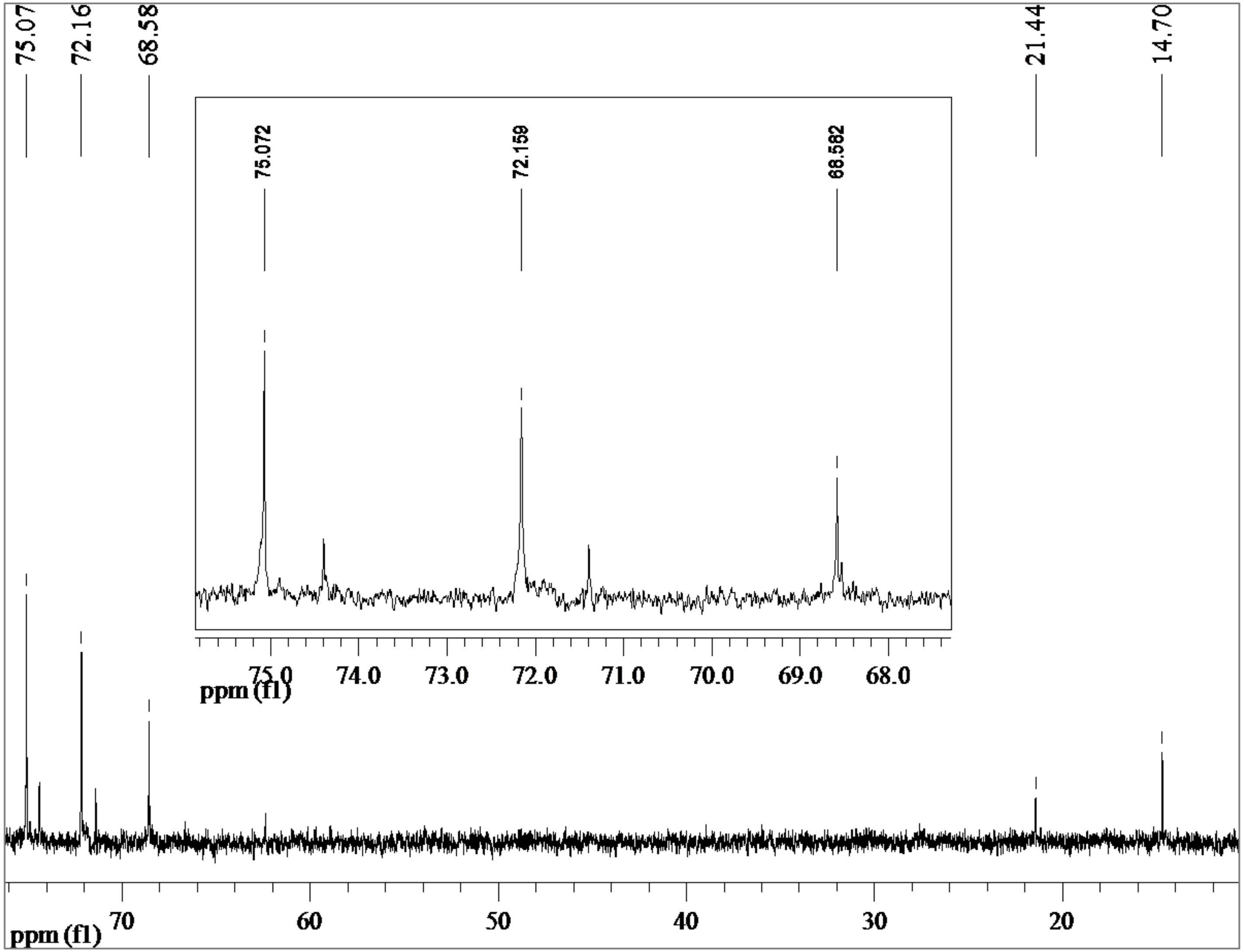

Appendix L: ^{1}H NMR spectrum of 4-D, peak set II

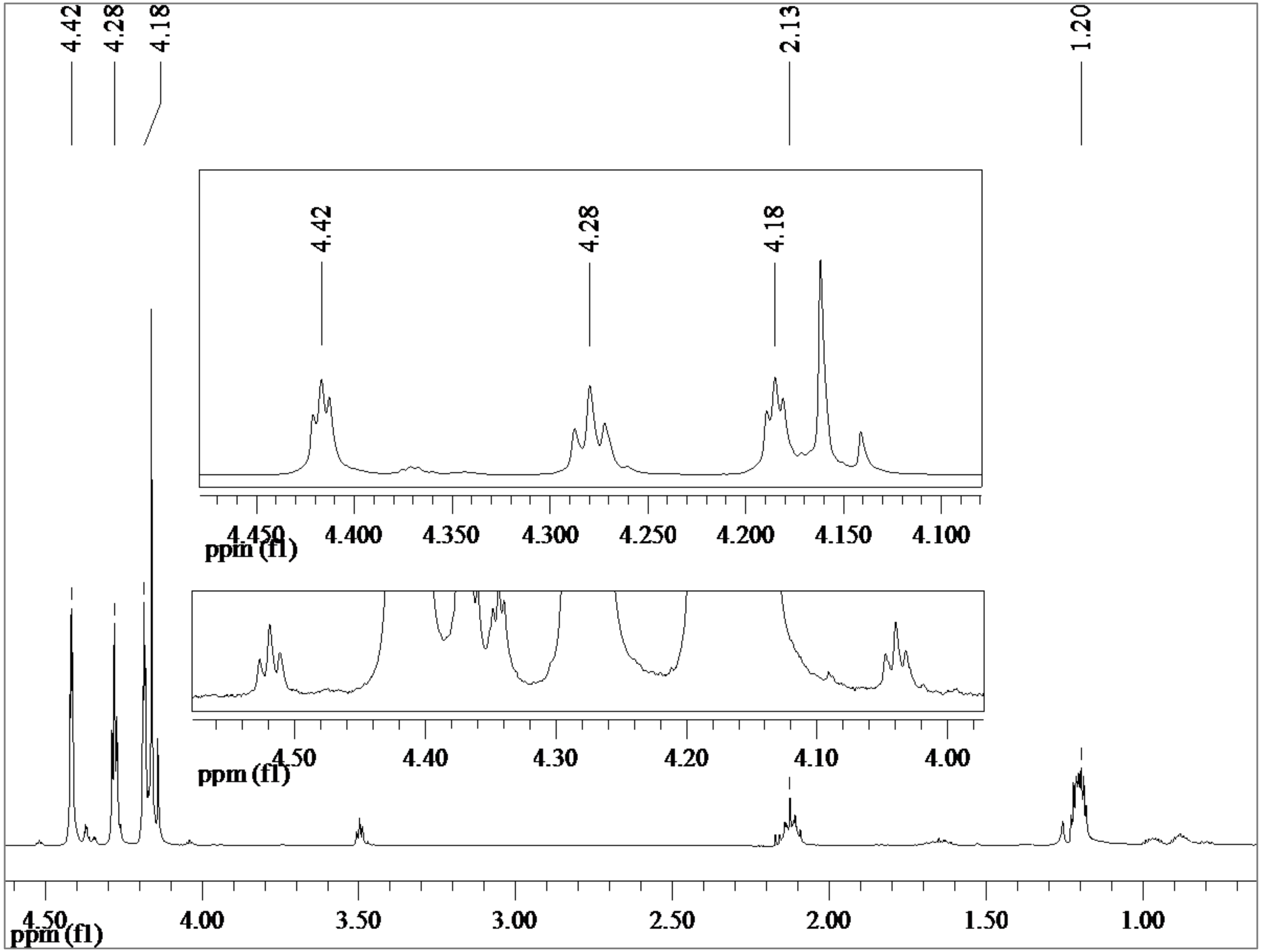

Appendix M: ^{13}C NMR spectrum of 4-D, peak set II

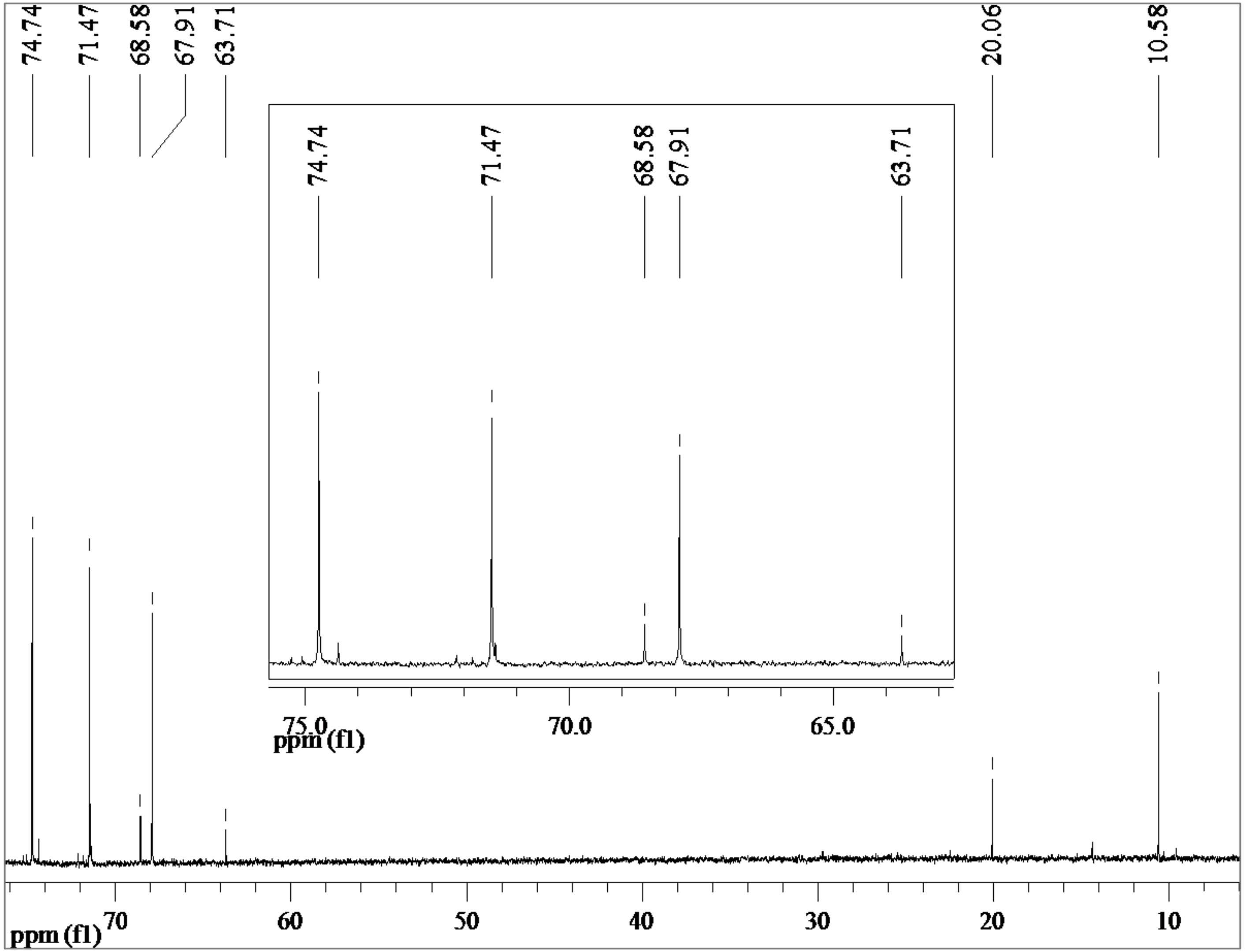

Appendix N: ^{1}H NMR spectrum of 5-A.

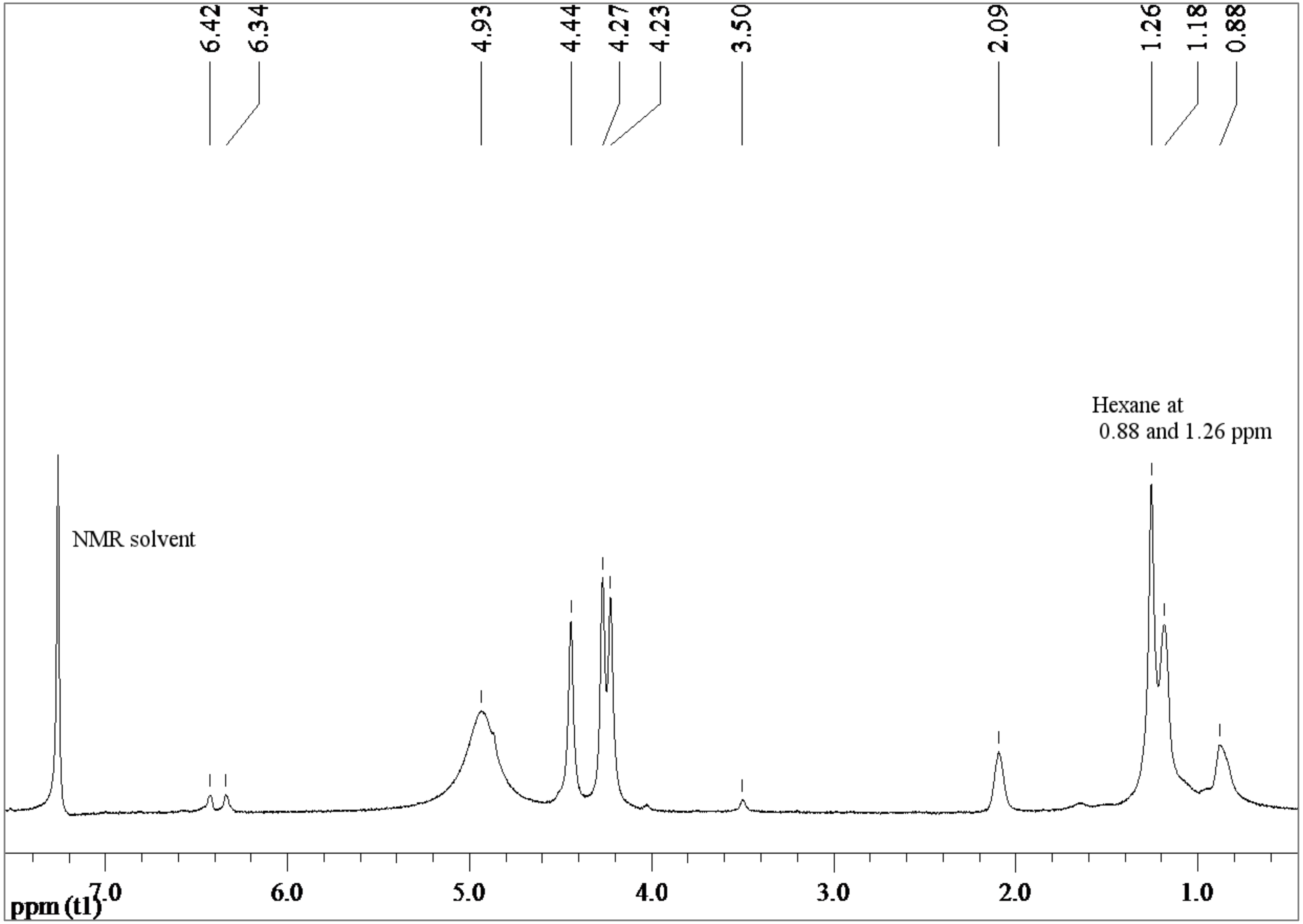

Appendix O: ^{13}C NMR spectrum of 5-A.

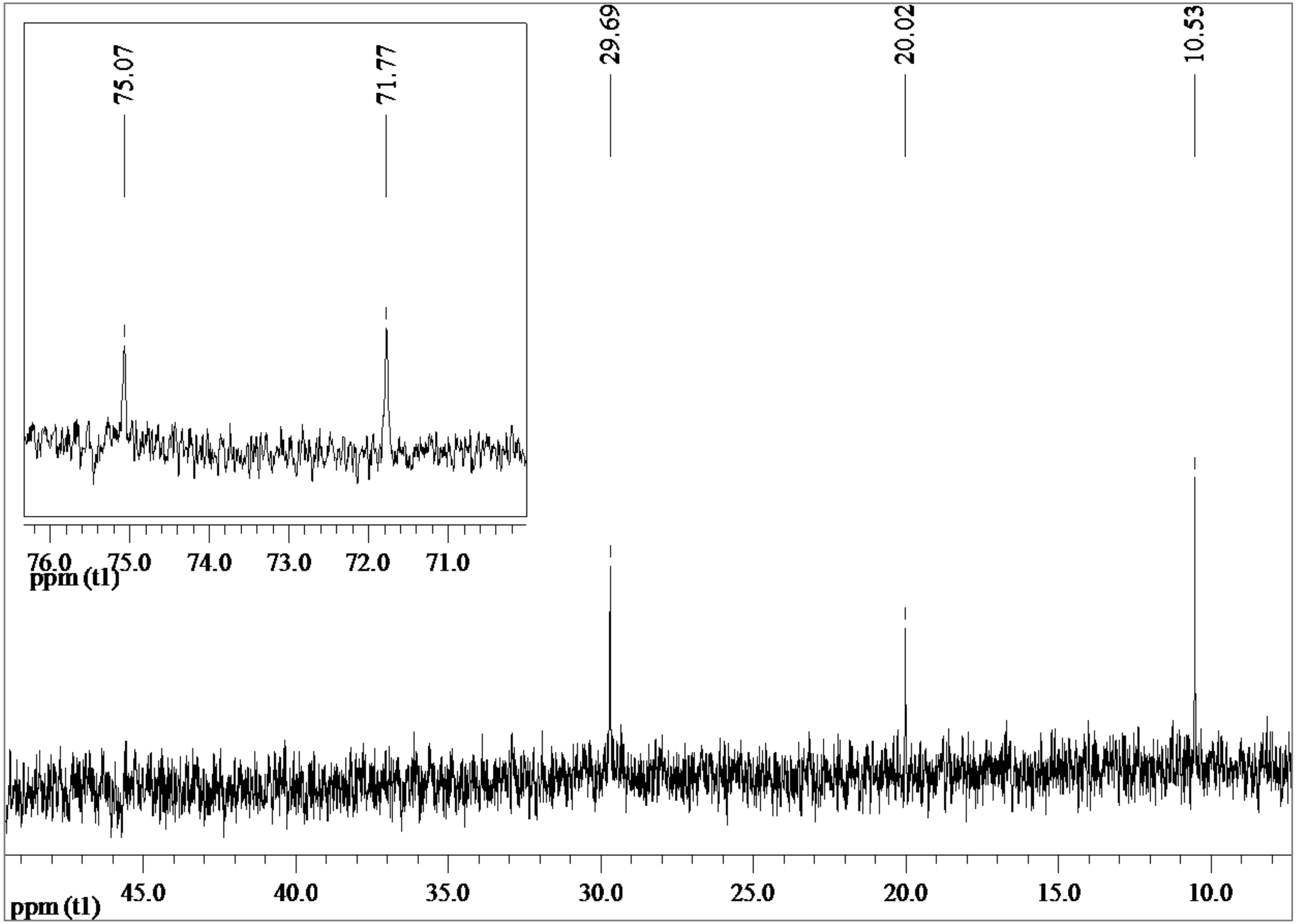

Appendix P: DEPT_135 NMR spectrum of 5-A.

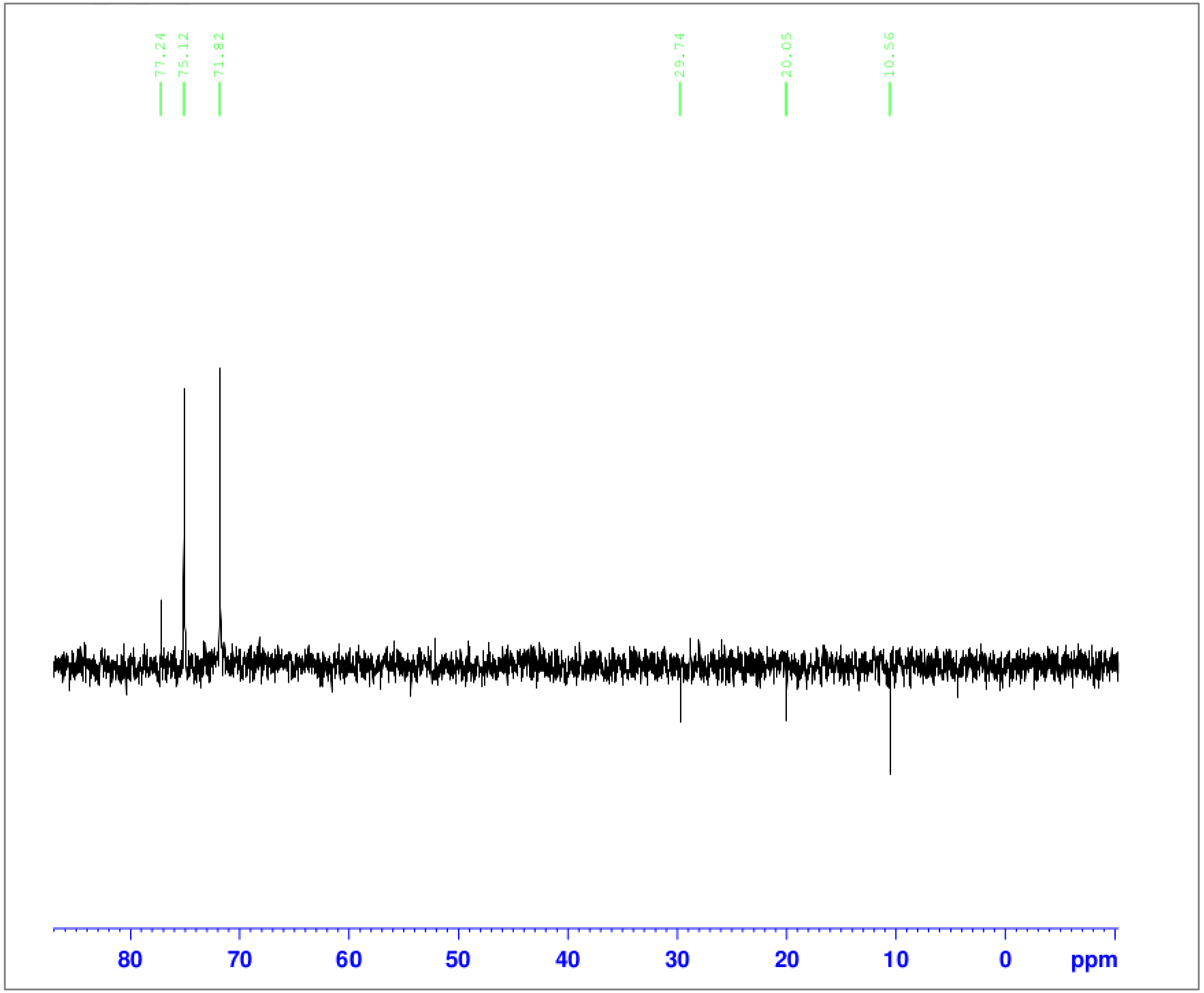

Appendix Q: ^1H ^{13}C COSY NMR spectrum of 5-A.

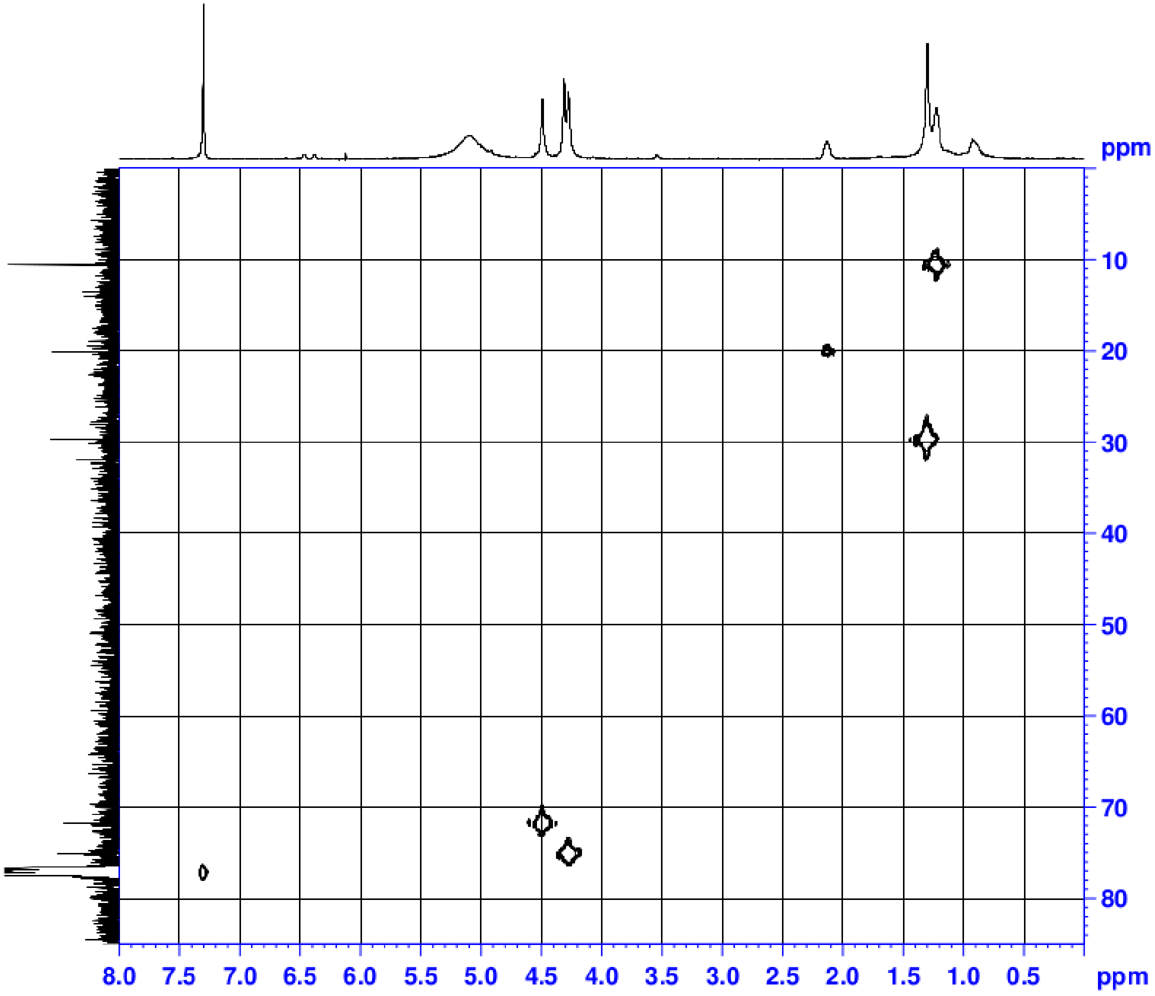

Appendix R: Calculated and experimental isotopic mass patterns of 6

Blue: experimental, red: calculated.

Lost fragment: H_2O

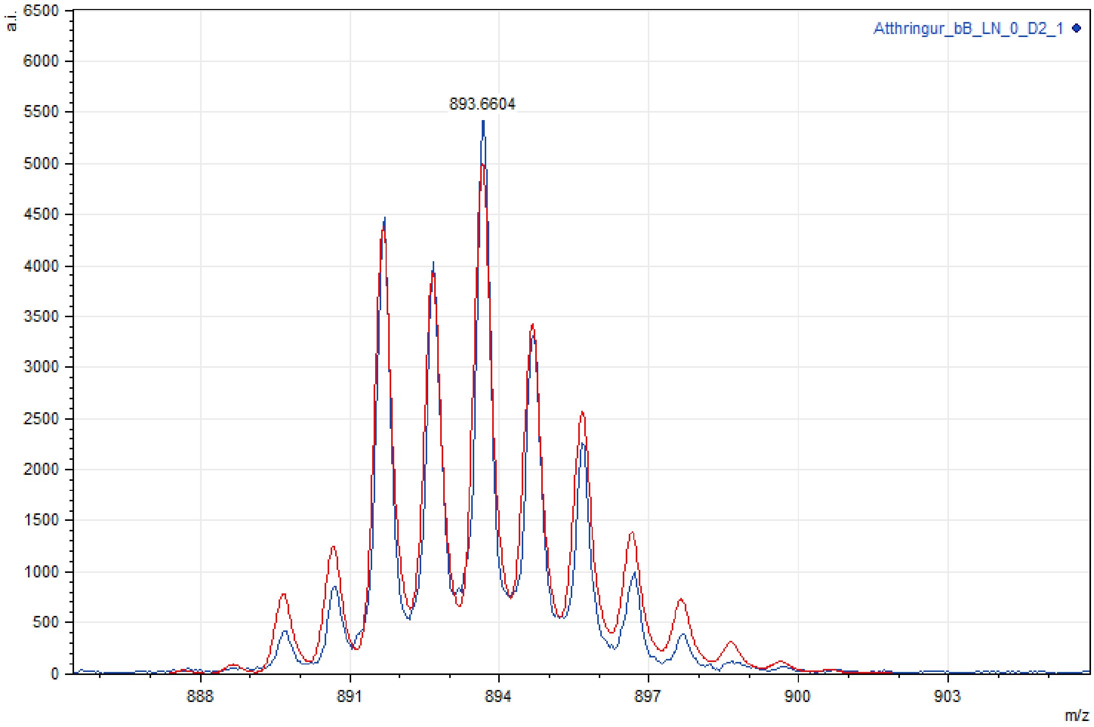

Lost fragments: 2x H_2O

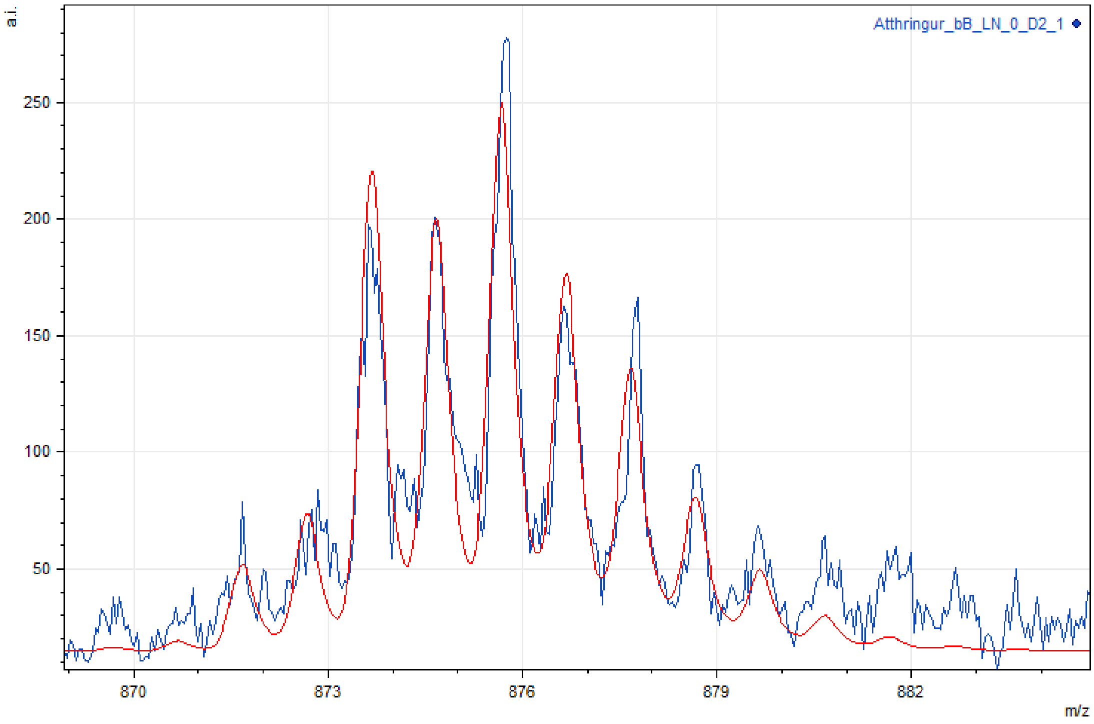

Lost fragments: H_2O and Cl

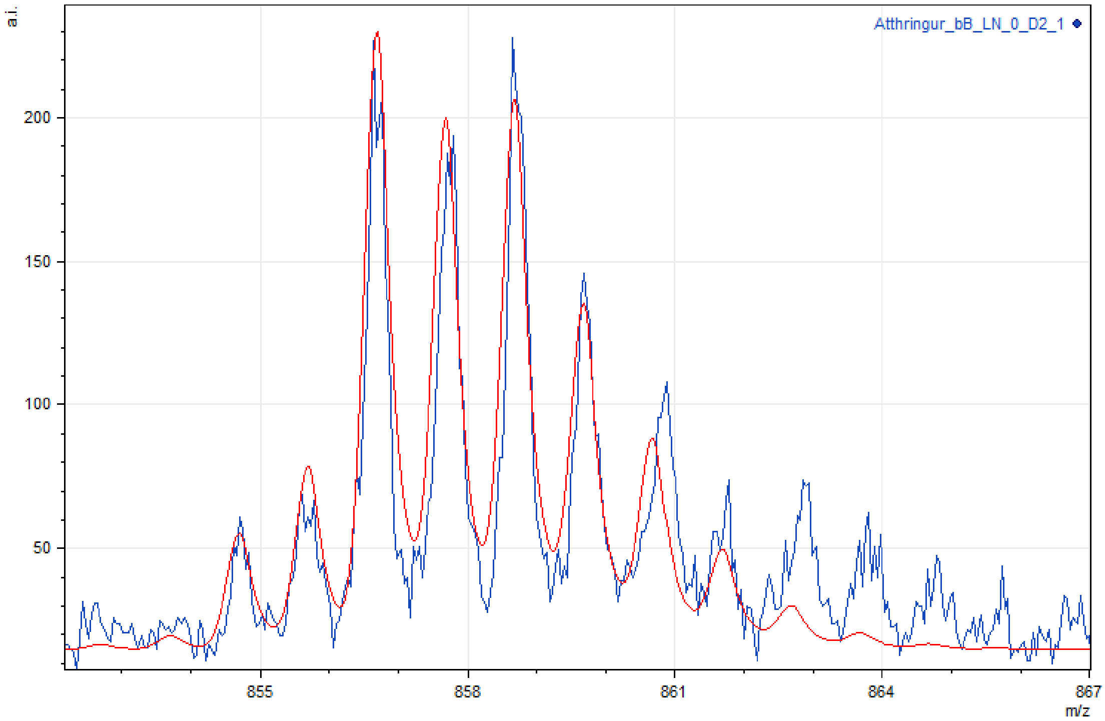

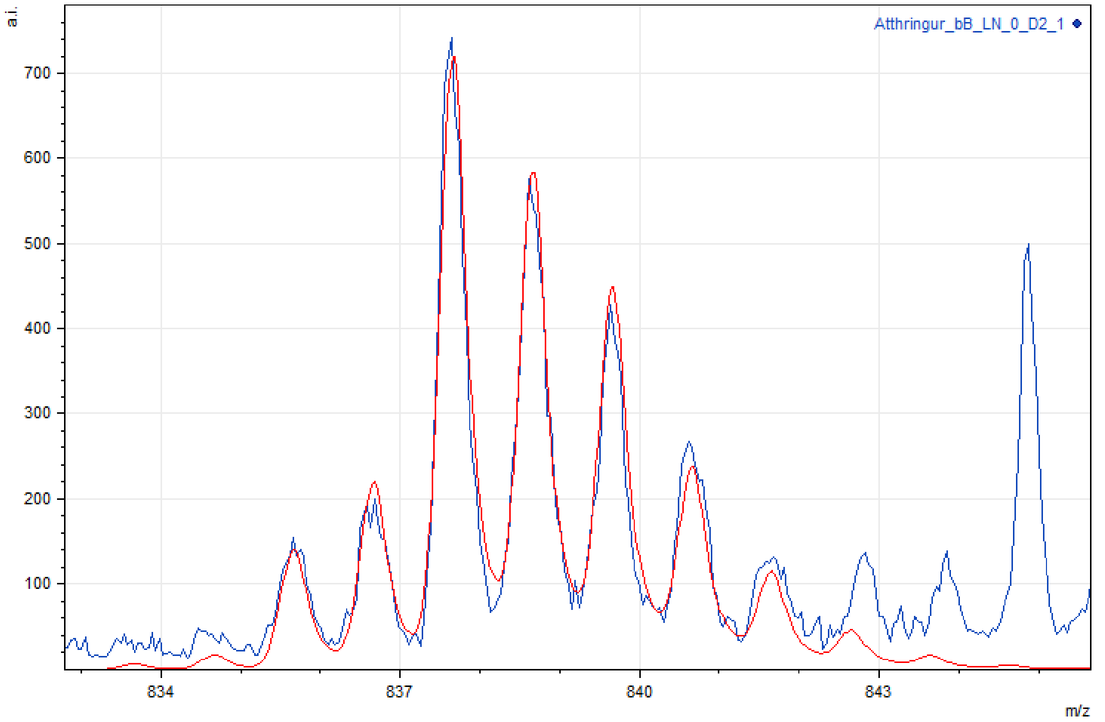Lost fragments: 2x HCl